THE UNIVERSITY OF
WARWICK

AUTHOR: **Ersilia Leonardis** DEGREE: **Ph.D.**

TITLE: **Quantifying Finite Range Plasma Turbulence**

DATE OF DEPOSIT: .....

I agree that this thesis shall be available in accordance with the regulations governing the University of Warwick theses.

I agree that the summary of this thesis may be submitted for publication.

I **agree** that the thesis may be photocopied (single copies for study purposes only).

Theses with no restriction on photocopying will also be made available to the British Library for microfilming. The British Library may supply copies to individuals or libraries. subject to a statement from them that the copy is supplied for non-publishing purposes. All copies supplied by the British Library will carry the following statement:

> "Attention is drawn to the fact that the copyright of this thesis rests with its author. This copy of the thesis has been supplied on the condition that anyone who consults it is understood to recognise that its copyright rests with its author and that no quotation from the thesis and no information derived from it may be published without the author's written consent."

AUTHOR'S SIGNATURE: .....

USER'S DECLARATION

1. I undertake not to quote or make use of any information from this thesis without making acknowledgement to the author.
2. I further undertake to allow no-one else to use this thesis while it is in my care.

DATE SIGNATURE ADDRESS

.....

.....

.....

.....

.....

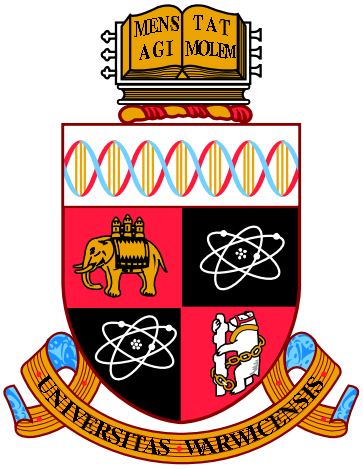

Quantifying Finite Range Plasma Turbulence

by

Ersilia Leonardis

Thesis

Submitted to the University of Warwick

for the degree of

Doctor of Philosophy

Department of Physics

June 2013

THE UNIVERSITY OF WARWICK

Ai miei genitori

(To my parents)

Contents

Acknowledgments

I acknowledge my supervisor, Prof. Sandra Chapman, for her supervision during the last four years and especially for giving me the chance to study one of the most challenging topics in physics: turbulence. During these years I experienced not only this research field, but also new languages, cultures and places. I feel I have added a precious piece to the puzzle of my Life.

I would also like to thank my research collaborators and CFSA colleagues, in particular James, Andy, Nicky and Francisco, for their pleasant company during my stay here in England.

I am very thankful also to my past and present house mates, in particular Shyaam, Elena, Natasha, Elizabeth and Giuseppe, for their friendship, which has contributed to weaken my Italian food and weather nostalgia.

A heartfelt acknowledgement goes to my closest friends, Khurom, Romina and Chiara, and my relatives, especially my uncle Pino and my cousin-friend Giuseppe for being always present and concretely helpful.

I am also grateful to my brother Nicola and to my sisters, Giovanna and Giuliana, and their partners, Mohamed and Carmelo, "simply" for being part of my Life. Last, but not least, I am very thankful to my mum and dad, for giving me freedom and tools to manage and bring value to my Life.

Declaration and published work

I declare that the work presented in this thesis is my own except where stated otherwise, and was carried out entirely at the University of Warwick, during the period of October 2009 to June 2013, under the supervision of Prof. S. C. Chapman. The research reported here has not been submitted, either wholly or in part, in this or any other academic institution for admission to a higher degree. Some parts of the work reported and other work not reported in this thesis have been published, as listed below:

Publications

- **Leonardis, E.**, Chapman, S. C., Daughton, W., Roytershteyn, V. and Karimabadi, H., Identification of intermittent multi-fractal turbulence in fully kinetic simulations of magnetic reconnection, **Physical Review Letters**, 110, 205002, (2013)

- Karimabadi, H., Roytershteyn, V., Wan, M., Matthaeus, W. H., Daughton, W., Wu, P., Shay, M., Loring, B., Borovsky, J., **Leonardis, E.**, Chapman, S. C., and Nakamura, T.K.M., Coherent structures, intermittent turbulence, and dissipation in high-temperature plasmas, **Physics of Plasmas**, 20, 012303 (2013)

- **Leonardis, E.**, Chapman, S. C., Foullon, C., Turbulent Characteristics in the Intensity Fluctuations of a Solar Quiescent Prominence Observed

by the Hinode Solar Optical Telescope, **Astrophysical Journal**, 745, 185, (2012)

- Chapman, S. C., Nicol, R. M., **Leonardis, E.**, Kiyani, K., and Carbone, V., Observation of Universality in the Generalized Similarity of Evolving Solar Wind Turbulence as Seen by Ulysses, **Astrophysical Journal Letters**, 695, L185, (2009)

Conference presentations

- **American Geophysical Union (AGU) Fall Meeting**, 3-7 December 2012 - San Francisco, California, USA.
  Oral presentation: First identification of intermittent turbulence in fully self-consistent kinetic (PIC) simulations of reconnection.

- **Magnetosphere, Ionosphere and Solar-Terrestrial (MIST)**, 30 November 2012 - London, UK.
  Poster presentation: First full quantitative characterization of intermittent turbulence in 3D particle-in cell (PIC) simulations of magnetic reconnection.

- **American Geophysical Union (AGU) Fall Meeting**, 5-9 December 2011 - San Francisco, California, USA.
  Poster presentation: Turbulent characteristics of a solar quiescent prominence observed by the SOT on board Hinode.
  Poster presentation: Generalized similarity observed in finite range magnetohydrodynamic turbulence in the corona and solar wind.

- **Magnetosphere, Ionosphere and Solar-Terrestrial (MIST)**, 25 November 2011 - London, UK.

Poster presentation: Hinode/SOT observations of turbulent fluctuations in a solar quiescent prominence.

- **National Astronomy Meeting (NAM)**, 17-21 April 2011 - Llandudno, UK.
  Poster presentation: Turbulent characteristics of the intensity fluctuations in the Hinode/SOT images of a solar quiescent prominence.

- **European Geosciences Union (EGU) General Assembly**, 3-8 April 2011 - Vienna, Austria.
  Oral presentation: The spatio-temporal characteristics of magneto-hydrodynamic turbulence seen in quiescent solar prominences by Hinode/SOT.

- **Magnetosphere, Ionosphere and Solar-Terrestrial (MIST)**, 26 November 2010 - London, UK.
  Poster presentation: Testing for signature of turbulence in Hinode/Solar Optical Telescope (SOT) observations of a solar quiescent prominence.

- **HINODE-4: unsolved problems and recent insights**, 11-15 October 2010 - Mondello, Italy.
  Poster presentation: Exploring spatio-temporal turbulent characteristics in solar prominences using the SOT instrument on Hinode.

- **Royal Astromonical Society (RAS)**, 12 March 2010 - London, UK.
  Poster presentation: Investigation of universal aspects of evolving MHD turbulence in astrophysical plasmas.

Ersilia Leonardis

June 2013

Abstract

Turbulence is a highly non-linear process ubiquitous in Nature. The non-linearity is responsible for the coupling of many degrees of freedom leading to an unpredictable dynamical evolution of a turbulent system. Nevertheless, experimental observations strongly support the idea that turbulence at small scales achieves a statistically stationary state. This has motivated scientists to adopt a statistical approach for the study of turbulence.

In both hydrodynamics (HD) and magnetohydrodynamics (MHD), fluctuations of bulk quantities that describe turbulent flows exhibit the property of statistical scale invariance, which is a form of self-similarity. For fully evolved turbulence in an infinite medium, one interesting consequence of this scale invariance is the power law dependence of the physical observables of the flow such that, for instance, the velocity field fluctuations along a given direction show power law power spectra and multiscaling for the various orders of the structure function within a certain range of scales, known as the inertial range. The characterization of such scaling is crucial in turbulence since it would fully quantify the process itself, distinguishing the latter from a wider class of scaling processes (e.g., stochastic self-similar processes).

Experimentally, it has been observed that turbulent systems exhibit an extended self-similarity when either turbulence is not completely evolved or the system has finite size. As consequence of this, the moments of the structure function exhibit a generalized scaling, which points to a universal feature

of finite range MHD turbulent flows and, more generally, of scale invariant processes that have finite cut-offs of the fields or parameters. However, the underling physics of this generalized similarity is still an open question.

This thesis focuses on the quantification of statistical scaling in turbulent systems of finite size. We apply statistical analyses to the spatio-temporal fluctuations associated with line of sight intensity measurements of a solar quiescent prominence and data of the reconnecting fields in simulations of magnetic reconnection.

We find that in both environments these fluctuations exhibit the hallmarks of finite range turbulence. In particular, an extended self-similarity is observed to hold the inertial range of turbulence, which is consistent with a generalized scaling for the structure function. Importantly, this generalized scaling is found to be multifractal in character as a signature of intermittency in the turbulence cascade. The generalized scaling recovered for finite range turbulence exhibits dependence on a function, the generalized function, which contains important information about the bounded turbulent flow such as some characteristics scale of the flow, the crossover from the small scale to the outer scale of turbulence and perhaps some characteristic features of the boundaries (future work).

The quantification of the generalized scaling is performed thank to the application of statistical tools, some of which have been here introduced for the first time, which allow to identify the statistical properties of a wide class of scaling processes. Importantly, these techniques are powerful methodologies for testing fractal/multifractal scaling in self-similar and quasi self-similar systems, allowing us to distinguish turbulence from other processes that show statistical scaling.

Chapter 1

Introduction

1.1 Overview of the thesis

This thesis focuses on the characterization of the inertial range turbulence in systems of finite size by performing statistical methods for the quantification of scaling in self-similar and quasi self-similar processes. We present analyses of turbulent plasmas in two very different environments, that is, in the lower solar corona and in simulations of magnetic reconnection.

In the first part of Chapter 1 we give a brief introduction of turbulence and its phenomenology. We review the statistical approach to the study of both hydrodynamic (HD) and magnetohydrodynamic (MHD) turbulent flows along with an overview of its historical development.
In the second part of Chapter 1, we introduce the turbulent systems for which we present analyses, namely, the solar corona and the magnetic reconnection process. In particular we highlight the main aspects of such systems which are relevant for our study.

The statistical techniques used throughout this research work are reviewed in Chapter 2. Here, we introduce and develop methodologies for quantifying the statistical properties of a wide class of scaling processes. Firstly, we give an overview of few stochastic processes showing self-affinity such as the Wiener process, the fractional Brownian motion and the Ornstein-Uhlenbeck process; secondly we focus on a narrower class of scaling processes showing an extended self-similarity such the turbulent process. We also address experimental issues which may affect the scaling properties of the time/space series

under analysis such as finite size effects of the dataset and noise.

Chapter 3 focuses on the analysis of a solar quiescent prominence in the lower corona. After a brief explanation on why we have chosen such a system, we then introduce the Hinode spacecraft which provided the observations for the analysis. Thus, we apply some of the statistical methods discussed in Chapter 2 to the spatio-temporal intensity fluctuations of the quiescent prominence under study in order to test whether their statistical properties are consistent with finite range turbulence.

In Chapter 4 we present the analysis of fully kinetic particle-in-cell (PIC) simulations of collisionless magnetic reconnection. We analyse the magnetic field data in the space domain of two reconnection simulations in a two dimensional (2D) geometry and one reconnection simulation in a three-dimensional (3D) geometry. Firstly, we focus on the 2D simulations, for which we consider two cases: a symmetric configuration and an asymmetric configuration of the magnetic field; secondly, we move to the 3D simulation.

In Chapter 5 we present a brief summary of the thesis and the main results obtained from the analyses of the quiescent prominence seen in Chapter 3 and the PIC simulations of magnetic reconnection seen in Chapter 4. Then, we conclude by discussing the results focusing mainly on the scaling properties observed to hold the inertial range of turbulence in the two finite sized systems analysed. Suggestions for future works are also given.

1.2 The phenomenon of turbulence

1.2.1 Introduction: what is turbulence?

The word *"turbulence"* comes form the Latin word *"turba"*, which means disorder. Initially, indeed, turbulence was associated to a chaotic and irregular motion of people.

During the Age of Renaissance in Italy, Leonardo da Vinci was the first to apply this term to the apparently random motion of a fluid giving a detailed description of a turbulent waterfall (see Fig. 1.1). Here, Leonardo highlighted the important role played by the coherent structures in the flow, such as the vortices, and understood that even though the microscopic features of a turbu-

Figure 1.1: Sketch of a turbulent waterfall made by Leonardo da Vinci.

lent fluid change, the macroscopic characteristics keep organizing themselves in the same manner every time the phenomenon is reproduced. After Leonardo, many scientists have been interested in this phenomenon, and as many were the definitions of turbulence proposed. Nevertheless, none of these definitions has been accepted as a unique, formal and satisfying definition of turbulence. However, there is consensus on the characteristics shown by turbulent systems such as the following:

- disorganised, seemingly random behaviour;
- dynamics non-repeatable but statistics repeatable;
- many excited modes/degrees of freedom involved;
- scale-invariance/self-similarity;
- state far from equilibrium;
- enhanced diffusion and dissipation.

The irregularity or random character of all turbulent flows makes a deterministic approach to the turbulence problem nearly intractable. Indeed, even though the governing equation of fluid dynamics, that is, the Navier-Stokes equation, is a deterministic equation, it contains non-linear terms, which become dominant as turbulence develops, leading to an intractable analytical resolution of

this equation. Thus, statistical methods have been adopted for the study of fully developed turbulence[1], which find their basis on the phenomenological description of this process.

1.2.2 The turbulence energy cascade

Leonardo's picture of turbulence gave a considerable contribution to the understanding of the turbulence phenomenon. As a matter of fact, his view of turbulence as a process dominated by coherent structures at different scales laid the foundations, after nearly four centuries, of the well known turbulent cascade, which establishes the phenomenology of turbulence.

In 1920, Lewis Fry Richardson proposed the first qualitative description of

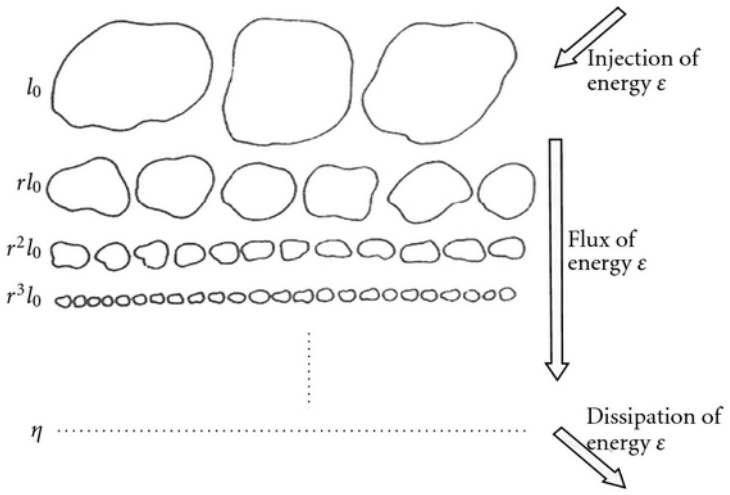

Figure 1.2: Sketch of the Richardson cascade. (Image from Frisch et al. [1978])

the turbulent cascade [Richardson, 1922]. In his book, *Weather Prediction by Numerical Process*, he wrote:

> *'Big whirls have little whirls that feed on their velocity,*
> *and little whirls have lesser whirls and so on to viscosity.'*

[1] A rigours definition of fully developed turbulence will be given in the next section.

Figure 1.2 shows a sketch of the turbulent cascade conjectured by Richardson. In this model the process of turbulence starts when energy is injected in the system at large scales l_0 and is successively transferred from larger eddies (mother eddies) to smaller and smaller eddies (daughter eddies), until it dissipates by viscosity at very small scales $l_\eta << l_0$. The input energy is introduced at the rate ε (per unit mass) which is assumed to be on average constant throughout the cascade. Also, eddies can have geometries different to circular and they are space-filling[2]. Notice that, unlike what is shown in Figure 1.2, the smaller eddies can also be embedded in the larger eddies.
The scales at which the energy transfer occurs are $l_n = l_0 r^n$, where $0 < r < 1$ and n is a positive integer. Importantly, these scales establish the so called inertial range of turbulence and satisfy the following relation $l_\eta << l_n << l_0$. Thus, in a turbulent process, one can distinguish three regions, namely, the input region, the inertial range and the dissipation region. This embodies the assumption that, in the inertial range, energy dissipation is not relevant and the energy transfer takes place locally between two or more structures at close scales (localness of interactions).

1.2.3 HD turbulence and the Kolmogorov 1941 theory

Let us consider the Navier-Stokes equation for an incompressible, viscid fluid flow:

$$\frac{\partial \mathbf{v}}{\partial t} + (\mathbf{v} \cdot \nabla)\mathbf{v} = -\frac{1}{\rho}\nabla p + \nu \nabla^2 \mathbf{v} + \mathbf{f}, \tag{1.1}$$

where $\mathbf{v} = \mathbf{v}(\mathbf{r}, t)$ is the fluid velocity field at position $\mathbf{r}$ and time t, $p = p(\mathbf{r}, t)$ is the pressure field in the fluid, ρ is the density, ν is the kinematic viscosity and $\mathbf{f} = \mathbf{f}(\mathbf{r}, t)$ is an external force per unit mass doing work on the system. Equation (1.1) expresses the conservation of momentum (Newton's second law) and comes along with the mass conservation equation:

$$\frac{\partial \rho}{\partial t} + (\nabla \cdot \rho \mathbf{v}) = 0. \tag{1.2}$$

[2]We shall see later in this chapter that both the assumptions of a constant mean transfer energy rate and a space-filling nature of the structures were soon questioned.

For incompressible fluids, that is, fluids in which the density is constant in both space and time, Equation (1.2) leads to $\nabla \cdot \mathbf{v} = 0$, which is the condition for incompressibility.

We now define the Reynolds number, R_e, as the ratio of the non-linear term and the viscous term of Equation (1.1) and, by applying dimensional analysis, we obtain:

$$R_e = \frac{|(\mathbf{v} \cdot \nabla)\mathbf{v}|}{|\nu \nabla^2 \mathbf{v}|} = \frac{V^2/L}{\nu V/L^2} = \frac{VL}{\nu}, \tag{1.3}$$

where V and L are respectively some characteristic velocity and length of the flow. The Reynolds number is a control parameter which indicates whether the flow is laminar or turbulent. It can be shown, indeed, that it is related to the number of excited degree of freedom of the flow by a dimensional analysis [Frisch, 1995, p107]. At relatively low R_e, a flow can be considered laminar (few degrees of freedom involved), whilst beyond a certain R_e, the many degrees of freedom excited interact non-linearly each other and the flow becomes turbulent. A broad variety of experiments with pipe flows have been made in order to study the transition from the laminar to the turbulent state of a fluid [e.g., Van Dyke, 1982; McComb, 1990]. It has been observed that for small values of the Reynolds number ($R_e \sim 1$) the flow possesses several symmetries, which are consistent with the Navier-Stokes equation (Eqn. (1.1)). As the Reynolds number increases ($R_e > 1$), these symmetries gradually vanish and the flow becomes more and more turbulent (see Fig. 1.3). Nevertheless, at very high Reynolds numbers ($R_e >> 1$), symmetries are restored far from the boundaries in a statistical sense, leading to a fully developed turbulence[3]. If the statistical properties of turbulence at $R_e >> 1$ are also invariant under translations and rotations in space (or time), then it is referred to as homogeneous isotropic fully developed turbulence.

One of the fundamental theories of fully developed HD turbulence was formulated by Andrey Nikolaevich Kolmogorov in 1941, that is, the so called K41 theory. In the K41 theory, Kolmogorov makes the assumption of locally isotropic time-steady homogeneous fluid turbulence. The time-steady condition implies that the energy rate injected into the system, the energy transfer

[3]In the limit of $R_e \longrightarrow \infty$ the flow becomes chaotic [Frisch, 1995, p8]. However, we shall not discuss this case as it is not the main topic of this thesis.

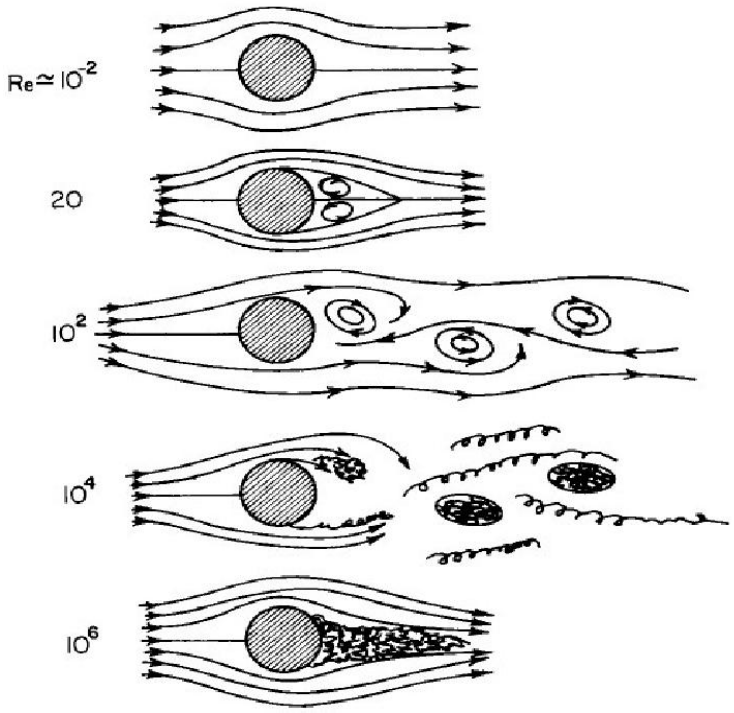

Figure 1.3: Schematic view of pipe flow experiments of turbulence at different Reynolds numbers. Notice that turbulence is fully developed for Reynolds numbers larger than 10^4. (Image from Bohr et al. [1998], p4)

rate and the energy dissipation rate must all be equal on average, while the local isotropy only holds for very large Reynolds and arises from the fact that the properties of well developed turbulence at small scales are independent of the details of the large scales. This has several implications, of which the most important is that for small scales, or large wave numbers, the turbulence exhibits *universal* behaviours.

Let us consider a turbulent flow with the above assumption, then define the longitudinal velocity increment as follows [Frisch, 1995, p57]

$$\delta v_{\parallel}(\mathbf{r}, \boldsymbol{l}) \equiv [\mathbf{v}(\mathbf{r} + \boldsymbol{l}) - \mathbf{v}(\mathbf{r})] \cdot \frac{\boldsymbol{l}}{l}. \tag{1.4}$$

Kolmogorov thus stated that, in the limit of infinite Reynolds numbers, the turbulent flow is self-similar at scales l much smaller than the large scales l_0,

and there exists a scaling exponent $h \in \Re$ such that

$$\delta\mathbf{v}(\mathbf{r}, \lambda\boldsymbol{l}) \stackrel{law}{=} \lambda^h \delta\mathbf{v}(\mathbf{r}, \boldsymbol{l}), \qquad \forall\lambda \in \Re_+, \tag{1.5}$$

for all $\mathbf{r}$ and increments $\lambda\boldsymbol{l}$ small compared to the integral scale. Under a further assumption, known as the Kolmogorov's second universality assumption, in the limit of infinite Reynolds numbers the statistical properties of $\delta\mathbf{v}(\mathbf{r}, \boldsymbol{l})$ at small scales must depend only on the scale l and mean energy dissipation rate per unit mass ε. Hence, Kolmogorov derived the two-thirds law for the second moment of the velocity increments as follows

$$< (\delta\mathbf{v}(l))^2 >= C\varepsilon^{2/3} l^{2/3}, \tag{1.6}$$

where C is a universal dimensionless constant[4]. Notice that Equation (1.6) implies that $h = 1/3$. Equation (1.6) also implies another important law, that is, the celebrated five-thirds law for the energy spectrum:

$$E(k) = C_{Kol}\varepsilon^{2/3} k^{-5/3}, \tag{1.7}$$

where C_{Kol} is a dimensionless constant called the Kolmogorov constant. Actually, this law was first derived by Obukhov [1941] and, according to Kolmogorov, was developed independently from the two thirds law [Kolmogorov, 1941].

The two thirds and the five-thirds laws have found many confirmations in both observations and numerical simulations of fully developed turbulence in fluid flows. However, the main result of the K41 theory is the four-fifths law, which is one of the few exact and non trivial results in turbulence. Given the third order structure function of the longitudinal velocity increment, the four-fifths law establishes the following equality

$$< (\delta v_{\parallel}(\mathbf{r}, \boldsymbol{l}))^3 >= -\frac{4}{5}\varepsilon l. \tag{1.8}$$

Equation (1.8) arises from a dimensionless analysis consistent with the sim-

[4]In the next section we shall see that the universality of the constant C was soon questioned by Landau.

ilarity hypothesis of the K41 theory and implies that the rescaling exponent h of the velocity increments in Equation (1.5) must be $1/3$. Note also that, in order to show that $h = 1/3$, the assumption of isotropy is not necessary [Frisch, 1995, p89].

Let us now examine the consequences of the K41 theory for the pth moment of the velocity increments, $S_p(l)$, at the inertial scales l, assuming homogeneity and isotropy. We define the structure function of order $p > 0$ along a given direction r, as follows

$$S_p(l) \equiv < v(r+l) - v(r)^p > = < \delta v(r,l)^p >, \tag{1.9}$$

where the angular brackets indicate an ensemble average over r. Then, the two-thirds (Eqn. (1.6)) and the four-fifths (Eqn. (1.8)) laws suggest the following scaling for the pth order structure function

$$S_p(l) = C_p \varepsilon^{\zeta(p)} l^{\zeta(p)}, \tag{1.10}$$

where the C_p are dimensionless coefficients and the scaling exponent $\zeta(p) = p/3$. Notice that, for $p = 3$, Equation (1.9) leads to the four-fifths law with $C_3 = -4/5$. Moreover, as stated in the K41 theory, the moment scaling law only depends on the mean energy dissipation rate ε and the scale l and does not involve the integral (large) scale l_0. Thus, for positive fixed values of ε, either when $\nu \longrightarrow 0$ and/or $l_0 \longrightarrow \infty$, the pth moment of the structure function does not diverge to infinity.

The *universal* role played by the C_p coefficients has been largely discussed by the turbulence community. In 1942 Landau pointed out that there is no reason to suppose the C_p are universal (except for $p = 3$). Indeed, according to Landau, the energy dissipation rate changes over times of the order of the periods of the large eddies ($\backsimeq l_0$), therefore the mean energy dissipation rate ε must depend on the large scales l_0 at which the turbulence mechanism is produced [Landau and Lifshitz, 1987]. As a consequence of this, the C_p cannot be universal since they are different for different flows (e.g., different geometries).

1.2.4 MHD turbulence and the Iroshnikov-Kraichnan model

The general equations describing an electrically conducting magnetized flow in the limits of the MHD approximation are the following:

$$\rho\left[\frac{\partial \mathbf{v}}{\partial t} + (\mathbf{v}\cdot\nabla)\mathbf{v}\right] = -\nabla p + \mathbf{J}\times\mathbf{B} \qquad (Momentum\ conservation) \quad (1.11)$$

$$\frac{\partial \rho}{\partial t} + (\nabla\cdot\rho\mathbf{v}) = 0 \qquad (Mass\ conservation) \quad (1.12)$$

$$\nabla\times\mathbf{E} = -\frac{\partial \mathbf{B}}{\partial t} \qquad (Faraday's\ law) \quad (1.13)$$

$$\nabla\times\mathbf{B} = \mu\,\mathbf{J} \qquad (Ampère's\ law) \quad (1.14)$$

$$\nabla\cdot\mathbf{B} = 0 \qquad (Gauss'\ law) \quad (1.15)$$

$$\mathbf{E} + \mathbf{v}\times\mathbf{B} = \frac{\mathbf{J}}{\sigma} \qquad (Ohm's\ law) \quad (1.16)$$

where $\mathbf{J}$ is the current density, $\mathbf{B}$ is the induction (commonly called "magnetic field"), $\mathbf{E}$ is the electric field, μ is the magnetic permeability and σ is the electrical conductivity. The last four equations in the system above are the well known Maxwell's equations. The above system of equations is closed by an equation of state, which relates the plasma pressure to the temperature and density, and its form depends on the assumptions that one makes about the thermodynamic state of the systems.
Manipulating the above equations, an expression for the induction can be derived and written as follows:

$$\frac{\partial \mathbf{B}}{\partial t} = \nabla\times(\mathbf{v}\times\mathbf{B}) + \lambda\nabla^2\mathbf{B}, \quad (1.17)$$

where $\lambda = (\mu\sigma)^{-1}$ is the magnetic diffusivity, which is here considered uniform.

As in HD, turbulence arises from the non-linear terms so that, similar to the usual Reynolds number, a magnetic Reynolds number, R_m, can be defined as the ratio of the non-linear term and the diffusion term of Equation (1.17), then

$$R_m = \frac{VL}{\lambda}, \quad (1.18)$$

where V is some average fluid velocity, which is often wrongly replaced by

the Alfvén velocity, $V_A = B/\sqrt{\mu\rho}$, leading to the definition of the Lundquist number S instead [Biskamp, 1993, p175]. The latter, indeed, is defined as $V_A L/\lambda$ and, unlike the magnetic Reynolds number, does not give any indication about the possible turbulent status of a MHD flow. As a matter of fact, high Lundquist numbers ($S >> 1$) may simply mean that the resistivity is small, corresponding even to $R_m \sim 0$ for static systems. On the contrary, high magnetic Reynolds numbers only arise from large fluid velocities generated by the non-linear dynamics, making therefore the system prone to turbulence.
Likewise in HD, fully developed MHD turbulence is characterized by large magnetic Reynolds numbers ($R_m >> 1$) for which statistical properties of the fluctuations show universal behaviour and scaling laws.

In MHD flows, there is often a large-scale background field, $\mathbf{B_0}$, which cannot be eliminated by a Galilean transformation. As a consequence of this, turbulent flows are typically highly anisotropic and therefore the assumption of isotropy is not always valid as it was for the HD case. Indeed, while dispersionless Alfvén waves propagate either parallel and anti-parallel to $\mathbf{B_0}$, in the direction perpendicular to $\mathbf{B_0}$, shear perturbations at the Alfvén speed generate at small scales giving rise (potentially) to turbulence [Biskamp, 1993, p178]. The effect of the Alfvén waves is to decrease the energy transfer rate in the turbulent cascade; in other words, a single eddy takes longer (with respect to the HD case), to transfer its energy to one or more smaller eddies [e.g., Carbone, 1993, and references therein]. This led to refinement of the Kolmogorov's theory for its applicability to MHD turbulent flows.
In 1964 Iroshnikov and, one year later, Kraichnan laid the foundations of the MHD turbulence model [Iroshnikov, 1964; Kraichnan, 1965]. By taking into account the effects of Alfvén waves on the turbulent cascade, they derived a power law for the power spectrum of the form

$$E(k) = C'_{Kol}(V_A\varepsilon)^{1/2}k^{-3/2}, \tag{1.19}$$

where C'_{Kol} is a constant which depends on $\|\mathbf{B_0}\|$ and hence on the geometry of the large scales eddies. Importantly, this expression is not dimensionless and thus profoundly differs from C_{Kol} obtained in the Kolmogorov's five-thirds law (Eqn. (1.7)). Indeed, while the Kolmogorov spectrum depends only on ε at

the inertial scales, the Iroshnikov-Kraichnan spectrum depends also on the large-scale background field. Furthermore, the Iroshnikov-Kraichnan model for MHD turbulence anticipates moments with scaling exponents $\zeta(p) = p/4$, thus smaller than $p/3$ expected by the K41 model. Therefore, according to this model, if the energy transfer rate is constant, then $\zeta(4) = 1$, in contrast to $\zeta(3) = 1$ obtained from K41.

Although the Iroshnikov-Kraichnan spectrum has been often observed in MHD turbulent flows like the solar wind, however also the Kolmogorov's spectrum predicted for HD turbulence has been observed in this environment, leading to the conclusion that both types of turbulence may coexist in highly anisotropic MHD flows [Chapman and Hnat, 2007].
Moreover, numerical and analytical studies of incompressible MHD turbulence, where the cascade is mediated by Alfvén fluctuations, show that the different scaling exponents for the power spectra might depend upon the strength of the turbulence, the strength of the background field, $\|\mathbf{B_0}\|$, and anisotropy. Specifically, it has been observed that introducing anisotropy to MHD models of turbulence, the power spectrum scales as $\sim k_\perp^{-2}$ for weak turbulence [e.g. Galtier et al., 2000] and $\sim k_\perp^{-5/3}$ - i.e. the Kolmogorov spectrum - for strong turbulence [e.g., Higdon, 1984; Goldreich and Sridhar, 1995] with respect to the background magnetic field. In particular, Goldreich and Sridhar [1995] showed that magnetic and velocity field perturbations only occur perpendicular to $\mathbf{B_0}$ leading to the following relationship $k_\parallel = k_\perp^{-2/3} l_0^{-1/3}$, where l_0 is the outer or energy injection scale. Considering the turbulence cascade picture, this could be seen as elongated eddies - i.e. "rope-like" or "sheet-like" structures - along the direction of $\mathbf{B_0}$.

1.3 Statistical properties of turbulence

The dynamical behaviour of any particular flow variable in either HD or MHD turbulent systems is highly random due to the large number of degrees of freedom involved, which are coupled through non-linear interactions. Mathematically, the description of such systems should center on invariant measures; however, there is no rigorous theory about what measures are strictly invariant in turbulent flows. Nevertheless, experimental observations strongly support

the idea that turbulence at small scales achieves a statistically stationary state. This is the basic motivation for seeking a universal statistical description of turbulence.
In this sections an overview of the main statistical properties of turbulent flows is given along with some models that have been developed in order to include these statistical characteristics into the theory of turbulence.

1.3.1 Intermittency

Both the Kolmorogov theory for HD turbulence and the Iroshnikov-Kraichnan model for MHD turbulence assume that the energy transfer (or dissipation) rate ε within the inertial range is on average constant. We have seen that this leads to a linear scaling exponent $\zeta(p)$ in p for the various moments of the structure function. However, the energy transferred by the eddies at the inertial scales l is actually far from uniform, implying that the self-similarity property of the velocity fluctuations (see Eqn. (1.5)) at the inertial scales is lost. Experimentally this is seen as a non-linear trend of $\zeta(p)$ with p and as a strongly intermittent, bursty, nature of the fluctuations of the bulk quantities that describe both HD and MHD turbulent flows. This phenomenon is known as intermittency.
Intermittent signals are typically dominated by large occasional events and characterized by heavy tailed probability density functions (PDFs) of their fluctuations. The bursty nature of a random function $f(r)$ in the space (or time) domain can be quantified via the flatness (or kurtosis K) of the probability distribution of its increments $\delta f(l) = f(r+l) - f(r)$ [5]. The flatness estimates the importance of the tails of the distribution and is defined as the normalised fourth moment of a distribution [Frisch, 1995][p122], namely:

$$K(l) = \frac{< (\delta f(l))^4 >}{< (\delta f(l))^2 >^2} \tag{1.20}$$

For a Gaussian distribution $K = 3$. An excess kurtosis, k, is usually defined as $k = K - 3$ in order to set $k = 0$ for Gaussian distributions. The func-

[5] Notice we have dropped the space argument r in the increments $\delta f(l)$ by assuming statistical homogeneity.

tion $f(r)$ is then said to be statistically intermittent if the fluctuations $\delta f(l)$ have flatness that increases as l goes to smaller and smaller scales. Therefore, according to this definition, neither self-similar nor Gaussian signals are intermittent. From Equation (1.20) we can clearly see that the expression for the flatness involves the fourth and second moments of the fluctuations suggesting that, for intermittent turbulence, even higher order statistics will be subject to modifications.

In 1962, Kolmogorov and Obukhov refined the K41 theory introducing intermittency effects in the turbulence cascade of energy [Kolmogorov, 1962; Obukhov, 1962] formulating the well known Kolmogorov-Obukhov theory of turbulence, in short K-O62. This theory was successively developed in detail in Monin and Yaglom's texbook of turbulence [Monin and Yaglom, 1971], in which the authors introduce a local energy dissipation rate at the scale l, ε_l, which is statistically independent on the velocity increments nondimensionalized by $(l\varepsilon_l)^{1/3}$ [Frisch, 1995, p164]. This assumption is known as the "refined similarity hypothesis". As a consequence of this, all the scaling laws predicted by the K41 theory were modified as follows [Lesieur, 2008, p230]:

$$
\begin{aligned}
&(Two-thirds\ law) \qquad S_2(l) \sim <\varepsilon>^{2/3} l^{2/3}\left(\frac{l}{l_0}\right)^{\chi/9} \\
&(Five-thirds\ law) \qquad E(k) \sim <\varepsilon>^{2/3} k^{-5/3}(kl_0)^{-\chi/9} \\
&(Moments\ law) \qquad S_p(l) \sim <\varepsilon_l^{p/3}> l^{p/3} \sim <\varepsilon>^{p/3} l^{p/3}\left(\frac{l_0}{l}\right)^{\chi p(p-3)/18}
\end{aligned}
\tag{1.21}
$$

where χ is a universal constant and l_0 is the integral scale of turbulence.

Besides the K-O62 model, numerous models have been developed in order to include intermittency effects in the turbulence cascade, some of which employ a (multi)fractal approach to the statistical description of fully developed turbulence. The use of the fractal geometry arises from the energy cascade picture: analogously to a fractal, a single eddy can be seen as a rough part or a fragmented geometric shape that can be subdivided into parts, the daughter eddies, each of which is a reduced size of the mother eddy [Seuront et al., 1999]. When intermittency phenomena occur, not all daughter eddies are generated producing therefore 'gaps' in the hierarchy of cascading eddies leading to a non-uniform distribution in space (or time) of the eddies. As

a consequence of this, the eddies are no longer space-filling and the energy dissipation rate within the inertial range depends on scale l [6].

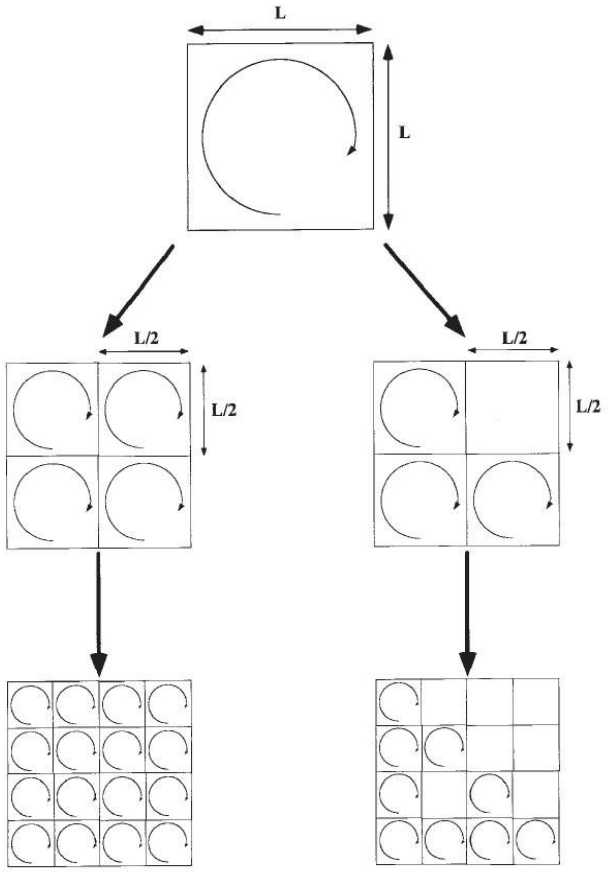

Figure 1.4: Sketch of the turbulent cascade: non-intermittent case (left) and intermittent, mono-fractal case (right). (Image from Seuront et al. [1999])

Frisch et al. [1978] developed one of the first models for intermittent HD turbulence using a fractal approach. This model is called the β-model and makes use of an "intermittency parameter" $\mu = 3 - D_h$, where D_h is the fractal dimension of the system [Mandelbrot, 1977]. Thus, by defying $\beta \in [0, 1]$ as the fraction of daughter eddies of size $l = l_0\, r^n$ produced, where l_0 is the outer

[6] There are several definitions of intermittency in literature, some of which threat the non-constant energy dissipation rate and the non-space-filling nature of turbulence separately. Here we only discuss the definition adopted throughout this thesis for the analyses presented.

scale of turbulence, n is a positive integer and r is typically chosen to be equal to 2 for simplicity[7], then $\beta = r^{\mu}$. For $\beta \longrightarrow 1$, $\mu \longrightarrow 0$ (non-intermittent case) and for $\beta \longrightarrow 0$, $\mu \longrightarrow -\infty$ (intermittent case). Consequently also the structure function scaling exponent, $\zeta(p)$, is subject to modification as follows $\zeta(p) = \mu(1 - p/3) + (p/3)$ [Frisch, 1995, p139].
The β-model was also extended to MHD turbulence by [Ruzmaikin et al., 1995] and, employing the Iroshnikov-Kraichnan model (§ 1.2.4), it yields the following expression for the structure function scaling exponent $\zeta(p) = \mu(1 - p/4) + (p/4)$.

However, the phenomenology of turbulent cascades is rather more complex and mono-fractal models, like the β-model, do not take into account how the activity of turbulence becomes more and more inhomogeneous as we go to smaller and smaller scales[8]. Let us explain this with an example. Figure 1.4 shows the phenomenology of the turbulent cascade with (right) and without (left) intermittency effects. The intermittent case here shown refers to a mono-fractal description of intermittency, such as that used in the β-model. As we can see, mono-fractal models only consider the case for a daughter eddy of a fixed size to be generated or not. It does not consider the intermediate case for which eddies of similar but different sizes can be generated. The latter case would be instead taken into account in a multifractal description of the turbulent cascade as can be seen in Figure 1.5.

One of the first attempts to describe the turbulent cascade by using a multifractal approach was made by Parisi, who suggested that fully developed turbulence possesses only a local scaling invariance, that is, the h exponent in Equation (1.5) can vary at different points of the fluid [Parisi and Frisch, 1985, p84]. This weaken the assumption of global scale invariance made in the K41 theory allowing a wider spectrum of continuous values for h. This led to a multifractal description of fully developed intermittent turbulence. Since then, many multifractal models were developed, the most important of which are

[7] r=2 simply means that one mother eddy at scale l generates two daughters at scale $l/2$.
[8] From an experimental point of view, mono-fractal models are inadequate to describe intermittent turbulence since they lead to a linear dependence of $\zeta(p)$ on p, while experimentally it has been observed a quadratic dependence of $\zeta(p)$ with p or, more generally, a non-linear dependence.

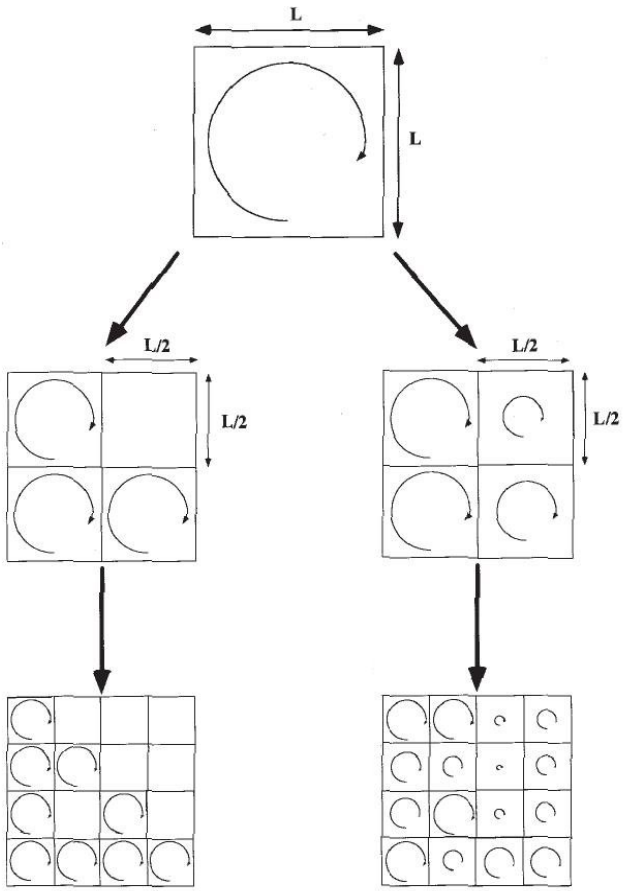

Figure 1.5: Multifractal description of the turbulent cascade: mono-fractal description (left) versus multi-fractal description (right). (Image from Seuront et al. [1999])

the revised β-model by Paladin and Vulpiani [1987], the p-model [Meneveau and Sreenivasan, 1987] and the She-Leveque model [She and Leveque, 1994]. Although there has been progress in the understanding of the intermittency phenomenon, however it is still an open question due to the several controversies on how to quantify it.

In this thesis we adopt the multifractal approach for the detection of intermittency in the turbulence cascade.

1.3.2 The closure problem and non-Gaussianity

Fluid turbulence can be considered as a transition state from a laminar flow in thermal equilibrium to a state very far from it. Small perturbations to an initially laminar flow slightly lead the system away from thermal equilibrium and can be classically treated via the perturbation theory. In contrast, fully developed turbulent flows typically involve perturbations which interact non-linearly with many degrees of freedom leading the system very far from thermal equilibrium. In this case, perturbation theories are no longer adequate. Furthermore, while for systems in or near thermal equilibrium, the total energy is constant, fluid turbulence is instead highly dissipative.
The coupling of the degrees of freedom arises from the non-linear terms in the fluid equations and a consequence of this non-linearity is the non-Gaussian nature of the fluctuations associated with the bulk quantities that describe a turbulent flow.

Let us focus for instance on the HD case by rewriting the Navier-Stoke equation (Eqn. (1.1)) in the following symbolic fashion [McComb, 1990, p6]:

$$L_0 v = L_1 vv + L_2 P, \tag{1.22}$$

where L_0, L_1 and L_2 are differential operators such that $L_0 = \left(\frac{\partial}{\partial t} - \nu\nabla^2\right)$, $L_1 v = -(v \cdot \nabla)$ and $L_2 = -\nabla/\rho$. We ignore external forces and also the vector character of the velocity field for illustrative purposes only. If we now write Equation (1.22) in terms of two-point correlation of the velocity field $< vv >$, then we get the following expression:

$$L_0 < vv >= L_1 < vvv > + L_2 < vP > . \tag{1.23}$$

Multiplying in turn by vv, vvv, ..., before averaging then one obtains a hierarchy of moment equations [McComb, 1990, p7]

$$\begin{aligned} L_0 < vvv >&= L_1 < vvvv > + L_2 < vvP > \\ L_0 < vvvv >&= L_1 < vvvvv > + L_2 < vvvP > \\ L_0 < vvvvv >&= L_1 < vvvvvv > + L_2 < vvvvP > \end{aligned} \tag{1.24}$$

and so on. This leads to the well known closure problem, which is a common problem of all non-linear equations and consists in having one more variable than the actual number of equations needed to solve the system. An important consequence of the closure problem for turbulence is the non-Gaussian nature of the probability distribution of the velocity field fluctuations; indeed, while the statistics of a turbulent velocity field at a fixed point is approximately Gaussian, the two-point, or in general many-point, statistics are typically non-Gaussian [McComb, 1990, p165].
Several attempts to solve the closure problem have since been made by making a closure hypothesis on the four-point correlations [Millionshchikov, 1941] such that

$$< v^4 > \sim \sum < vv >< vv >. \tag{1.25}$$

However this moment-closure assumption implies a near-Gaussian expansion for the turbulence statistics, which is also not consistent with observations. Indeed, experimentally measured PDFs at small scales deviate significantly from Gaussian, and the deviation tends to amplify as the Reynolds number increases [e.g., Monin and Yaglom, 1971, and references therein].

1.3.3 Finite range turbulence

Turbulence is characterized by strong correlations between different length/time scales. This is typically seen as power law scaling arising from the self-similarity of these correlations [Sornette, 2000]. In real situations, however, scaling holds only approximately and a generalized similarity is instead observed.

In fluid turbulence, it has been seen that either when turbulence is not completely evolved (low Reynolds number), the dataset size or the Reynolds number are finite (realistic cases) [Sreenivasan and Bershadskii, 2006] or the system is bounded [Barenblatt, 2004; Cleve et al., 2005], then symmetries in the flow are broken, and the similarity is lost. Thus, finite-size corrections to the scaling laws need to be made [e.g., Grossmann et al., 1994; Dubrulle, 2000; Bershadskii, 2007].
The main reason for which the similarity is lost arises from the fact that Kolmogorov's assumption on the inertial range scales l, that is, $l_\eta << l << l_0$

is no longer valid; indeed, the finite size of the system or parameters implies a finite range of the inertial scales of turbulence for which $l \lesssim l_0$. As a consequence of this, scaling laws at the inertial scales might also depend on the outer scale of turbulence l_0.

We have seen so far that both HD and MHD fully developed turbulence in an infinite medium possess statistical scale invariance at small scales, which leads to power law scaling of the turbulent fluctuations within the inertial range. One of the main consequences of this scale invariance is seen in the various structure functions of order p, which are expected to exhibit the following scaling law:

$$S_p(l) \sim l^{\zeta(p)}, \tag{1.26}$$

where the scaling exponent $\zeta(p)$ is experimentally observed to be a non-linear function of p (intermittent turbulence).
Often, when dealing with real turbulent flows, Equation (1.26) is no longer satisfied and an Extended Self-Similarity (ESS) instead suggests a generalized scaling for the pth moment of the structure function of the form:

$$S_p(l) \sim G(l)^{\zeta(p)}, \tag{1.27}$$

where $G(l)$ is an initially unknown function [e.g., Grossmann et al., 1994; Bershadskii, 2007; Chapman and Nicol, 2009].

ESS was first introduced by Benzi et al. [1993], who observed the following empirical formula

$$S_p(l) = S_q(l)^{\zeta(p)/\zeta(q)} \tag{1.28}$$

to hold the dissipation region of the k spectrum. Successively, it was observed to hold the inertial range of turbulence in both systems of infinite and finite size for which respectively Equation (1.26) and Equation (1.27) are satisfied. This is simply because the ratio of the logarithm of two orders of the structure function defined as in Equation (1.26) (or Eq. (1.27)) does not depend on the function l (or $G(l)$) directly.

The function $G(l)$ is referred to here as the "generalized function" since it arises from a generalized similarity. The latter has been observed in many

systems such as the fast solar wind [Carbone et al., 1996; Kiyani et al., 2007; Nicol et al., 2008; Chapman and Nicol, 2009], where it appears to be insensitive to the details of the flow [Chapman et al., 2009], in laboratory simulations of MHD turbulence [Dudson et al., 2005; Dendy and Chapman, 2006] and in HD turbulence [Grossmann et al., 1994; Bershadskii, 2007]. Moreover, the generalized function points to a characteristic feature of a wide class of scaling processes that show ESS [Dubrulle, 2000]; however there are still several unsolved questions: what does determine its functional form? Is it a universal function or does it depend on the details of the flow?
In this thesis we do not claim to address all these questions, we rather provide analysis tools for the identification and quantification of the generalized scaling in order to investigate its universal features. We also take advantage of the compensate for the generalized function to develop new tests for multifractal intermittent turbulence in real systems.

1.4 The solar corona

1.4.1 Introduction

The atmosphere of the Sun is mainly composed of three layers. From the Sun's surface outward we find: the photosphere, the chromosphere and the corona (see Fig. 1.6). Although these three layers are very close to each other, they are characterized by very different physical parameters. As we can see in Table 1.1, above the photosphere the temperature is about $\sim 4 \times 10^3$K and rises through the chromosphere reaching very high temperatures in the corona. Here the plasma is highly ionized and extends for hundred of thousands of kilometres into the interplanetary space becoming the solar wind.
The reason why the corona has temperatures 200 times hotter than the photospheric temperature and especially how these can be maintained is still an open debate. However, it is widely recognized that the coronal heating is related to the magnetic field's activity [Kivelson and Russel, 1995, p79].

The solar corona is a very inhomogeneous and tenuous layer of plasma transparent to photospheric light, and becomes visible only during total solar eclipses, when the Moon obscures the solar disk. Indeed, the name "corona"

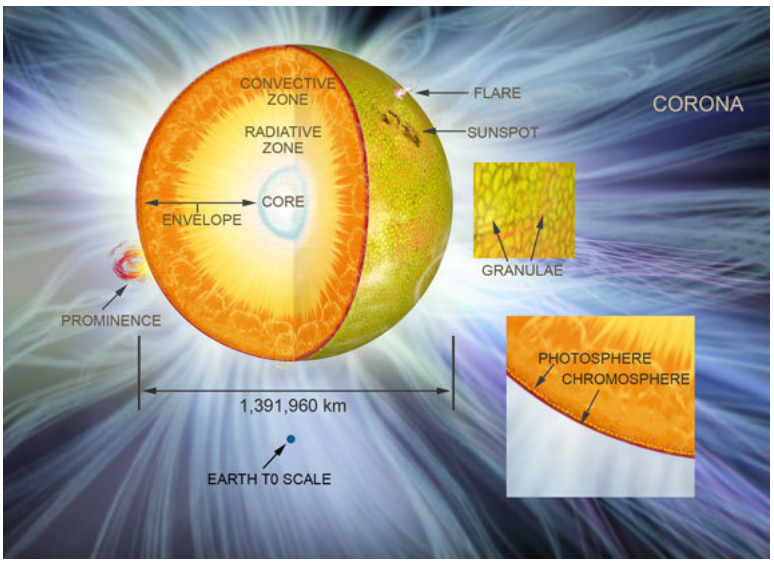

Figure 1.6: Sketch of the Sun's structure. (Image available on line)

Layer	Temperature (K)	Density (m^{-3})	Thickness (Mm)
Photosphere	$\sim 4 \times 10^3$	10^{23}	0.5
Chromosphere	$\sim 10^4$	10^{17}	2.5
Corona	$\sim 10^5 - 10^6$	$10^{15} - 10^7$	-

Table 1.1: Characteristic parameters of the three layers of the Sun's atmosphere [Kivelson and Russel, 1995, p61].

comes from the Latin word for crown, to indicate the halo visible during total solar eclipses (see Fig. 1.7).
In the corona many spectacular as well as energetic phenomena take place. The observed correlation of the coronal structures' variability with the solar cycle led to the conclusion that the coronal dynamics strongly depends on the solar magnetic field [Golub and Pasachoff, 2010, p87]. Thus, in order to understand the physics of the corona, a deeper study of the coronal magnetic field is needed.

1.4.2 Solar magnetic field in the corona

The solar magnetic field controls the dynamics and topology of all coronal phenomena. The coronal plasma is frozen in the magnetic field and there-

Figure 1.7: *Upper panel:* image of the solar corona during a solar eclipse from Mongolia in 2008, when the Sun was at the minimum of its activity. *Lower panel:* zoom of the image in the upper panel. Bright coronal structures, which outline the coronal magnetic field, are visible above the solar limb in contrast with the dark background. (Images courtesy of Miloslav Druckmuller)

fore particles can only move along the field lines. The latter are of two typologies: close magnetic field lines and open magnetic field lines. Close-field regions are mainly placed at low solar latitudes forming the so called coronal loops (see Fig. 1.8). The slow solar wind originates here: the closed field lines act as a constraint for the coronal plasma flow, whose motion outward the Sun's atmosphere into the interplanetary space is therefore slowed down. In contrast, open-field regions lie at high solar latitudes in correspondence of the

poles[9]. These regions are also known as coronal holes as they connect the solar surface with the interplanetary field and are the source of the fast solar wind.

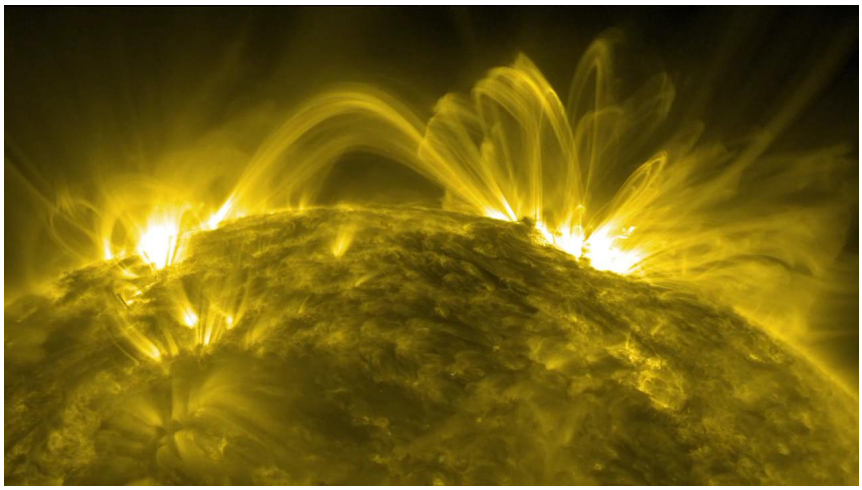

Figure 1.8: Image of the solar corona during solar minimum at 171 Ångström taken with the Solar Dynamics Observatory on July 12, 2012. High density hot loops are seen to outline the magnetic filed lines of the corona.

It is possible to distinguish two main regions in the corona: active regions where the magnetic field is much intense and its force lines appear very bright in the visible, and quite regions where the field is less intense and no important phenomena seem to occur. The strongly localized magnetic field in the active regions generates several magnetic structures and dynamical processes in corona, which are constantly observed by numerous satellites (e.g., SoHO, HINODE, STEREO, SDO) and are matter of study for the development and testing of a broad range of models spanning from the loops oscillations models to the coronal heating models.

A further distinction between two coronal regions is usually made due to its non-uniformity: the upper (or outer) corona and the lower corona. Scientists distinguish these two regions because of the different trend of their physical quantities. In particular, while both the density and magnetic field decrease with the distance going from the lower to the outer corona, it is found

[9]This is almost true during solar minimum, however during solar maximum they can be located anywhere on the Sun.

that the density drops faster in the lower corona and the magnetic field drops faster in the outer corona [Aschwanden, 2004, p204]. Nevertheless, it is quite difficult to experimentally measure the magnetic field in the corona because of its strong non-linearity and the complexity. This is thought to be the result of the coupling between the solar dynamo and the coronal magnetic field [e.g., Pinto et al., 2011] and also due to a persisting photospheric turbulence in the corona [e.g., Abramenko et al., 2008; Dimitropoulou et al., 2009]. Intriguingly, correlations between outer corona and solar wind have also been found in the statistics of large-scale density fluctuations [Telloni et al., 2009] suggestive of a coronal turbulence convected with the solar wind plasma [Matthaeus and Goldstein, 1986].

1.4.3 Coronal structures and phenomena

We have seen so far that coronal structures are dominated by the solar magnetic field. At low latitudes, where the field lines are closed, the most characteristics coronal structures are the loops, which behave as "highlighters" of the magnetic field lines.
Over active regions, the white-light corona also shows huge long-lived particle condensations extending outward the Sun (see Fig. 1.7). These structures are known as "coronal streamers" and occur mainly at the Sun's equator. Among these streamers, more specific structures have been identified as "helmet streamers", which are centered over prominences[10] often separating different magnetic field polarities. Moving toward the solar poles, within coronal holes, plumes are visible. These are outgoing flows similar to jets, which move along the open magnetic field lines and have a lifetime of about 24 hours.
Even though the large-scale coronal structures mentioned above have clear characteristics, however during the maximum of the solar activity they are no longer distinguishable from each other (see Fig. 1.9).

Besides the structures that characterize the corona, the latter is also dominated by large-scale erupting phenomena that can occur suddenly throughout the Sun's atmosphere. These phenomena are commonly associated with bursting events or explosions by which the corona expels X-ray, energy and/or

[10]We shall focus on prominences in detail in the next section.

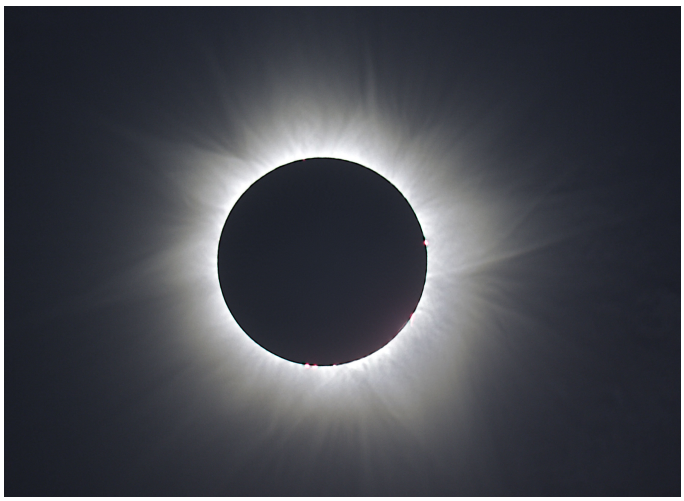

Figure 1.9: Image of the solar corona taken at Clifton Beach during a total solar eclipse in 2012, when the Sun was at the maximum of its activity. (Image courtesy of Wendy Vysma-Gooch and Tony Surma-Hawes)

matter. The former are known as X-ray bursts, while explosions with a subsequent release of energy and/or matter are called respectively flares and Coronal Mass Ejections (CMEs). These three phenomena are often observed to occur simultaneously, however they may also take place independently. In any case, they are strongly related to the coronal magnetic field. Indeed, a change in the magnetic field line configuration determines a restructuring of the coronal structure and a release of energy under the form of accelerated flow, energetic particles and X-ray emission trough the magnetic reconnection process[11]. Figure 1.10, for instance, shows the standard 2D model for flares originally developed by Carmichael and Sturrock [Carmichael, 1964; Sturrock, 1966] and successively re-elaborated by Shibata and Tsuneta [Shibata, 1995; Tsuneta, 1996]. According this model, flares originate in active regions such as prominences, where an initial driver causes the prominence to rise with a consequent transition of the magnetic field from an equilibrium state to a non equilibrium state. Then, the rising prominence stretches generating a current sheet, which is prone to Sweet-Parker or Petschek reconnection.

[11] We shall focus on the magnetic reconnection process in the next section.

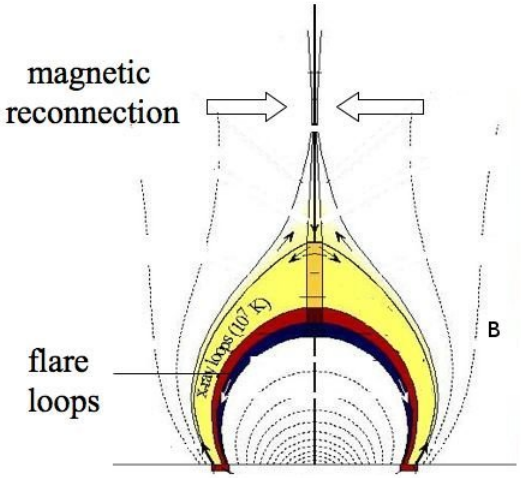

Figure 1.10: Standard 2D model for flares.

1.4.4 Solar prominences

Solar prominences or filaments are relatively cool, dense plasma structures in the lower solar corona with temperatures of about 10^4 K. Solar filaments can be seen on the disk, whilst prominences are observed above the solar limb (see Fig. 1.11). In practice, they are classified in three main categories according to their location on the Sun, namely active, intermediate and quiescent. The latter usually occur on the quiet Sun at high latitudes and consequently are also known as "polar crown" prominences, while active and intermediate filaments are often observed at low latitudes associated with active regions [Engvold, 1998]. All prominences originate from filament channels and develop above the polarity inversion line showing many different morphologies and dynamics [see Mackay et al., 2010, for a recent review]. In particular, some observations of filaments on the disk show that they are mainly composed of thin horizontal threads [e.g., Zirker et al., 1998; Lin et al., 2005], while others show vertically striated prominences often associated with up and down flows [e.g., Engvold, 1981; Martres et al., 1981]. There is as yet no physical framework to explain how these relatively cool plasma structures

reach coronal heights and maintain there, suspended against gravitational free fall.

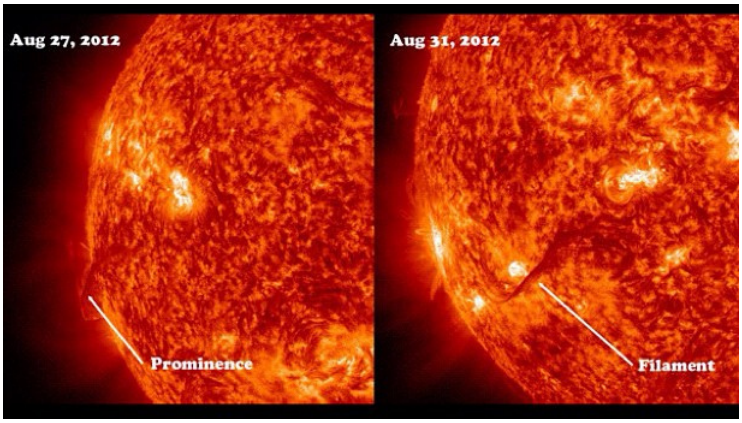

Figure 1.11: Images of the Sun taken by SDO on August, 2012 showing a solar prominence (left) and a filament (right), which is nothing else than the same structure seen on the solar surface three days later after the Sun rotation.

Many models have been developed to describe possible scenarios for the production and maintenance of such dynamical structures in the corona and the local magnetic field is suggested to play a key role as it is thought to be the driver of the prominence threads [e.g., Low and Hundhausen, 1995; Foullon et al., 2009; Hershaw et al., 2011]. Recently, in strongly inhomogeneous coronal plasma structures, processes such as magneto-thermal convection in solar prominences [Berger et al., 2011] and Kelvin-Helmholtz instabilities in the corona [Foullon et al., 2011] have been suggested as mechanisms for the generation of such dynamical structures. In particular, Berger et al. [2010] showed that quiescent prominences (QPs) often exhibit highly variable dynamics characterized by several up-flows and vortices suggestive of turbulence. The latter, indeed, could be the reason for the continuous formation process of QPs.
In Chapter 3 we shall test this idea by applying statistical analyses to one of the QPs discussed in Berger et al. [2010] in order to detect and quantify its presumably turbulent nature.

1.5 Magnetic reconnection

Magnetic reconnection is an ubiquitous process in both astrophysical and laboratory plasmas. Experimentally it has been observed that driven plasmas can show changes in their magnetic field topology along with a release of energy [e.g., Dungey, 1961; Dere, 1996; Browning et al., 2008]. One of the main proposed mechanisms for the change of the magnetic field topology is magnetic reconnection. During this process, two oppositely directed magnetic field lines approach each other, stretch, then break and reconnect changing their topology (see Fig. 1.12); consequently, the magnetic field energy stored in the force lines is released and rapidly converted into thermal and kinetic energy [Priest and Forbes, 2000, and references therein].

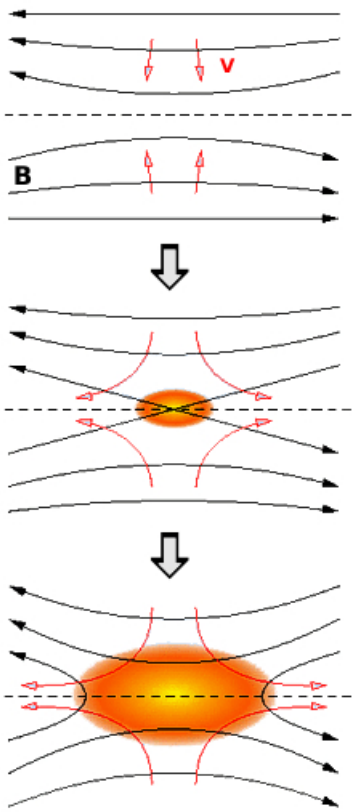

Figure 1.12: Schematic view of the reconnection process. Two oppositely directed magnetic field lines approach each other (top), then break (center) and reconnect (bottom).

For an ideal MHD flow, for which the resistive term $\mathbf{J}/\text{œ}\mathbf{e}$ is negligible compared to the other terms in Equation (1.16), the induction equation (Eqn. (1.17)) reduces to the following expression:

$$\frac{\partial \mathbf{B}}{\partial t} = \nabla \times (\mathbf{v} \times \mathbf{B}), \tag{1.29}$$

where the term $\lambda \nabla^2 \mathbf{B}$ has been neglected for finite values of the resistivity $\eta = 1/\sigma = \lambda\mu$, in the MHD limit of large length scales ($L \longrightarrow \infty$). As a consequence of this, the magnetic lines of force are 'frozen-in' and move with the flow, therefore a change of the magnetic field topology is not permitted because it would require a change of the magnetic flux within the frame of the plasma. This is also known as the Alfvén's theorem.
However, magnetic reconnection processes have been observed to take place in many astrophysical environments (e.g., magnetospheres, solar flares) and laboratory experiments (e.g., tokamaks) in which the plasma can be considered quasi-ideal [Yamada et al., 2010]. In these systems, indeed, current sheets of finite size (L small) generate, which invalidates the MHD limit leading to the break down of the Alfvén's theorem. Hence, the ideal MHD description of the reconnection process is not adequate and models using the Hall MHD, two-fluid or the Vlasov theory are needed.

The electromagnetic energy released during a the reconnection process can be derived by using the Ohm's law (Eqn. (1.16)). Manipulating this equation we get the following expression:

$$\mathbf{E} \cdot \mathbf{J} = -\mathbf{v} \cdot (\mathbf{J} \times \mathbf{B}) + \frac{J^2}{\sigma}. \tag{1.30}$$

For a steady state $(\nabla \times \mathbf{E}) = 0$, therefore we can write the term on the l.h.s. of Equation (1.30) as follows:

$$\mathbf{E} \cdot \mathbf{J} = -\nabla \cdot (\mathbf{E} \times \mathbf{H}), \tag{1.31}$$

where $\mathbf{H} = \mathbf{B}/\mu$ and $\nabla \cdot (\mathbf{E} \times \mathbf{H})$ is the Poynting flux, which expresses the rate of inflow of electromagnetic energy per unit area. Thus combining Equations (1.30) and (1.31) and integrating over the diffusion region, we can deduce that the inflow electromagnetic energy $\mathbf{E} \cdot \mathbf{J}$ into a volume produces ohmic heat J^2/σ

and work done by the Lorentz force $\mathbf{J} \times \mathbf{B}$. Reconnection is thus a mechanism which both accelerates particles and thermally heats the plasma.
A time-scale for magnetic dissipation, τ_d, can be obtained from the induction equation (Eqn. (1.17)) by equating the magnetic time derivative and the dissipation term (second term on the r.h.s.), leading to the following expression $\tau_d = L^2\mu/\eta$. However, estimations of the dissipation time in real systems where reconnection occurs (e.g., in the magnetosphere, solar flares, CME, etc) are inconsistent with such expression as this phenomenon is observed to take place much faster. This inconsistency has led many physicists to develop several models, which can be divided in two main categories: models for steady reconnection and models for unsteady reconnection.

1.5.1 Steady reconnection

The first qualitative model of reconnection was formulated by Parker [1957] and Sweet [1958]. This model employs a 2D steady state MHD description of the reconnection process which occurs in a small area within the current layer, that is, the diffusion region of length $2L$ and width $2l$ (see Fig. 1.13). During this process, the plasma flows into the dissipation region at a speed v_i, the inflow speed, and leaves at speed v_o, the outflow speed. Conservation of mass then implies that $Lv_i = lv_o$. Since the magnetic force accelerates the plasma to the Alfvén speed, V_A, then it can be demonstrated that $v_o \approx V_A$ at the inflow. Then the Sweet-Parker model anticipates a reconnection rate, v_i/v_o, proportional to $S^{-1/2}$, where $S \sim LV_A/\lambda$ is the Lundquist number at the inflow. Therefore, the larger is L the slower is the reconnection process.
In astrophysical environments where reconnection takes place, such as solar flares, L is normally large, while λ is thought to be very small; hence, the release of magnetic energy would be expected to occur in a time of the order of 10^7 years [Giovanelli, 1946]. On the contrary, experimentally, this time has been observed to be few Alfvén time scales $t_A = L/V_A$, thus much faster than the time anticipated by the Sweet-Parker model.

In 1964, Petschek proposed a new theoretical MHD model for 2D reconnection. This model anticipates the presence of standing-slow mode waves, which would generate shocks at the edges of the current layer converting the

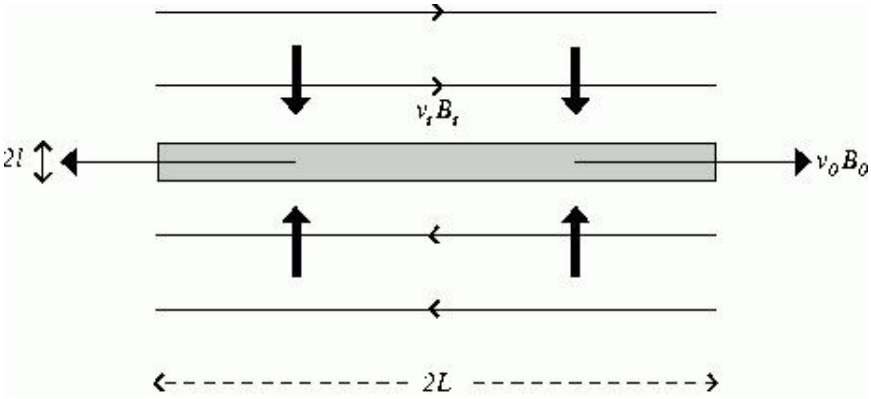

Figure 1.13: Sweet-Parker reconnection. The shaded rectangle represents the diffusion region, while the black arrows indicate the inflow (thick) and the outflow (thin) plasma velocity.

magnetic energy into kinetic energy [Petschek, 1964]. Importantly, this model assumes that the diffusion region is not equal to the global scale $2L$, as in the Sweet and Parker model, but it is limited to a small segment (localized resistivity). As a consequence of this, the reconnection rate v_i/v_o is proportional to $1/log(S)$; since $log(S)$ varies slowly, then the reconnection rate is much larger than the Sweet-Parker rate, allowing the process to proceed much faster. Since then, it is referred to such process as "fast magnetic reconnection", for which rates typically range between 0.01 and 0.1.

Although the Petschek model was accepted for several years, however it lacks of an appropriate treatment of the diffusion region; indeed, Petschek's solution in the outer region is correct and stable, but it does not match to the diffusion layer for small η. Thus, numerous modifications to the Petschek model were formulated (i.e. Petschek-like models of fast reconnection), which make use of an "anomalous" resistivity, $\eta_X = O(1)$, that is, a locally strong resistivity in proximity of the X-point [Biskamp, 1993, p137]. Drake et al. [2006] also proposed that the Hall electric field along with whistler waves are required in order to set up the original Petschek scheme: the dispersive properties of the whistler waves permit the flux of electron through the inner diffusion region to remain finite, even as the dissipation approaches zero. However, rates consistent with fast reconnection have been shown either without employing the Hall term in hybrid simulations [Karimabadi et al., 2004] and in electron-positron

plasmas in absence of whistler waves [Bessho and Bhattacharjee, 2005]. Hence, determining whether the resistivity is either uniform (Sweet-Parker model) or localized (Petschek model) is crucial to fully understand the dynamics of the dissipation region and therefore to model the reconnection process.

Recently, high performance supercomputers have allowed deeper studies of the reconnection process via numerical simulations spanning from MHD to kinetic regimes. These simulations have shown that for Lundquist numbers greater than a critical value, $S_{crit} \sim 10^4$, the initial current sheet becomes unstable giving rise to instabilities [Loureiro et al., 2007; Lapenta, 2008; Bhattacharjee et al., 2009; Daughton et al., 2009; Huang and Bhattacharjee, 2010]. Then, the hypothesis of a time-dependent scenario have arisen, which will be discussed in the next section.

1.5.2 Unsteady reconnection

As larger kinetic simulations became possible, one interesting result was that magnetic reconnection evolves non-linearly becoming unstable to plasmoids [e.g. Daughton et al., 2006; Shay et al., 2007, and references therein]. Diffusion processes can drive three different types of resistive instabilities: gravitational, rippling, and tearing mode [Furth et al., 1963].
In particular, tearing instabilities may occur during reconnection processes within current sheets whose thickness satisfies the following relation $t_d \gg t_A$; consequently, magnetic structures such as islands in 2D (see Fig. 1.14) or flux ropes in 3D, generate while magnetic energy is released.

Secondary tearing instabilities have also been observed in a variety of 2D kinetic simulations of reconnection, which have shown that electron-scale current sheets become unstable to the formation of magnetic structures on multiple scales [Daughton et al., 2006; Drake et al., 2006; Karimabadi et al., 2007; Klimas et al., 2008]. This has led to the so called "fragmentation process" [Bárta et al., 2010], for which the current sheet is fragmented to smaller and smaller plasmoids trough tearing instabilities (see Fig. 1.15). Besides this "plasmoid instability" [Loureiro et al., 2007; Uzdensky et al., 2010], also called "cascading reconnection" [Shibata and Tanuma, 2001], an inverse cascade process is also observed to occur, namely, the coalescence process [Kliem et al.,

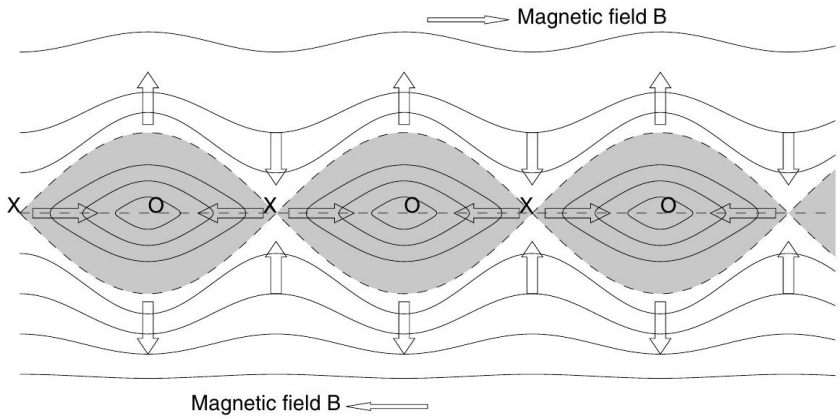

Figure 1.14: Magnetic island formation by tearing-mode instability during the reconnection process. Magnetically neutral X and O points are formed at the boundary between regions of oppositely directed magnetic field lines. Arrows indicate the direction of the plasma flow. (Image from Aschwanden [2004], p415)

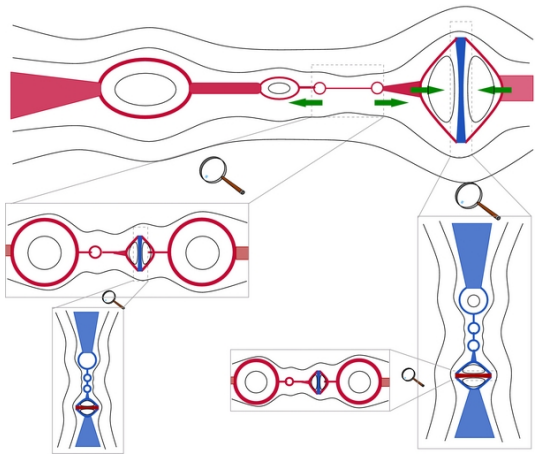

Figure 1.15: Schematic view of the fragmentation process of the current sheet via tearing and driven coalescence processes from Bárta et al. [2011]. Increasing rescaling shows similar kinds of processes repeating on smaller scales. Red and blue areas of various hue indicate various intensities of the positive and negative out-of-plane component of current density, respectively.

2000; Bárta et al., 2011; Karlický and Bárta, 2011; Karlický et al., 2012]. The latter consists in the formation of a larger magnetic structure from two smaller

merging plasmoids.
In some cases, these two processes, fragmentation and coalescence, have been observed to be connected (fragmenting coalescence) [Karimabadi et al., 2011]: the current sheet fragmentation is unstable to small plasmoid formation, which can eventually merge leading to the formation of one single thin current sheet (coalescence); successively, the latter can again be unstable to fragmentation and so on. This scenario has led to a fractal approach to the reconnection process [Materassi and Consolini, 2007; Klimas et al., 2010] as well as the formulation of models that take into account the development of turbulence.

1.5.3 Turbulent reconnection

It is well known that the majority of astrophysical plasmas are highly turbulent. Turbulence is suggested in coronal dynamics, solar wind, dynamo processes and so on. It has been observed that in some of these systems also magnetic reconnection phenomena take place, suggesting that these two processes, turbulence and reconnection, are strictly correlated [Matthaeus and Velli, 2011; Servidio et al., 2011]. Both numerical simulations and observations seem to support this idea [e.g., Chaston et al., 2009; Chang et al., 2011; Huang et al., 2012, and references therein]. In particular, attempts to reproduce magnetic reconnection processes through laboratory simulations have shown that the influence of turbulence is crucial in the understanding of such phenomenon.

Depending on the application, the turbulence may arise from a spectrum of instabilities within the reconnection layer or from pre-existing magnetic fluctuations in the ambient plasma. Within the MHD model, there has been progress on both ideas - either by starting with a laminar current sheet to explore instabilities [Loureiro et al., 2007; Lapenta, 2008; Bhattacharjee et al., 2009; Huang and Bhattacharjee, 2010] or by directly driving turbulence [Matthaeus and Lamkin, 1985, 1986; Loureiro et al., 2009; Eyink et al., 2011]. In the first case, turbulence is thought to contribute to the energy transport generating coherent structures during the reconnection process but without having any strong implications for the dissipation process and the reconnection rate growth, while in the second case the presence of turbulence is believed

to be the cause of the fast evolution of the reconnection process. The LV99 model proposed by Lazarian and Vishniac [1999], for instance, falls in the latter case. Importantly, the LV99 model is based on the fact that reconnection

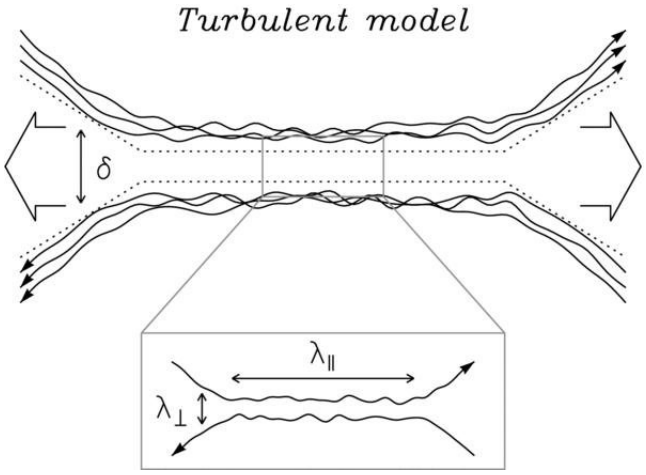

Figure 1.16: Sketch of turbulent reconnection from Kowal et al. [2009].

occurs in astrophysical fluids which are generically turbulent; therefore realistic studies of astrophysical magnetic reconnection should include the effects of stochastic magnetic field. According to this model, indeed, the shuffling of the magnetic field lines induced by the turbulence, leads to a, at least weakly, stochastic field, which allows many magnetic field lines to enter the reconnection zone simultaneously enabling fast reconnection (see Fig. 1.16). The degree of magnetic field stochasticity thus controls the reconnection rate which is fast independently on the presence or absence of anomalous plasma effects [Lazarian et al., 2012]. The LV99 model has been tested in a broad variety of MHD simulations of collisionless reconnection with pre-existing turbulence, where it has been shown the dependency of the reconnection speed on the level of the turbulence power [Kowal et al., 2009; Lapenta and Lazarian, 2012; Kowal et al., 2012].

Moving beyond these MHD models into kinetic regimes, most research has focused on initially laminar current sheets within a variety of descriptions [Birn et al., 2001] including two-fluid, hybrid and fully kinetic simulations. The latter, in particular, allows a complete description of the electron physics responsible for breaking the frozen-flux condition in collisionless parameter

regimes [Hesse et al., 1999; Pritchett, 2001]. Fully kinetic PIC simulations of collisionless reconnection in 3D have demonstrated that the tearing instability within these electron layers has much greater freedom to develop than in the 2D case, giving rise to numerous magnetic flux ropes [Daughton et al., 2011]. The subsequent non-linear interaction of these flux ropes is seen in the simulations to lead to a self-generated turbulence.

In Chapter 4, we shall present analyses of the reconnecting fields of these PIC simulations performed by Daughton et al. [2011] in order to test for turbulence.

Chapter 2

Experimental Methods

2.1 Introduction

In the previous chapter we saw that turbulence is a non-linear process governed by deterministic equations. The non-linearity is responsible for the interaction of numerous modes excited during the process - i.e. coupling of the degrees of freedom - leading to an unpredictable evolution of the system. Consequently, data measurements of the corresponding physical observables exhibit an irregular, seemingly random, behaviour on a certain range of time/space scales. In addition, both experimental and simulation data of physical systems are also affected by mainly stochastic uncertainties - i.e. random error - which introduce uncertainty into the data and may obscure the characterization of turbulence.
Nevertheless, both turbulence and the majority of the stochastic processes show the statistical property of scale invariance, which is an exact form of self-similarity. A direct consequence of this scale invariance is that the characteristic quantities of self-similar processes exhibit a wide variety of scaling laws, each of which identifies a subclass of scaling processes. Hence, in principle, an adequate statistical approach would fully quantify the statistical scaling properties of the process under study and eventually distinguish it from other scaling processes.

In this chapter we present a statistical approach for the study of a general class of self-similar and quasi self-similar processes. In particular, we introduce some powerful statistical techniques for the identification and quan-

tification of scaling in both finite range turbulence and stochastic processes such as Brownian motion, and discuss how they can be distinguished.

2.1.1 Self-similarity and fractals

The statistical property of self-similarity is a property of a process, for which each sub-part of it is statistically similar to the whole [Sornette, 2000, p29]. If the variation in one direction scales differently to the variation in another direction, it is referred to as self-affine [Mandelbrot, 1985]. Hence, self-similar processes are isotropic.

The most basic example of a self-similar object is a fractal. The word fractal comes from the Latin word "fractus", which means fragmented; indeed, this term was first coined by Mandelbrot to describe the rough and irregular geometrical shape of real objects such as mountains and clouds, which do not have perfect Euclidean geometric shapes [Mandelbrot, 1977]. In an attempt to measure the length of the Britain's coastline, Mandelbrot noticed that measured metric properties, such as length or area, are not invariant as postulated for the Euclidean geometry, but are a function of the measuring scale [Mandelbrot, 1982]. Indeed, when measured at a given spatial scale d, the total length of a fragmented coastline $L(d)$ is estimated as a set of N straight-line segments of length d. Then, if we increase the spatial resolution, we would be able to appreciate more details of the coastline and its length $L(d)$ would be observed to increase as the scale of measurement d increases. Specifically, Mandelbrot found the following relation between $L(d)$ and d [Mandelbrot and Wheeler, 1983]:

$$L(d) = Cd^{(1-D_h)}, \tag{2.1}$$

where C is a constant and D_h is known as the fractal dimension, or Hausdorff dimension, which is a non integer (fractional) number. Hence, Mandelbrot defined a fractal set as a set for which the Hausdorff dimension D_h is greater than its topological dimension D_T.
Originally, the fractal dimension D_h was considered to be constant, however it was successively found that in Nature there are much more complex fractals, which exhibit locally variations of the Hausdorff dimension D_h within the fractal set; these are termed multifractals [Sornette, 2000, p120]. Figure 2.1

shows an example of a multifractal field. Each colour in Figure 2.1 corresponds to a single value of D_h (fractal); the superimposition of fractal patterns with different values of D_h leads to a multifractal field.

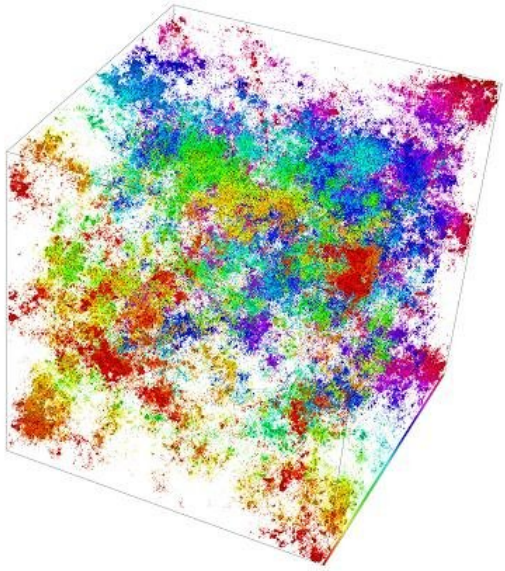

Figure 2.1: Example of a 3D multifractal field associated with an electronic eigenstate at the Anderson localization transition. (Image from Vasquez et al. [2008]).

The Hausdorff dimension is the main quantity used to describe the fractal geometry and, more in general, irregular shapes. It quantifies the complexity of irregular patterns and distinguishes fractal from multifractal geometries as we describe below.
Many methods exist to compute the fractal dimension. Here we only discuss the most frequently and most popular method used, that is, the box-counting method, which is also one of the analysis tools used in this research work (see Chapter 4).

The box-counting method was first introduced by Russel [1980] and applies to datasets of any dimension: vectors, 2D data (e.g., images), data cube, etc. It consists of three main steps:

- convert the original signal into a binary signal - i.e. zeros and ones;

- mash the signal with various boxes of size L using a regular grid;
- count the number of boxes $N(L)$ that contain non-zero values.

$N(L)$ is then the analogue of a mass counter. Thus, the fractal dimension D_h is estimated as

$$D_h = -\lim_{L \longrightarrow 0} \frac{ln(N(L))}{ln(L)}. \tag{2.2}$$

For fractal geometries D_h is constant, while it varies with L for multifractal geometries.

We shall see later in this chapter that there are other methods to quantify the multifractal character of a given field/process, namely, the calculation of the moments of the structure function.

2.2 Signal processing: deterministic processes and noise

A classical physical system is described by all its possible states $x(t)$ with $t \in \Omega$, where Ω is the phase space of the system. Then the time evolution of the system is given by the following differential equation:

$$\frac{d}{dt}x(t) = \mathbf{F}(x(t)), \tag{2.3}$$

where $\mathbf{F}$ is a time independent vector field that establishes the type of time evolution of the systems and can either be a linear or non linear function of the state $x(t)$ [1].

For the case where time is a discrete variable, then the analogue of Equation (2.3) is the map

$$x_{n+1} = \mathbf{f}(x_n), \quad n \in Z \subset \Omega \tag{2.4}$$

where also $\mathbf{f}$ is a time independent vector field.

Experimentally one does not have direct access to the states $x(t)$ due to the fact that the observables of any physical system are always contaminated

[1] Under regularity conditions on $\mathbf{F}$, Equation (2.3) is usually referred to as a flow [Kantz and Schreiber, 1997, p31].

by different kind of noises. The latter can be classified into two main categories: additive noise and multiplicative noise. The deterministic equation for the temporal evolution of a system then becomes a stochastic differential equation of the form:

$$\frac{d}{dt}x(t) = \mathbf{F}(x(t)) + \eta(t), \tag{2.5}$$

for the additive noise, and

$$\frac{d}{dt}x(t) = \mathbf{F}(x(t)) + \mathbf{G}(x(t))\eta(t), \tag{2.6}$$

in the case of multiplicative noise, where $\eta(t)$ is a fluctuating random variable (noise) and $\mathbf{G}$ is a vector field that determines the coupling of the noise to the dynamical state variable $x(t)$. Equation (2.5) is known as the Langevin equation as it was first used by Langevin to describe the Brownian motion. We shall return to this in the next section.

One of the difficulties with data modeling is that one does not know a priori the source of the noise $\eta(t)$ and, in case of multiplicative noise, one needs to make assumptions on the functional form of $\mathbf{G}$ in order to quantify the effects of the noise on the observables of the system. The accuracy of these assumptions can then be tested by looking at the agreement between the theoretical models and the experimental data.
On the other hand, if the statistical properties of the random variable $\eta(t)$ are experimentally accessible, then one can identify the stochastic process associated with $\eta(t)$ and possibly determine the source of the noise.

2.2.1 Stochastic processes: an overview

Given a random variable $x(t)$ at time t, a stochastic process (or random process) is defined as all the possible transitions of the state $x(t)$ to a state $x'(t')$ at time t' with $t \neq t'$. The probability of one state to transit to the next is given by transition probability density function $f(x,t) = p(x',t'|x,t)$. A Markov process, for instance, is a stochastic process for which the transition probability to a future state only depends on the present state, not on the past.

Stochastic processes can be described via Stochastic Differential Equa-

tions (SDEs) which, provided the initial conditions, determine the time evolution of the probability density function $f(x,t)$. An example of a SDE is the Fokker-Plank equation[2], which mathematically describes a diffusion process and, in one dimension, can be written as follows [Gardiner, 2004, p118]:

$$\frac{\partial}{\partial t}f(x,t) = -\frac{\partial}{\partial x}[A(x,t)f(x(t))] + \frac{1}{2}\frac{\partial^2}{\partial x^2}[B(x,t)f(x(t))], \tag{2.7}$$

where $A(x,t)$ is a drift vector, whilst $B(x,t)$ is the diffusion matrix.

The most basic example of diffusion process is the standard Brownian motion (or Wiener process), which is a Markov process continuous in space and time governed by the Fokker-Plank equation with no drift ($A(x,t) = 0$) and constant diffusion coefficient $B(x,t) = D$ [Gardiner, 2004, p66]. It was named after the botanist Robert Brown, who described the random path of a pollen grain suspended in a fluid and moving under the influence of random forces caused by the collisions with the neighbouring molecules induced by thermal fluctuations [Gardiner, 2004, p2].

Let us consider first the random walk of a particle moving in one dimension on a line and taking steps to the right or to the left with equal probability. Then we define the following process

$$X_n \equiv \sum_{i=1}^{n} Y_i, \tag{2.8}$$

with $X_0 = 0$, where Y_i is an independent identically distributed (*i.i.d.*) random variable in $\Re$ and represents the ith step made by the particle, that is, $Y_i = x_{n+1} - x_n$. Then, for the Central Limit Theorem (CLT) [Gardiner, 2004, p37], as $n \longrightarrow \infty$

$$\frac{X_n}{\sqrt{n}} \longrightarrow N(0,\sigma^2), \tag{2.9}$$

where $N(0,\sigma^2)$ ia a Gaussian distribution with zero mean and standard deviation σ.

The Brownian motion B_t is defined as the "continuous" analogue of the

[2]The Fokker-Plank can also be derived from the Langevin equation [see p96 of Gardiner, 2004, for further details].

random walk, that is[3]

$$B_t \equiv \lim_{\Delta t \longrightarrow 0} X_n. \tag{2.10}$$

If we look at the process X_n in rescaled time $t = n\Delta t$ and space $x = b\Delta x$, then for $\Delta t \sim 1/n$ we should choose $\Delta x \sim 1/\sqrt{n} = \sqrt{\Delta t}$ so that the CLT ensures the convergence of the process $\Delta x X_{[t/\Delta t]}$ to a t-dependent random variable as $\Delta t \longrightarrow 0$, namely

$$B_t = \lim_{\Delta t \longrightarrow 0} \sqrt{\Delta t} X_{[t/\Delta t]} = \lim_{\Delta t \longrightarrow 0} \frac{\sqrt{t}}{\sqrt{t/\Delta t}} \sum_{i=1}^{[t/\Delta t]} Y_i \longrightarrow N(0, t\sigma^2). \tag{2.11}$$

The most general scaling between time and space can be written as

$$\Delta x = \Delta t^H, \tag{2.12}$$

where H is a real number in (0, 1), called the Hurst exponent. In order to the above limit to converge for the CLT, the Brownian process must have $H = 1/2$ [Kantz and Schreiber, 1997, p97]. Indeed, other values of H would lead to an either non-existing or degenerating limiting process: for $H > 1/2$, $B_t = 0$, while for $H < 1/2$, B_t is not defined. Hence, for $H = 1/2$ the Brownian motion is a well defined process $B = \{B_t : t \geq 0\}$ (t to be considered as a continuous index), which has a continuous, although non-differentiable, sample path [Gardiner, 2004, p68]. Furthermore, it has the following properties:

- stationary increments: $B_t - B_s \sim B_{t-s} - B_0$;
- independent increments: $B_t - B_s$ is independent of $\{B_u : u \leq s\}$, for all $t \geq s \geq 0$;
- $B_t \longrightarrow N(0, t\sigma^2)$.

Figure 2.2 shows the sample paths of several realization of a Wiener process $W(t) = B_t$. If we looked at the projections on the x and y axis of each $W(t)$ we would be able to appreciate the property of self-affinity arising from the different rescaling along the x and y axes, that is, $\Delta x = \Delta t^{1/2}$.

[3]Notice that the limit properties for a stochastic process are established by the Ito calculus [Gardiner, 2004, p80].

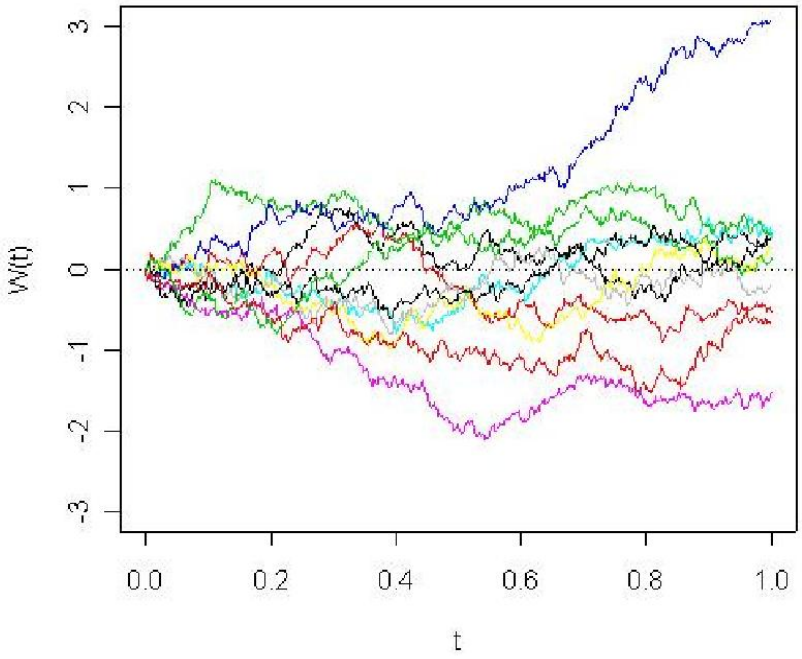

Figure 2.2: Simple paths of a Brownian motion obtained by several realizations of a Wiener process. (Image courtesy of Stefan Grosskinsky)

Therefore the standard Brownian motion is a scaling process showing self-affinity, that is, for every $\lambda > 0$, $\left\{B_t^{(\lambda)} \equiv \lambda^{-H} B_{t\lambda} : t \geq 0\right\}$ with $H = 1/2$ [Bhattacharya and Waymire, 2008, p141]. It is straightforward to note that it also possesses fractal properties; indeed, the fractal dimension of the Brownian motion can be expressed as $D_h = d - H$, where d is the dimension of an embedding space [Sornette, 2000, p30]. For the Wiener process $d = 2$ and therefore the fractal dimension D_h is equal to $3/2$ which is, consistently with the definition of fractal, a value grater that the topological dimension D_T (in this case $D_T = 1$).

We now determine the time correlation function Γ_{ts} for the Wiener process as

$$\Gamma_{ts} = < B_t B_s > - < B_t >< B_s > \tag{2.13}$$

$$= < B^2 > - < B >^2 \delta_{ts} = \sigma^2 \tag{2.14}$$

It can be also demonstrated that for the standard 1D Brownian motion $\sigma^2 = 2Dt$ [Sornette, 2000, p25]. The diffusion process described by the Fokker-Plank equation for a Wiener process then evolves in time by spreading an initially sharp Gaussian PDF with increasing time t (see Fig. 2.3). This is a

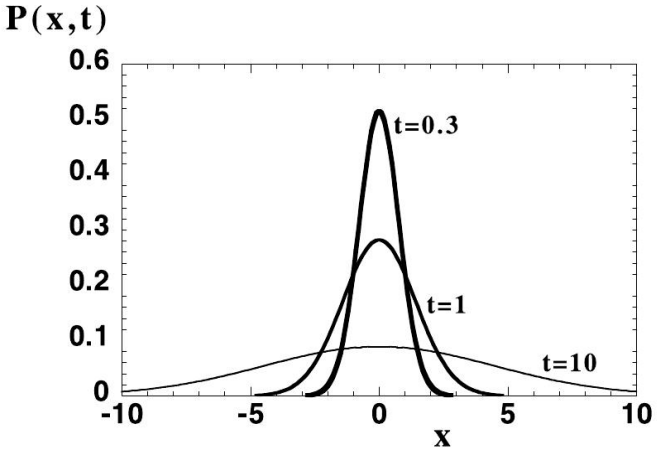

Figure 2.3: Solution of the Fokker-Plank equation, $f(x,t) = P(x,t)$, for a Brownian walk with no drift and diffusion coefficient D=1. Three times are shown, namely, $t = 0.3$, 1 and 10. (Image from Sornette [2000], p33)

direct consequence of the Markov property of a Brownian process, that is, the Brownian walk rapidly diffuses away from the starting point with no memory of the initial conditions and through a series of steps uncorrelated each others (steps to be considered continuous).
If we take the time derivative of the Wiener process[4], we then define the so called white noise or uncorrelated Brownian noise $\xi(t)$, namely

$$\frac{d}{dt}W(t) = \xi(t). \tag{2.15}$$

Thus, if we go back to the Langevin equation (Eqn. (2.5)), its original form

[4]Note, in order the white noise to exist, the Wiener process must be integrable $\xi(t) = \int_0^t W(t')dt'$, however we saw that the Brownian motion has a nowhere differentiable sample path. Nevertheless, it is possible to define the Ito stochastic integral [see Gardiner, 2004, p84], which allows to interpret $\xi(t)$ as real noise with finite correlation time.

describing the Brownian motion has the following expression [Langevin, 1908]

$$m\frac{d^2}{dt^2}x(t) = -\lambda\frac{d}{dt}x(t) + \xi(t), \tag{2.16}$$

where m is the mass of the Brownian particle and λ is a constant coefficient. The white noise $\xi(t)$ can be either additive or multiplicative and is always characterized by a Gaussian probability distribution.

The Wiener process can be generalized to a continuous-time Gaussian process with correlated increments. Such process was first introduced by Mandelbrot and van Ness [1968] and is known as fractional Brownian motion (fBm), or fractal Brownian motion. For a fBm the time correlation function Γ_{ts} is

$$\Gamma_{ts} \;=\; \frac{\sigma^2}{2}\left(|t|^{2H} + |s|^{2H} - |t-s|^{2H}\right). \tag{2.17}$$

For $H = 1/2$ the process reduces to the Wiener process, whilst for $H > 1/2$ and $H < 1/2$ the increments of the process are respectively correlated and anti-correlated. The process defined by the correlated increments of a fBm $F = \{B_{n+1} - B_n : n \geq 0\}$ with $H \neq 1/2$ gives rise to the so called fractional Gaussian noise.

The Wiener process can be easily extended to allow a non zero (linear) drift of the form $A(x,t) = kx$, where k is a positive constant. Such a process is properly named Ornstein-Uhlenbeck process $U(t) = \{U_t : t \geq 0\}$. This is still a continuous Gaussian process but for which the Markov property is slightly relaxed, that is, the increments are more persistent with respect to the Wiener process. The drift term indeed acts as a "restoring force" tending to bring the Brownian particle back to the origin, reaching therefore a stationary state. As a consequence of this, the process has a correlation function which depends only on time differences [Gardiner, 2004, p77]

$$\Gamma_{ts} = < U_t U_s > - < U_t >< U_s > = \frac{D}{2k}(e^{-k|t-s|}). \tag{2.18}$$

The Ornstein-Uhlenbeck process is then a stationary Gaussian process which converges to the Brownian motion in the limit of $t \longrightarrow \infty$. The states of the process U_t and U_s are then said to be significantly correlated if $|t-s| \sim 1/k \equiv \tau$, where τ is the correlation time [Gardiner, 2004, p77].

Analogously to the white noise, the time derivative of the Ornstein-Uhlenbeck process gives rise to the so called "coloured noise" $\bar{\xi}(t)$, namely

$$\frac{d}{dt}U(t) \equiv \bar{\xi}(t) = \sqrt{\frac{2\sigma^2}{\tau}}\xi(t), \tag{2.19}$$

where $\xi(t)$ is the Brownian white noise. The coloured noise thus is characterized by two parameters, σ and τ and shows scaling properties and fractality as the uncorrelated Brownian motion.

White noise and coloured noise often affect the measurement of physical observables, therefore it is important to identify their properties in order to predict their effects on the data.
In the next sections we shall introduce some statistical methods which allow to detect and quantify the statistical properties of the stochastic processes here discussed.

2.3 Spectral analysis

One of the most common analyses for signal processing is spectral decomposition. It consists in the analysis of a signal in the frequency domain. The one-to-one correspondence between a signal $s(t)$ in real space at time t and its representation in the frequency domain $s(f)$ at frequency f is given by the Fourier Transform (FT)[5]. The Fourier analysis enables us to identify periodicities by determining which frequencies dominate the signal and how each mode is related to the others [Kantz and Schreiber, 1997, p20].
The FT of a given signal $s(t)$ is defined as

$$\hat{s}(f) \equiv \int_{-\infty}^{+\infty} s(t)e^{-2\pi i f t}dt. \tag{2.20}$$

[5]There are several ways to perform a spectral analysis (e.g., wavelet analysis); here we only discuss the method used throughout this research work.

For a time-discrete signal s_n the above definition is equivalent to the following

$$\hat{s}_k \equiv \sum_{n=-\infty}^{+\infty} s_n e^{-2\pi i t_n},\ t_n = n\Delta t. \tag{2.21}$$

It is also possible to define the inverse FT as follows:

$$s(t) \equiv \int_{-\infty}^{+\infty} \hat{s}(f) e^{2\pi i f t} df \tag{2.22}$$

and for the discrete case

$$s_n \equiv \sum_{k=-\infty}^{+\infty} \hat{s}_k e^{2\pi i f_k},\ f_k = k\Delta f. \tag{2.23}$$

The Fourier analysis is based essentially on the fact that a continuous periodic signal $s(t) = s(t+T)$ with period T, can be decomposed as an infinite sum of sines and cosines with different frequencies; in other words, the signal $s(t)$ can be decomposed using Fourier series as follows:

$$s(t) = \sum_f a_f cos(2\pi f t) + \sum_f b_f sin(2\pi f t), \tag{2.24}$$

where a_f and b_f are the Fourier coefficients and represent the amplitudes of the different sinusoidal components of the signal.
Non-linear deterministic signals are typically non-periodic and therefore they cannot be expressed in the form of Fourier series; however, they typically have finite-energy, that is, they fulfil $\int_{-\infty}^{+\infty} |s(t)| dt < \infty$, which means that they are square integrable[6]. It is then possible to consider a sub-interval of the frequency domain $[-T/2, T/2]$, in which the square integrable signal $s(t)$ can

[6]We shall see that scaling processes have power law spectral density of the form $1/f^{\alpha}$, therefore the power density goes to infinity as $f \longrightarrow 0$; however for such processes, the corresponding observables are described by a finite range of frequencies/wave numbers (finite time or space domain), which ensures the existence of their FT.

be written as follows [Percival and Walden, 2000, p65]:

$$s(t) = \sum_{k=-\infty}^{+\infty} \left(\int_{-T/2}^{+T/2} s(t) e^{2\pi i f_k t} dt \right) e^{2\pi i f_k t} \Delta f, \tag{2.25}$$

where $\Delta f = 1/T$. Thus, for $T \longrightarrow \infty$ we have that $\Delta f \longrightarrow 0$, therefore the summation above becomes an integral and the FT and its inverse transform are defined for all t.
Also stochastic signals are typically non-periodic. In this case one employs the spectral representation theorem for continuous stationary stochastic processes, which ensures the existence of a meaningful Fourier spectrum for the correspondent stochastic signal over a sub-range of frequencies [Percival and Walden, 2000, p127].

We now define the Power Spectral Density (PSD) (energy spectral density per unit time) of the signal $s(t)$, as the square of the absolute value of its FT, that is, $S(f) = |\hat{s}(f)|^2$. It is a positive real function which gives information about the contribution to the energy from each component of the signal with frequency f. The PSD obeys the Parseval's theorem for which the FT preserves the energy of the original quantity, namely

$$\int_{-\infty}^{+\infty} |s(t)|^2 dt = \int_{-\infty}^{+\infty} |\hat{s}(f)|^2 df. \tag{2.26}$$

We have seen so far that self-similar processes exhibit statistical scale invariance over a certain range of time (or space) scales; as a consequence of this, PSDs associated with these kind of processes show power law power spectra of the form $S(f) \sim f^{-\alpha}$, where α is the spectral index.
For a statistically stationary or weakly stationary process, the PSD is intimately related to the autocorrelation function through the Wiener-Khinchin formula [Frisch, 1995, p54]

$$S(f) = \int_{-\infty}^{+\infty} C(\tau) e^{-2\pi i f \tau} d\tau, \tag{2.27}$$

where the autocorrelation function, or covariance of the signal $s(t)$, is defined

as follows

$$C(\tau) \equiv \int_{-\infty}^{+\infty} s(t)^* s(t+\tau) dt, \tag{2.28}$$

where τ is a constant stationary time increment. Hence, the PSD is the FT of the correlation function and vice versa.

For the Wiener process, for instance, the correlation function of the increments is $C(\tau) = \delta(t-s)$ (cf. Eqn. (2.14)); therefore the corresponding power spectrum will take a constant value for any frequency f. This implies that a Brownian process contains cyclic components of various frequencies with the same amplitude, in other words, it exhibits a flat spectrum, which is commonly associated with uncorrelated white noise [Kitagawa, 2010, p33].

On the contrary, for the Ornstein-Uhlenbeck process we obtained a correlation function which depends exponentially on τ (see Eqn. (2.18)), which is responsible of the correlation in the coloured noise leading to the power law power spectrum of the form $S(f) \sim f^{-\alpha}$, where α can assume a wide range of values. As we can see, power law PSDs are not unique to turbulence, therefore a Kolmogorov spectrum does not uniquely quantify the turbulent cascade.

The term "coloured noise" comes from the fact that it can be seen as the effect of filtering of white light, in this case white noise. Indeed, a way to generate coloured noise is to apply a linear time invariant filter $G(t)$ [7] to the uncorrelated white noise $\xi(t)$, in other words $\bar{\xi}(t) = G(t) * \xi(t)$, where $*$ denotes the convolution operation. Then, by FT $\bar{\xi}(t)$ we obtain $\hat{G}(f)\hat{\xi}(f)$ which can be shown to lead to a power law PSD [Kantz and Schreiber, 1997, p237]. Hence, the filter introduces long-range correlation to the white noise $\xi(t)$ generating a correlated coloured noise.

A direct consequence of Equation (2.27), for statistically stationary processes, is that the spectral index and the scaling exponent of the second order moment satisfy the following expression:

$$\alpha = \zeta(2) + 1. \tag{2.29}$$

For (fractal) monoscaling processes $\zeta(2) = 2H$, therefore a correlated coloured

[7] For further details on linear time invariant filters the reader is referred to Percival and Walden [2000],p155.

Brownian motion for which $H = 1/2$ will have a scaling PSD of the form f^{-2}. Although the uncorrelated Brownian motion is characterized by stationary time increments, however it is not a stationary processes (pure diffusive process); hence Equation (2.29) does not apply for white noise, which we have seen above is characterized by a flat spectrum.

The Fourier analysis can be easily extended to the wave vector domain, also known as k-space. Indeed, a square integrable function of the space variable $x \in \Re$, $s(x)$, can be expressed via the generalized Fourier series as a wavepacket, that is, the superimposition of (ideally) infinite waves, each of which characterized by a wave-number k. Then, the FT of $s(x)$, that is, $\hat{s}(k)$, can be defined analogously as in Equation (2.20) as well as its power spectral density $S(k) = |\hat{s}(k)|^2$, for which all the properties seen above will apply.

In the next chapters we shall see the application of the Fourier analysis in the k-space in order to test for scaling in the PSD associated with the spatial fluctuations of both intensity measurements from images of a solar quiescent prominence (Chapter 3) and magnetic field data from simulations of magnetic reconnection (Chapter 4).

2.4 Probability density function of self-similar processes

Statistical processes have defined probability distributions, which characterize the process itself. When analysing a time or space series, measurements of a phenomenon with uncertainty are usually considered to be the realization of a random variable with a certain probability distribution. Thus, the analysis of the PDF represents one of the first steps for signal modelling based on data.
In this section we focus mainly on the scaling properties of the PDF associated with self-similar processes rather than on its functional form.

Let us consider a statistically stationary random variable $x(t)$ with increments $y(\tau)$ defined as

$$y(\tau) \equiv x(t+\tau) - x(t). \tag{2.30}$$

Then, for a self-affine process the increments $y(\tau)$ hold the following statistical scaling

$$y(b\tau) \stackrel{law}{=} f(b)y(\tau), \tag{2.31}$$

where $f(b)$ is an unknown scaling function of the scale dilatation factor b.
If we now consider the following scaling transformations

$$\tau' = b\tau \ , \quad y' = f(b)y, \tag{2.32}$$

then, for the conservation of probability under change of variables, the PDF of the increments y, $P(y,\tau)$, and the PDF of the rescaled increments y', $P(y',\tau')$, will be related by the following

$$P(y,\tau) \ = \ f(b)P'(y',\tau'). \tag{2.33}$$

This is a direct consequence of self-similarity, which implies that a given process on scale τ' (and thus y') maps onto another process on a different scale τ (and y) via the above scaling transformations.
Moreover, since b is arbitrary, by choosing $b = \tau^{-1}$, Equation (2.33) reduces to the following scaling

$$\begin{aligned} P(y,\tau) &= f(\tau^{-1})P'(f(\tau^{-1})y,1) \\ &= f(\tau^{-1})\mathcal{P}_s(f(\tau^{-1})y), \end{aligned} \tag{2.34}$$

which shows that any PDF P of increments y at the time scale τ may be collapsed onto a single unique PDF $\mathcal{P}_s$ of rescaled increments $f(\tau^{-1})y$ and increment $\tau = 1$ [Kiyani et al., 2006]. The identification of the scaling function $f(b)$ is then crucial because it uniquely identifies a scaling process.
Fractal processes, for instance, are monoscaling with $f(b) = b^H$, where H is the Hurst exponent, leading to the following scaling for the PDF

$$P(y,\tau) = \tau^{-H}\mathcal{P}_s(\tau^{-H}y). \tag{2.35}$$

However, in general $f(b)$ is a non linear function of b describing then a wider class of self-affine processes.
In the next section we shall see how to determine the form of the scaling

function $f(b)$ via the calculation of the moments of the structure function.

2.4.1 Normal probability plot

In Section 2.2.1 we have seen few stochastic Gaussian processes that show self-similar properties and scaling; however not all the scaling processes are described by Gaussian statistics. Turbulence, for instance, is a non-Gaussian scaling process (see §1.3). One method for testing the Gaussian distribution of a given time (or space) series consists in plotting the experimental cumulative distribution function (CDF) of the signal against the corresponding empirical normal CDF (Gaussian CDF with same mean value and standard deviation as that of the data).
Whether the applied distribution matches the theoretical distribution within uncertainties, then the normal probability plot will show a straight line, otherwise it will introduce curvature.

Although this technique does not provide any information about the functional form of the experimental CDF in case the plot shows curvature, however it represents a powerful tool for discriminating different scaling processes. It is indeed particularly useful for our purposes since it will provide a valid test for non-Gaussianity of the presumably turbulent fluctuations analysed. We shall see the application of this method later in Chapter 3.

2.5 Generalized structure function

Scaling processes are described by a broad variety of PDFs, however it is not always possible to access their functional form. Nevertheless, what one can do is to rather calculate the parameters that determine the essential characteristic of a PDF. The calculation of the moments of the PDF then provides a valid method for the estimation of such parameters. For example, for the increments $y(\tau)$ defined in Equation (2.30), the pth moment is defined as

$$< y(\tau)^p >= \int_{-\infty}^{+\infty} y(\tau)^p P(y,\tau) dy, \tag{2.36}$$

where the angular brackets indicate an ensemble average over t and the power p determines the order of a moment. In order the moments to exist, $P(y,\tau)$ must

decay faster that $1/|y(\tau)|^{p+1}$ for $y \longrightarrow \pm\infty$ [Sornette, 2000, p9]; however, this condition is always satisfied when dealing with finite range variables (realistic cases).

The moment of first order $< y(\tau) >$ provides the mean value of $y(\tau)$, the second order moment $< y(\tau)^2 >$, the variance σ^2, the standardized third and fourth order moments define respectively the skewness $S_k =< y(\tau)^3 > /\sigma^3$ and the kurtosis $K =< y(\tau)^4 > /\sigma^4$ of the PDF (cf. Eqn. 1.20), and so on. S_k gives information about the asymmetry of a PDF, whilst K indicates the degree of peakedness in a distribution. For a Gaussian distribution, for instance, one has: $< y(\tau) >= \mu$, $< y(\tau)^2 >= \sigma^2$, $S_k = 0$ and $K = 3$.

Although the moments provide useful information about the statistical properties of a distribution, however for symmetric PDFs the odd order moments vanish. Hence, one typically obviates by defining the the generalized structure function (GSF) of order p as:

$$S_p(\tau) =< |y(\tau)|^p >= \int_{-\infty}^{+\infty} |y(\tau)|^p P(y,\tau) dy. \tag{2.37}$$

Notice however that the modulus operation may cause loss of information. In MHD turbulence, for instance, the signed moments carry additional information about the direction of the cascade [Frisch, 1995].

The GSF is a powerful tool for the quantification of self-similar scaling since, in principle, it allows to determine the form of the scaling function $f(b)$ (see Eqn. (2.31)).

Let us consider again the scaling laws obtained for the PDF of y, $P(y,\tau)$, and the PDF of the rescaled increments y', $P(y',\tau')$. Then, substituting $P(y,\tau)$ in Equation (2.37) with the expression in Equation (2.34), we obtain

$$\begin{aligned} S_p(\tau) &= \int_{-\infty}^{\infty} |y|^p \, f(\tau^{-1}) \mathcal{P}_s(f(\tau^{-1})y) \, dy \\ &= \left(f(\tau^{-1})\right)^{-p} \int_{-\infty}^{\infty} |y'|^p \, \mathcal{P}_s(y') \, dy' \\ &= \left(f(\tau^{-1})\right)^{-p} \mathcal{S}_p(1), \end{aligned} \tag{2.38}$$

where $\mathcal{S}_p(1)$ corresponds to the GSF of the rescaled increments y' and rescaled PDF $\mathcal{P}_s(y')$. This is again evidence of the self-affine property of the increments

y, which leads to the following scaling for the GSF [Kiyani et al., 2006]

$$S_p(\tau) = \tau^{\zeta(p)} \mathcal{S}_p(1) \tag{2.39}$$

where $\zeta(p)$ is the scaling exponent.
Importantly, if a single set of exponents $\zeta(p)$ applies to both positive and negative increments $y(\tau)$, then the scaling property $S_p \sim \tau^{\zeta(p)}$ is preserved under the modulus operation (see Eqn. (2.36)).
For monoscaling processes - i.e. fractal processes - $\zeta(p)$ depends linearly on p, namely $\zeta(p) = pH$, while a non-linear function of $\zeta(p)$ with p denotes multiscaling - i.e. multifractality.

In principle, the procedure for extracting the scaling exponents $\zeta(p)$ consists in plotting $log(S_p)$ against $log(\tau)$ for the different orders p of the GSF; the gradients of such plots would then yield the corresponding scaling exponents $\zeta(p)$. However, in practice, Equation (2.39) is no longer satisfied when dealing with finite size dataset, instead an extended self-similarity is observed, which will be discussed in the next section.

Moreover, finite experimental datasets generally have a small number of large events which have poor representation statistically. This may hide the scaling properties of the time (or space) series under analysis [Kiyani et al., 2009]. There exist several methods for excluding these extreme events by fixing upper limit in the calculation of the structure function [Horbury and Balogh, 1997; Veltri, 1999; Chapman et al., 2005] or directly by conditioning the data [Kiyani et al., 2006; Hnat et al., 2007; Kiyani et al., 2007].

2.5.1 Extended self-similarity

In Chapter 1 we saw that turbulence processes show a weaker form of statistical self-similarity known as generalized similarity or ESS. It was first shown to hold for the structure functions by Benzi et al. [1993] as follows

$$S_p(\tau) = [S_q(\tau)]^{\zeta(p)/\zeta(q)} . \tag{2.40}$$

Although Equation (2.40) has been observed in several turbulent systems such as the fast solar wind [Carbone et al., 1996; Kiyani et al., 2007; Nicol et al.,

2008; Chapman and Nicol, 2009], laboratory simulations of MHD turbulence [Dudson et al., 2005; Dendy and Chapman, 2006] and in HD [Grossmann et al., 1994; Bershadskii, 2007], however it has yet to find a theoretical basis[8].
ESS implies a generalized similarity of the form

$$S_p(\tau) \sim [G(\tau)]^{\zeta(p)}\,, \tag{2.41}$$

where the function $G(\tau)$ is the generalized function anticipated for scaling processes with finite cut-offs of the fields or parameters [e.g., Dubrulle, 2000; Sornette, 2000].
One way to investigate the functional form of the scaling exponent $\zeta(p)$ consists in plotting $log(S_p)$ against $log(S_q)$. Then, the linear fit to the curve within the inertial range will provide the scaling exponent ratio $\zeta(p)/\zeta(q)$. Now, for fractal scaling, $\zeta(p) = pH$, while for multifractal scaling $\zeta(p)$ is a non-linear function of p, $\zeta(p) = a + b\,p + c\,p^2 + ...$. As a consequence of this, the corresponding exponent ratio will be:

$$\frac{\zeta(p)}{\zeta(q)} = \begin{cases} \frac{pH}{qH} = \frac{p}{q} \;\longrightarrow\; Fractal \\ \\ \frac{a+b\,p+c\,p^2+...}{a+b\,q+c\,q^2+...} \neq \frac{p}{q} \;\longrightarrow\; Multifractal \end{cases}$$

Then, by using ESS to calculate the scaling exponent ratio $\zeta(p)/\zeta(q)$, one can test for fractal versus multifractal scaling distinguishing therefore different classes of self-similar processes.

In the next two chapters we shall see the application of this method in order to test for intermittency, that is, multifractal scaling, in turbulent fluctuations associated with systems of finite size.

[8]For further reading on ESS the reader is referred to Dubrulle [2000] and the related idea of finite size scaling in Sornette [2000].

Chapter 3

Hinode/SOT observations of a solar quiescent prominence

3.1 Introduction

Many filamentary upward flows in vertically striated quiescent prominences (QP) have been observed to dominate intermittently the QP plasma flow showing high variable dynamics [Berger et al., 2010].
These upflows are observed to rise within the QP with a nearly constant speed of $\sim$ 20 km s^{-1} leading to rotational motions [Berger et al., 2008]. Moreover, the Reynolds number estimated for these upflows is of the order of $\sim 10^5$ [Berger, 2009], suggesting a turbulent nature of the QP flow.

In this chapter we present the analysis of one of these presumably turbulent QPs. The aim here is to test whether the statistical properties of the QP flow are consistent with those expected for a turbulent flow in a system of finite size.
We focus on images of a specific QP observed by Berger et al. [2008] on the north-west solar limb (52N 90W) on November, 30th 2006. The images are provided by the Solar Optical Telescope (SOT) on board the Hinode spacecraft. This QP is chosen for analysis as it clearly shows several small scale upflows and vortices suggestive of turbulence (the reader is encouraged to see the time evolution of this QP in animation 1 of Berger et al. [2008]).

Generally, solar data mainly consist of images whose intensity values are directly related to the density of the plasma structure observed. This is possible thanks to the study of emission line spectroscopy (see p57–58 of Aschwanden [2004] for further details). Then, a common assumption in solar corona physics, which is also the assumption that we make here, is that the intensity measurements provided by the observations (images) are proportional to the square of plasma density.

In this chapter we shall show the application of some of the statistical techniques reported in Chapter 2 to the spatio-temporal intensity fluctuations of the imaged QP of interest in order to investigate their statistical properties and scaling.
We begin by introducing the Hinode mission along with the datasets used for our analysis; then we perform statistical analyses of the intensity measurements first in the temporal domain, and successively in the spatial domain. We conclude the chapter with a summary of the results found along with a discussion on their physical meaning. The role played by the statistical techniques used for the quantification of turbulent fluctuations is also emphasized.

3.2 The Hinode mission and the dataset

Hinode, also known as Solar-B, is a solar satellite mission developed by the Japanese Aerospace Exploration Agency (JAXA). The spacecraft name indeed comes from Japanese and means "Sunrise". Hinode was launched in September 2006 and has a sun-synchronous orbit over the day/night terminator, allowing continuous observations of the Sun. It consists of three instruments: SOT, the Extreme ultraviolet Imaging Spectrometer (EIS), and the X-Ray Telescope (XRT). SOT is a diffraction-limited Gregorian telescope with a 0.5 m aperture. It provides images of the Sun with an unprecedented resolution up to 0.2 arcsec and sample time between 15 and 30 sec. The typical image size provided by SOT is of 2048×1024 pixels with a spatial resolution of 0.10896 arcsec per pixel, where each pixel corresponds to $\Delta r \sim 77.22$ km on the solar surface. The Broadband Filter Imager (BFI), one of the four instruments of the Focal Plane Package on SOT, provides observations in two spectral lines: the 656.3 nm Hα line and the 396.8 nm Ca II H-line.

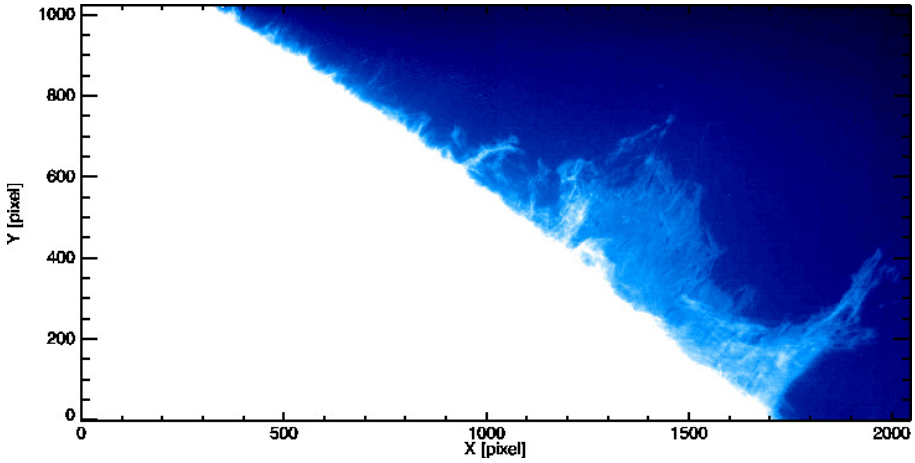

Figure 3.1: Image of a quadrant of the Sun taken in the Ca II H-line by SOT on November, 30th 2006 and showing the QP that we will focus on. Image resolution: 1 pixel $\sim$ 77.22 km on the solar surface.

We analyse images in the Ca II H-line taken with a cadence $\Delta t = 16.8$ sec on average. Figure 3.1 shows an image in the Ca II H-line of a quadrant of the Sun provided by SOT and showing the QP that we will focus on. This QP was observed for almost 6 hrs on November, 30th 2006 and its position was nearly perpendicular to the line of sight of SOT. We consider about 1000 images of size 800 $\times$ 420 pixels which span a time interval of about 4.5 hrs, from 01:00:00 UT to 05:30:00 UT. All the images have been rotated, calibrated (normalized to the exposure time), and aligned with respect to the solar limb.

Figure 3.2 shows the first frame of the dataset. Note the different structures: large scale structures appear brighter at the edge of the prominence while at smaller scales, bright and dark plumes alternate within the plasma sheet.

We will analyse fluctuations in space by taking differences in intensity along the longitudinal and transverse directions with respect to the direction of up/down flows which correspond respectively to the vertical and horizontal direction in the imaged QP shown in Figure 3.2. This procedure is shown by the overlaid grid which is made of 10 strips labelled as strips L1 to L5 along the longitudinal direction and strips T1 to T5 along the transverse direction; each strip is 10 pixels wide. We will also examine fluctuations in time, that is, from one image to the next. Five white squares, labelled A to E, with size 21×21 pixels,

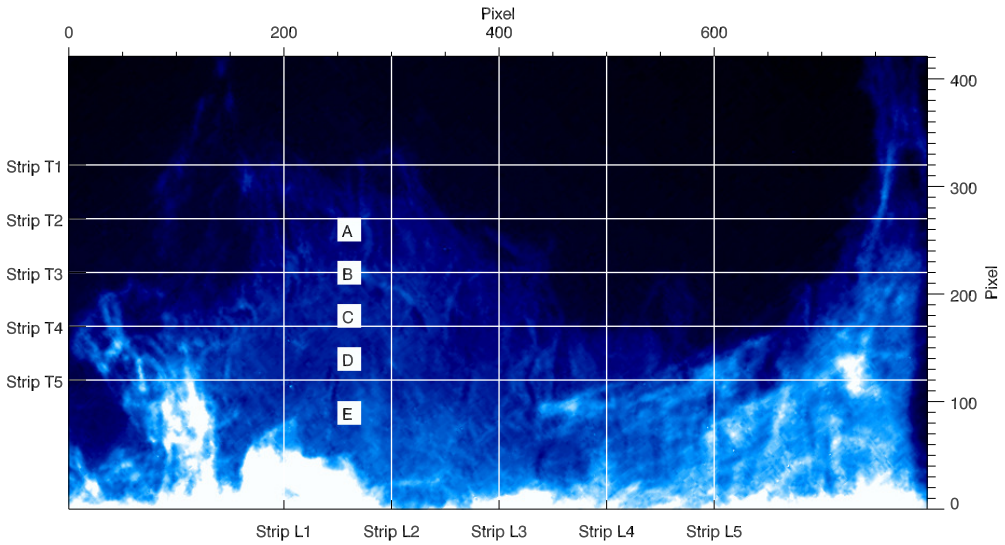

Figure 3.2: Zoom of the QP shown in Figure 3.1. The image has been rotated to the horizontal position with respect to the solar limb. Intensity levels increase from blue to white. The white grid and 5 squares are shown as reference for the analysis in the space domain (transverse strips T1 to T5 and longitudinal strips L1 to L5) and in the time domain (squares A, B, C, D and E).

indicate the regions over which the respective intensity time series are formed across all the images.

In order to improve statistics we will construct local spatial averages and will present the variation about these averages [Dudok de Wit, 2004]. The procedure used to analyse the intensity measurements in the strips consists in calculating statistical quantities for small ensembles of 10 neighbouring rows (columns) for each strip along the horizontal (vertical) direction and then performing an average across the strip width. For example, the mean value of the intensities for strip T1 will be the average over the mean values calculated for each of the 10 rows within T1. The same procedure is adopted for the analysis in the time domain: the statistical quantities calculated for each time series associated with the pixels that compose the square are averaged over the 21×21 pixels.

3.3 Analysis of the intensity fluctuations in the time domain

In this section we present the analysis of the time series associated with the intensity measurements $I(t)$ of squares A, B, C, D and E shown in Figure 3.2. Under the assumption of stationarity in a statistical sense, we define the temporal intensity fluctuations at scale τ as $\delta I(\tau) = I(t+\tau) - I(t)$. We then apply statistical methods such as PSD and PDF in order to test whether these fluctuations are correlated.

3.3.1 Spectral analysis

Figure 3.3 shows the averaged power spectrum, $< PSD >$, of the intensity time series associated with squares A to E. Recall that we compute the PSD of a square by taking the average of the PSDs calculated for each of the 21×21 pixels that form a square.
As we can see, all the PSDs show a power law scaling with a spectral index α.

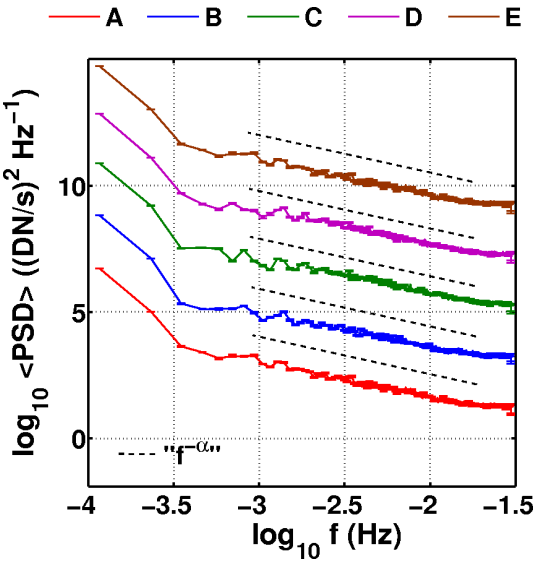

Figure 3.3: Log-log plot of the PSDs of the intensity time series associated with squares A, B, C, D, and E. All the power spectra are shifted in the y-direction for clarity. The power spectra show scaling of the form $f^{-\alpha}$ whose spectral indices α are given in Table 3.1.

We extract the α values by reading the gradient of the linear fits to the plots in Figure 3.3 within the frequency range 1–20 mHz. Table 3.1 reports the spectral indices for all the squares under analysis. The α values are all approximately close to 1, implying a scaling for the PSD of the form $\sim 1/f$.

Data	**ff $\pm$ Δff**
A	1.21 $\pm$ 0.04
B	1.17 $\pm$ 0.04
C	1.29 $\pm$ 0.04
D	1.27 $\pm$ 0.04
E	1.20 $\pm$ 0.04

Table 3.1: Spectral index α of the PSDs of squares A to E. The α values are estimated by extracting the gradient of the linear fits to the plots in Figure 3.3 in the frequency range 1–20 mHz.

We attribute this scaling to a "random telegraph" process, which is a stochastic Markov process (see § 2.2.1). The intensity time series, indeed, seem to behave as random telegraph signal in the sense that they take random values associated with uncorrelated pulses or features in the flow moving through the line of sight of the observations [Kaulakys and Meš Kauskas, 1998; Kaulakys et al., 2005].
We test this idea by estimating the "maximum observable speed" of structures moving past the line of sight as $u = \Delta r/\Delta t \sim 4.6$ km s^{-1}. Since the prominence flow has a bulk velocity ($u_{flow} \sim 25$ km s^{-1}) larger than u then, at a given pixel, intensity fluctuations are moving too fast for us to observe correlations in time. In other words, the time needed to catch a coherent structure (e.g., up-flows), at fixed space coordinates across two consecutive frames, is much shorter than the cadence, therefore, all the moving flows in the prominence appear decorrelated in time.

3.3.2 PDF analysis

Let us now focus on the PDF of the intensity fluctuations $\delta I(\tau)$. Figure 3.4 shows the PDFs of the intensity fluctuations $\delta I(\tau)$ at time scale τ=1.12 min for squares B and D, centered on the mean value μ and normalized to the

standard deviation σ, in order to allow comparisons with a Gaussian distribution (solid red line). As we can see, the temporal fluctuations appear to be normal distributed. Fluctuations $\delta I(\tau)$ at scales $\tau \neq$1.2 min, but still within the range of scaling observed for PSD, show similar behaviour.
The Gaussian distribution of the intensity fluctuations is also consistent with the value of the excess kurtosis k [1] calculated for the PDFs shown in Figure 3.4. Specifically, $k = 0.91 \pm 0.16$ for point B, and $k = 0.78 \pm 0.16$ for point D. We find consistent statistics also for the other squares chosen for the analysis.

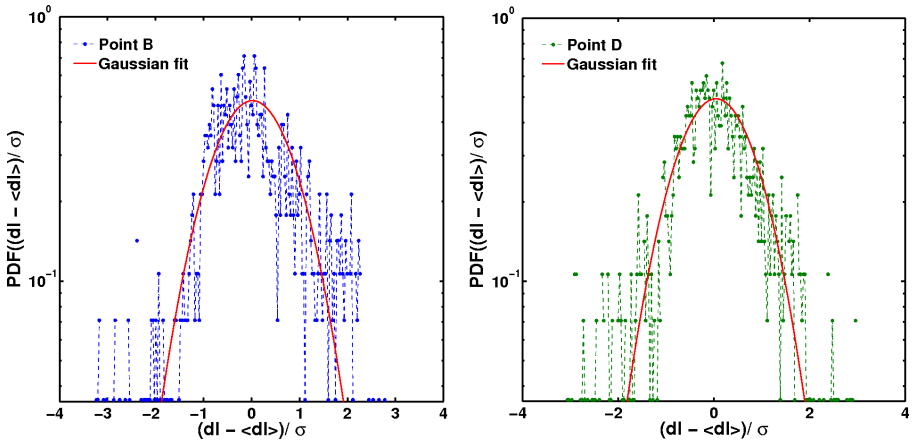

Figure 3.4: PDFs of the intensity fluctuations $\delta I(\tau)$ with τ = 1.12 min for squares B (left) and D (right). Both PDFs are centered on $< \delta I >$ and normalized to the standard deviation σ of the intensity fluctuations, in order to allow comparisons with a Gaussian PDF with $\mu = 0$ and $\sigma = 1$ (red solid lines).

Further evidence of the Gaussian statistics of the intensity fluctuations is given by the normal probability plot (see § 2.4.1). The panels in Figure 3.5 show the normal probability plot for the CDFs of the intensity fluctuations $\delta I(\tau)$ with τ=1.12 min for squares B (left) and D (right). Notice that both plots almost show a linear behaviour, again confirming that the fluctuations $\delta I(\tau)$ are nearly Gaussian.

Due to the lack of correlation of the intensity fluctuations in time, we then move straight to the analysis of the intensity measurements in space.

[1] Recall the excess kurtosis k is defined as the standard kurtosis K-3, so that for Gaussian PDFs the excess kurtosis is null.

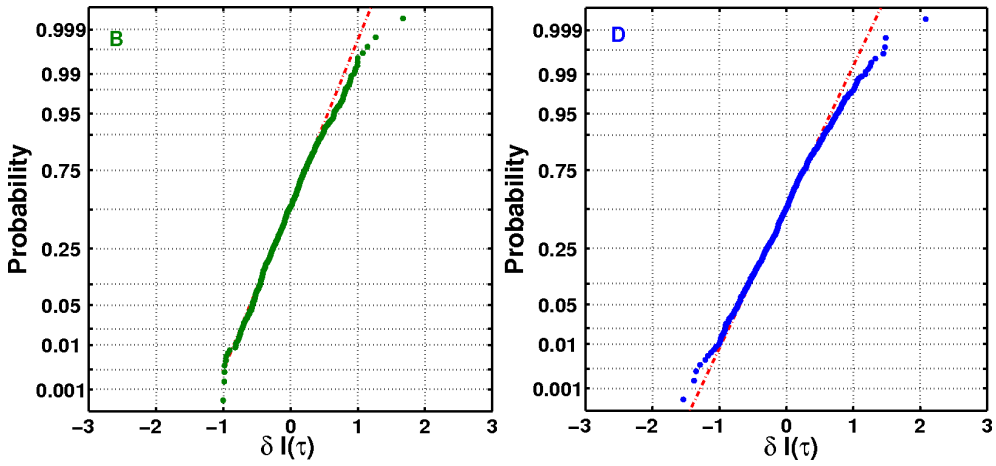

Figure 3.5: Normal probability plots of the CDFs of the intensity fluctuations $\delta I(\tau = 1.12$ min) for squares B (left) and D (right). Dashed red lines refer to the probability expected for a Gaussian distribution.

3.4 Analysis of the intensity fluctuations in the space domain

In this section we present the analysis of the intensity measurements $I(r)$ in space for a fixed time of the observation corresponding to the first frame of our dataset (frame shown in Fig. 3.2). Under the assumption of homogeneity in a statistical sense, we define the spatial increments as $\delta I(L) = I(r+L) - I(r)$. Thus, we investigate the statistical properties of the intensity fluctuations $\delta I(L)$ along the longitudinal and transverse direction to the bulk (driven) flow of the QP of interest.

3.4.1 Spectral analysis

Let us begin by performing the spectral analysis of the intensity series $I(r)$. The panels in Figure 3.6 show the averaged PSD of the intensity measurements for the longitudinal strips L1-L5 (left) and the transverse strips T1-T5 (right). Recall that we compute the PSD of a strip by taking the average of the PSDs calculated for each of the 10 rows (or columns) which each strip is composed of.

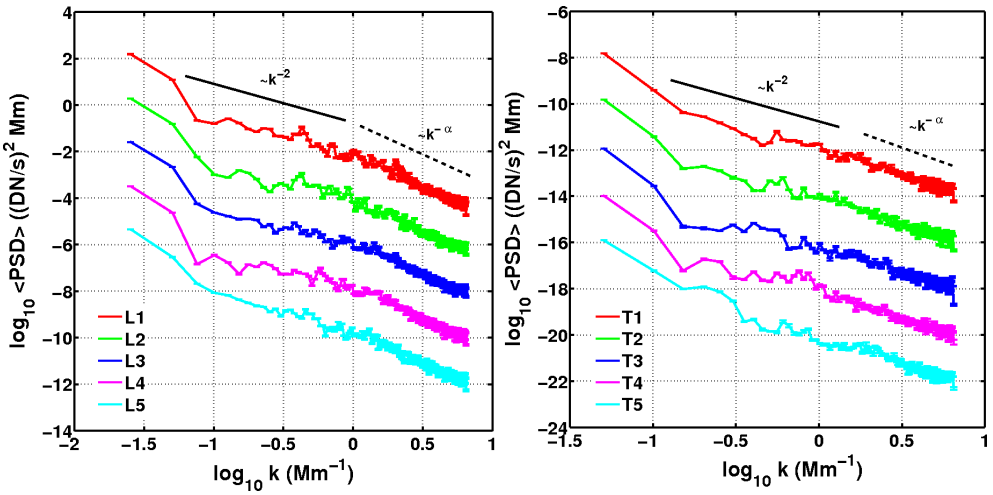

Figure 3.6: Log-log plots of the PSDs for the longitudinal strips L1-L5 (left) and the transverse strips T1-T5 (right). All the power spectra are shifted in the y-direction for clarity. The PSDs reveal two regions with different scaling exponents: k^{-2} at small wave numbers (solid line) and $k^{-\alpha}$ within the wave number range $\sim$ 1.2–6 Mm^{-1} for the longitudinal strips and $\sim$ 1.7–6 Mm^{-1} for the transverse strips (dashed line). The values of the spectral index α for all the strips under analysis are reported in Table 3.2.

We can see that all the power spectra approximately exhibit two trends: at small wave numbers the spectra scale as $\sim k^{-2}$, consistent with a Brownian process (see § 2.2.1), while at larger wave numbers the spectra scale as $\sim k^{-\alpha}$ with a spectral index α suggestive of non-trivial dynamics. The α values for all the strips are reported in Table 3.2 and are estimated by extracting the gradient of the linear fits to the plots in Figure 3.6 within the wave number range $\sim$ 1.2–6 Mm^{-1} for the longitudinal strips and $\sim$ 1.7–6 Mm^{-1} for the transverse strips.

Thus, the intensity measurements possess non-trivial power law power spectra in both the longitudinal and transverse direction to the prominence bulk flow. The ranges of wave numbers for which we observe this scaling corresponds to the range of length scales 0.17–0.89 Mm for the longitudinal fluctuations and 0.17–0.56 Mm and for the transverse fluctuations. We identify these two ranges as potential ranges of turbulence.

For the K41 theory, an ideal turbulent flow is expected to exhibit a Kolmogorov spectrum with a spectral index α=5/3 (see Eqn. (1.7)). However

Longitudinal strips	$\alpha \pm \Delta\alpha$	**Transverse strips**	$\alpha \pm \Delta\alpha$
L1	2.73 ± 0.29	T1	2.69 ± 0.21
L2	2.74 ± 0.37	T2	2.76 ± 0.20
L3	2.81 ± 0.25	T3	2.81 ± 0.19
L4	2.78 ± 0.27	T4	3.17 ± 0.15
L5	2.75 ± 0.29	T5	2.93 ± 0.19

Table 3.2: Spectral index α of the PSD of the intensity series associated with strips L1 to L5 and strips T1 to T5. The α values are estimated by extracting the gradient of the linear fits to the plots in Figure 3.6 in the k-number range $\sim$ 1.2–6 Mm^{-1} for the longitudinal strips and $\sim$ 1.7–6 Mm^{-1} for the transverse strips.

we find spectral indices distinct from this value. This is due to the fact that we are dealing with integrated, line of sight intensity measurements. Nevertheless, we should still expect line of sight measurements to capture qualitative features of turbulence whilst not necessary giving the same numerical values of scaling exponents as in-situ point observations.

3.4.2 Tests for non-Gaussianity

We now investigate the probability distribution of the intensity fluctuations $\delta I(L)$ with length scales L within the potential range of turbulence. As we saw in Section (§ 1.3), turbulent fluctuations at the inertial scales are characterized by non-Gaussian PDFs. Figure 3.7 shows the PDFs of $\delta I(L)$ with $L \sim 0.5$ Mm for a representative strip along each direction considered, that is, strips L1 and T5 along the longitudinal and transverse direction respectively. We choose $L \sim 0.5$ Mm since it is a potential inertial scale common to both longitudinal and transverse strips; however we obtain the same statistics at all the length scales L within the potential range of turbulence. Notice also that the PDFs have been centered on $\mu =< \delta I(L) >$ and normalized to the standard deviation σ, in order to allow comparisons with a Gaussian distribution (solid red line). As we can see, the PDF of the intensity fluctuations along both directions considered departs from a Gaussian distribution.

Moreover the excess kurtosis k of the PDFs shown in Figure 3.7 is 4.12 ± 0.24 and 2.44 ± 0.17 for strips L1 and T5 respectively, suggesting therefore

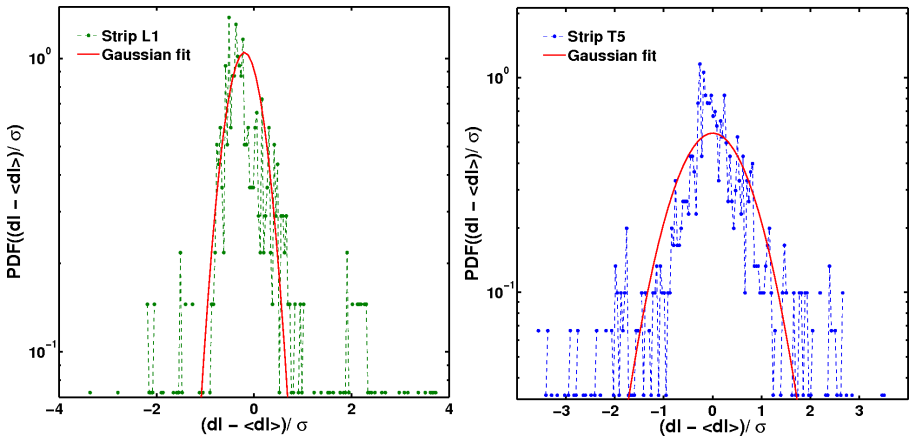

Figure 3.7: PDFs of the intensity fluctuations $\delta I(L)$ with $L \sim 0.5$ Mm for strips L1 (left) and T5 (right). Both PDFs are centered on $< \delta I(L) >$ and normalized to the variance σ. Red solid lines are Gaussian PDFs with $\mu = 0$ and $\sigma = 1$.

non-Gaussian statistics. We find similar values of the excess kurtosis also for the other strips under analysis as a signature of the non-Gaussian nature of the intensity fluctuations.

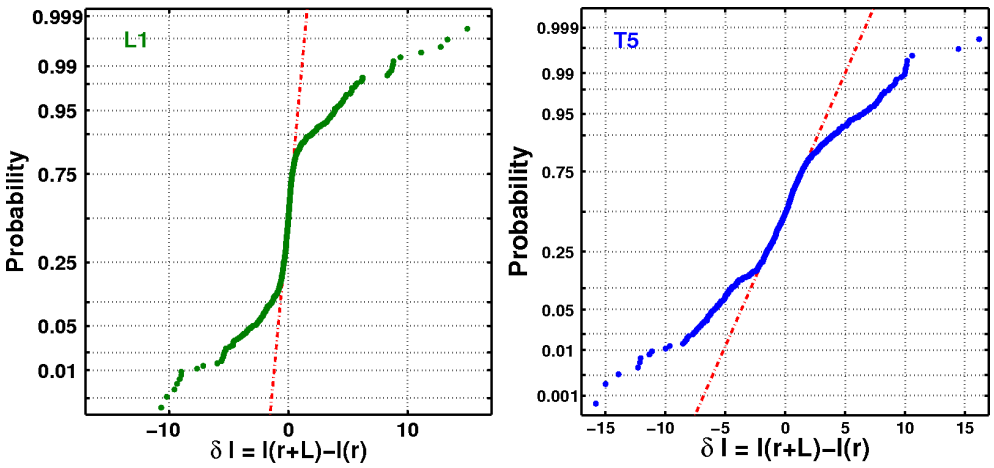

Figure 3.8: Normal probability plots of the CDFs of $\delta I(L)$ with $L \sim 0.5$ Mm for strips L1 (left) and T5 (right). Dashed red lines refer to the probability expected for a Gaussian distribution.

Further evidence of non-Gaussian statistics is given by the normal probability plot of the CDF of the intensity fluctuations $\delta I(L)$ (see § 2.4.1). The

panels in Figure 3.8 show the normal probability plot of the observed CDF of the intensity fluctuations $\delta I(L)$ with $L \sim 0.5$ Mm for strips L1 and T5. Both normal probability plots show curvature, providing therefore evidence of the non-Gaussianity of the intensity fluctuations along both the longitudinal and transverse direction.

A distinctive characteristic of turbulence is that the PDFs of non-Gaussian fluctuations at different scales are related by a multifractal similarity or scaling of the moments of the structure function. We then test for this by examining the GSF of the spatial intensity fluctuations.

3.4.3 Quantifying the structure function scaling

In the first part of Chapter 1 we saw that turbulence is characterized by an intermittent energy cascade; as a consequence of this, the scaling exponent of the GSFs, $\zeta(p)$, is a non linear function of p. Determining the precise $\zeta(p)$ is central to testing turbulence theories. However, here we do not have in-situ measurements, therefore we cannot directly compare our observed $\zeta(p)$ value with predictions of turbulence theories. Nevertheless, we can still test whether the $\zeta(p)$ that we observe are non-linear with p, consistent with a multifractal, intermittent flow.

Let us then focus on the GSF of the intensity fluctuations $\delta I(L)$ (see § 2.5 for details on the GSF). We label as L_{long} and L_{trans} the space increments in pixel of the intensity fluctuations $\delta I(L)$ respectively along the longitudinal and transverse direction to the bulk flow of the QP.

The left panels of Figures 3.9 and 3.10 show log-log plots of the averaged third moment of the GSF, $< S_3 >$, versus L_{long} for strips L1 to L5, and versus L_{trans} for strips T1 to T5 respectively. As we can see, all the GSFs increase with L indicating a high degree of correlation of the intensity fluctuations along both the longitudinal and transverse direction to the bulk flow. This is a signature of the presence of coherent structures in the QP.
Notice also that the GSFs exhibit a knee at a length scale $L \sim 0.89$ Mm for the longitudinal strips and at $L \sim 0.56$ Mm for the transverse strips. The knees delimit the crossover between the small-scale turbulence and the large-scale coherent structures. We associate the spatial scales at which the GSFs show

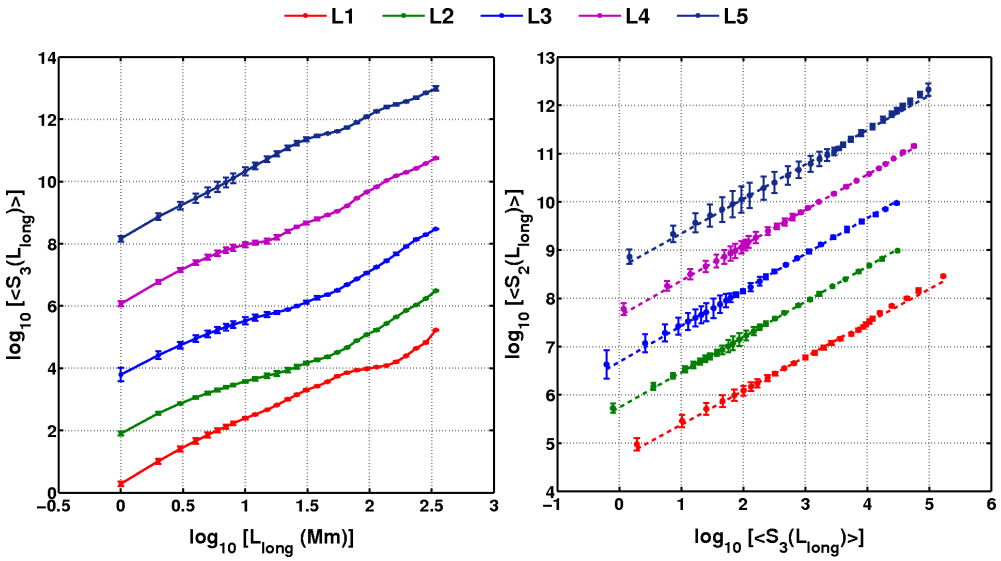

Figure 3.9: *Left panel*: log-log plot of $< S_3 >$ versus L_{long} for the intensity fluctuations associated with strips L1-L5 along the longitudinal direction to the the prominence bulk flow. *Right panel:* log-log plot of $< S_2 >$ against $< S_3 >$ for all the longitudinal strips considered showing evidence of ESS. All the curves shown in both panels are shifted along the y-direction for clarity.

these "break points" in the longitudinal and transverse fluctuations to the characteristic height and width of the small scale up/down flows respectively. Importantly, the intensity fluctuations in the longitudinal direction reveal a correlation over a broader range of spatial scales compared to the fluctuations along the transverse direction; this is because the coherent structures detected (the up/down flows) move along the vertical direction to the prominence bulk flow, that is, the longitudinal direction, in which we then expect to see the strongest correlation in a turbulent flow [Frisch, 1995].

The GSFs shown in the left panels of Figures 3.9 and 3.10 clearly do not follow the power-law scaling expected for fully developed turbulence in an infinite medium (cf. Eqn. (1.26)). This is mainly due to the fact that we are dealing with a system of finite size, therefore we do not have direct access to the scaling exponent $\zeta(p)$. Hence, we employ ESS in order to calculate the ratio of two scaling exponents instead (see § 2.5.1 for more details on ESS). We consider the averaged second and third order of the structure function, then we plot $\log(< S_2 >)$ against $\log(< S_3 >)$ for all the strips considered.

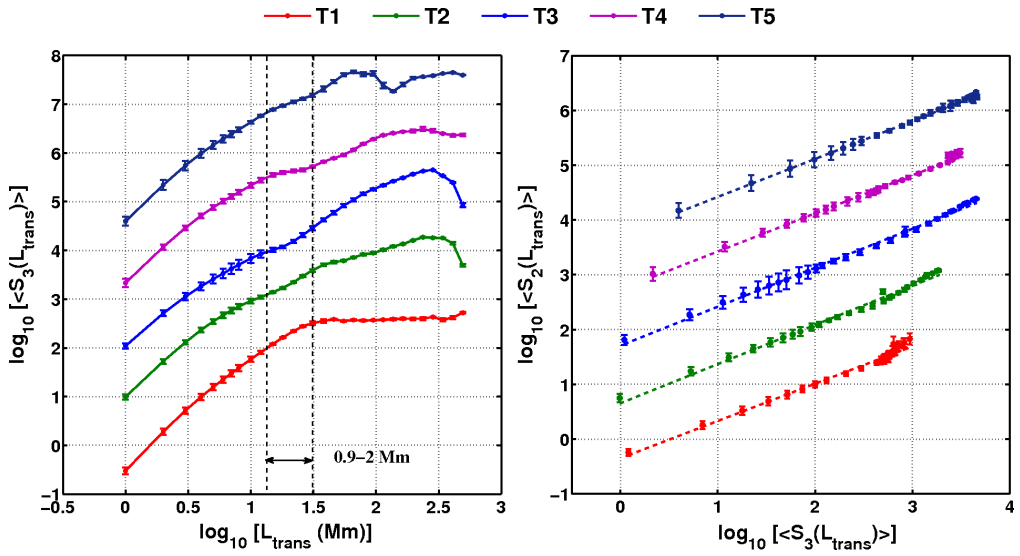

Figure 3.10: *Left panel*: log-log plot of $< S_3 >$ versus L_{trans} for the intensity fluctuations associated with strips T1-T5 along the transverse direction to the prominence bulk flow. *Right panel:* log-log plot of $< S_2 >$ against $< S_3 >$ for all the transverse strips considered showing evidence of ESS. All the curves shown in both panels are shifted along the y-direction for clarity.

The right panels in Figures 3.9 and 3.10 show evidence of ESS for both the longitudinal strips (L1-L5) and the transverse strips (T1-T5). Specifically, the log-log plots show straight lines within the ranges of length scales 0.17–0.89 Mm for the fluctuations along the longitudinal direction and 0.17–0.56 Mm for the fluctuations along the transverse direction. Departures of the curves from a linear behaviour occur for length scales outside these ranges and are associated with large-scale coherent structures in the flow.

The gradient of such plots in the inertial range provides a measurement of the ratio $\zeta(2)/\zeta(3)$. Figure 3.11 show $\zeta(2)/\zeta(3)$ for strips L1 to L5 in the longitudinal direction (left) and for strips T1 to T5 along the transverse direction (right). The error bars provide an estimate of the uncertainty in the gradients of the fitted lines in the correspondent turbulence range. The ratio $\zeta(2)/\zeta(3)$ appears to be roughly constant across all the strips and, more interestingly, differs from the value that one would expect if $\zeta(p)$ was linear in p, that is, $\zeta(2)/\zeta(3) = 2H/3H \sim 0.66$ (see §2.5.1). The ratios of the scaling exponents found for all the strips are therefore consistent with a non-linear form of the

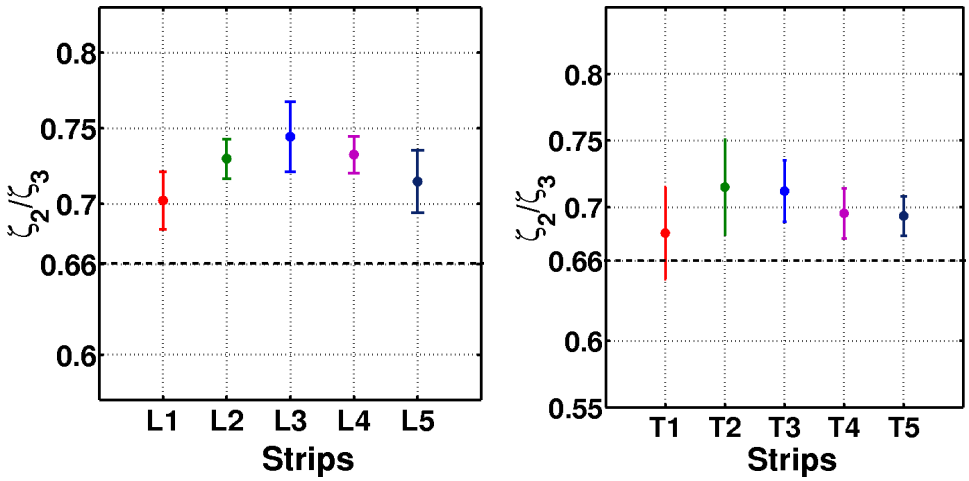

Figure 3.11: Ratios of the scaling exponents $\zeta(2)/\zeta(3)$ for the longitudinal (left) and transverse (right) strips chosen for the analysis. The values of the scaling exponent ratio correspond to the gradients of the linear fits in the turbulence ranges to the curves shown in the left panels of Figures 3.9 and 3.10 for the strips L1-L5 and T1-T5 respectively. Notice that both plots show nearly constant ratios, whose values differ from 0.66, consistently with a multifractal field.

scaling exponent $\zeta(p)$. This is a signature of the multifractal nature of the spatial intensity fluctuations, which suggests an intermittent turbulence process in action within the prominence flow.

3.4.4 Evidence of the generalized scaling

In the previous section we saw that the GSFs of the intensity fluctuations at the inertial scales do not depend linearly on L. Thus, a scaling law of the form $S_p(L) \sim G(L)^{\zeta(p)}$ is expected to hold the inertial range of turbulence (see § 1.3.3 and § 2.5.1). Here, we test whether the generalized function $G(L)$ depends on the details of the flow or not.

We consider the generalized similarity for the intensity fluctuations associated with strip T5. In Figure 3.12 we plot the averaged third moment of the structure function, $< S_3 >$, normalized to a value L_0 against L/L_0 (in logarithmic axes) for 7 consecutive time intervals separated by ΔT= 1.12 min and starting at t_0= 01:10:31 UT. The collapse of all the GSFs onto each other within the inertial range indicates the existence of a single scaling function

$G(L/L_0)$ for which the GSFs hold the following generalized scaling (cf. Eqn. (1.27))

$$S_p(L) = S_p(L_0)G(L/L_0)^{\zeta(p)}, \tag{3.1}$$

where L_0 is a characteristic parameter of the flow. We have chosen $L_0 \sim 0.54$ Mm since this is the characteristic length scale that we found for the intensity fluctuations along the transverse direction, that is, the typical width of the small-scale coherent structures (up/down flows).

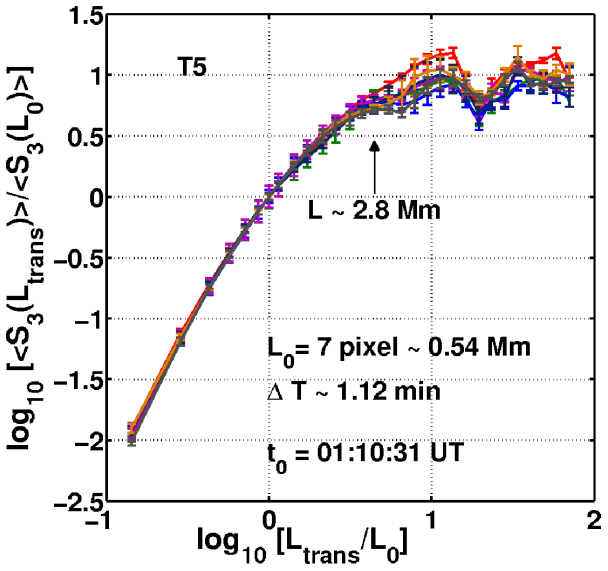

Figure 3.12: Log-log plot of $< S_3(L_{trans}) > / < S_3(L_0) >$ versus L_{trans}/L_0 with L_0= 0.54 Mm for strip T5 and for seven different frames of the dataset separated by ΔT= 1.12 min. t_0 is the time of the observation corresponding to the first frame of the dataset. The arrow indicates the length scale after which the GSF collapse breaks.

Moreover, the overlapping of the various GSFs in Figure 3.12 breaks where the effects of large-scale structures become important. As we saw in the previous section, indeed, along the transverse direction the GSFs exhibit a knee in the range of scales $\sim$ 0.9–2 Mm (dashed black lines in Fig. 3.10), which indicates the crossover between the small-scale turbulence and the large-scale coherent structures. This break point for the strip T5 occurs at a length scale $L \sim 2$ Mm. Large-scale coherent structures in the prominence flow then have typical length scales $L >$2 Mm; an example is the large bright structure shown

in Figure 3.2 on the right of the prominence and crossed by strip T5, whose width is approximately 2.8 Mm.

3.5 Conclusions

3.5.1 Results summary

In this chapter we focused on the images of a solar QP provided by SOT on board Hinode. Our interest for the specific QP here analysed arose from previous observations made by Berger et al. [2008] according to which the QP plasma flow shows highly variable dynamics involving small scale upflows and episodic vortices suggestive of turbulence. We tested this idea by performing statistical analyses of the integrated, line of sight intensity measurements associated with the QP from the prospective of a finite sized turbulent system. Thus, we quantified the statistical properties of the spatio-temporal intensity fluctuations of the QP flow. Specifically, we analysed the intensity fluctuations in space along two directions, the longitudinal direction which is the direction along which the upward/downward flows move within the prominence plasma sheet, and the direction transverse to the bulk flow; we also focused on the intensity time series corresponding to a time interval of about 4.5 hrs ($\sim$ 1000 images).

We found that the temporal intensity fluctuations possess a scaling PSD of the form $\sim 1/f$. We associated this behaviour to the random telegraph effect arising from uncorrelated pulses moving past the line of sight of the observations. Indeed, we showed that the maximum observable speed of the small-scale structures in the QP is much smaller than the speed of the up/down flows, thus preventing us to appreciate any correlation of the fluctuations in time. Consistently, we also found that the temporal fluctuations are nearly Gaussian distributed.

We observed a completely different scenario in the space domain. We found that the spatial intensity fluctuations exhibit all the hallmarks of finite range fluid-like turbulence. Specifically, they possess non-trivial power law power spectra, non-Gaussian distributions and have scaling GSFs consistent with a multifractal field. In particular, we showed that ESS holds for all

the strips chosen for the analysis and it is consistent for each direction transverse and longitudinal to the bulk flow. The ratio of the scaling exponents $\zeta(2)/\zeta(3)$, indeed, revealed to be roughly constant for all the strips along each direction and its value is distinct from 0.66, suggesting a multifractal nature of the intensity fluctuations. Importantly, we found evidence of the generalized scaling expected for finite range turbulence. Specifically, we showed that the normalized third order GSFs of the spatial fluctuations for seven different time intervals all collapse onto a single scaling function $G(L/L_0)$, where L_0 is a characteristic length scale of the flow. We identified this function as the generalized function anticipated for finite range turbulent flows.

3.5.2 Discussions

The principal aim of the analysis here presented has been to explore, for the first time, the possibility of discerning the quantitative signatures of turbulence, namely multifractal or intermittent statistical scaling, within the flows of a long-lived QP. We have shown how tests for non-Gaussianity, multifractality, scaling and ESS can be applied in order to fully identify and quantify statistical properties of turbulent fluctuations.
For these specific intensity measurements we are restricted to a qualitative characterization of the fluctuations since the observations are integrated along the line of sight rather than in-situ in the flow. Despite this constraint, the statistical methods used are powerful tools to test the hypothesis that in-situ flows are turbulent. Their application indeed revealed that the statistical properties of the intensity fluctuations associated with the QP of interest are consistent with a MHD turbulent flow in a system of finite size. This is a clear evidence of in-situ evolving small-scale turbulence within the prominence flow.

Since many QPs in the Hinode/SOT database exhibit similar dynamics, then this opens up the possibility of using these QPs as a "laboratory for turbulence", to investigate for example finite sized effects on the turbulent flow. The question that immediately arises is whether the flow in these prominences is more generally found to be turbulent. It would be intriguing to determine if or how the presence of turbulence in QPs correlates with their physical properties. Importantly, turbulence is a mechanism by which directed flow

is transformed into heat. Heating at the loop foot-points is known to drive condensations at the loop tops [e.g., Karpen et al., 2001]. Rather than heating driven by a coronal or a chromospheric reconnection process, the evidence of turbulence presented here suggests a continuous heating supply that could account for the continuous formation process of QPs.

Chapter 4

Kinetic PIC simulations of magnetic reconnection

4.1 Introduction

Fully kinetic particle-in-cell (PIC) simulations represent an informative attempt to explain magnetic reconnection since they allow both local and global dynamics to be studied spanning the macroscopic fluid scales down to the motion of electrons. However, one of the main problems when using PIC codes is the choice of boundary conditions, which could potentially affect the dynamics of the process. Particularly, in magnetic reconnection simulations, in order to model the diffusion region properly, the simulation domain must be large enough to prevent artificial effects such as recirculation of particles and magnetic flux during the time interval of interest.
Recently, fully kinetic PIC simulations of collisionless reconnection with relatively large open boundary conditions and/or large spatial domains have been performed both in 2D [Daughton et al., 2006] and 3D [Daughton et al., 2011] geometries. These simulations have shown that the initial current layer always becomes unstable due to the presence of non-linear (interacting) tearing instabilities leading to the formation of magnetic structures on multiple scales, which manifest highly variable dynamics suggestive of turbulence.

In this chapter we investigate the statistical properties of the reconnection generated fluctuations in the above simulations in order to test whether

these fluctuations are indeed turbulent, and if so, what kind of turbulence phenomenology they exhibit. Firstly, we shall focus on 2D simulations of reconnection. Here, two simulations with different initial configurations of the magnetic field will be analysed: a symmetric configuration and an asymmetric configuration. Secondly, we shall move to the analysis of the reconnection simulation in a 3D geometry. In the last section of this chapter, differences and comparisons between the results obtained from the analyses of the 2D and 3D simulations of reconnection will be summarized and discussed.

4.2 2D magnetic reconnection

Kinetic PIC simulations of magnetic reconnection in 2D provide the opportunity to develop a basic model describing reconnection processes that could be successively extended in a 3D geometry. The magnetic topology in the 2D case is much simpler than in 3D although not fully understood yet. A broad variety of regimes are achievable depending on the parameters chosen, the boundary conditions and the initial magnetic field configurations. In this section we shall focus on two kinetic PIC simulations of collisionless magnetic reconnection in a 2D geometry: one simulation is initialized with a symmetric magnetic field and the other with an asymmetric magnetic field. These two types of configurations lead to the formation of coherent structures at different scales and distributed differently in space for each case: for the symmetric case, three large magnetic islands are generated, while in the opposite configuration, small scale magnetic structures emerge asymmetrically with respect to the X point.
Both simulations discussed in this section use a PIC code which solves the full set of relativistic Vlasov and Maxwell's equations. These simulations employ an initial Harris current sheet and a uniform guide magnetic field. The temperature in the simulation is the same for electrons and ions and is uniform across the current sheet; while the mass ratio is $m_i/m_e = 100$, which implies that d_i, the ion inertial length, is 10 times d_e, the electron inertial length.

We shall focus on the statistical properties of the magnetic field fluctuations generated during the reconnection process. Importantly, we distinguish these fluctuations from the noise that arises from the so-called discrete particle

noise due to the PIC code [Birdsall and Langdon, 1985]. The latter will be analysed in detail in the next section and behaves similarly in both 2D and 3D simulations; specifically, the PIC noise shows the same characteristics as uncorrelated white noise at small scales, and as correlated (coloured) Brownian noise at large scales.

4.2.1 2D reconnection in a symmetric configuration

In this section we focus on 2D fully kinetic PIC simulations of collisionless magnetic reconnection with a symmetric initial magnetic field. This simulation is initialized with a Harris sheet with magnetic field $\mathbf{B} = B_0 tanh(z/\lambda)\mathbf{e}_x$ and density profile $n = n_0 sech^2(z/\lambda)$, where B_0 is a uniform guide field and $\lambda = d_i$ is the initial half-thickness of the initial current layer. The simulation domain size is $L_x \times L_z = 70d_i \times 35d_i$, corresponding to 2048×1024 cells, and each cell contains 280 particles per species - i.e. ions and electrons. The simulation employs open boundary conditions in the X and Z directions. Also, a weak 4% magnetic perturbation is included to set up a large-scale flow pattern consistent with the open boundaries, while still enabling linear modes to grow [Daughton et al., 2006].

We analyse the three components of the magnetic field, B_i $(i = x, y, z)$, at three different times of the simulation, corresponding to an early phase of the process at $T\Omega_{ci}$=70, where the magnetic reconnection is just starting and a middle ($T\Omega_{ci} = 140$) and late ($T\Omega_{ci} = 200$) phase, where three large magnetic islands emerge (e.g., see the time evolution of B_y in the three panels of Fig. 4.1). We probe the statistical properties of the reconnection generated fluctuations by applying some of the statistical techniques discussed in Chapter 2 to each component of the magnetic field, in order to detect any turbulent mechanism in action during the reconnection process. Thus, we take six cuts on the simulation grid within the reconnection region where the field is strongly fluctuating, and label them as cuts 1 to 6 (e.g., see cuts chosen for B_y at $T\Omega_{ci}$=70 in Fig. 4.2).

A spectral analysis reveals that all magnetic field components at all simulation times here considered show a short range power-law power spectrum (see Fig. 4.3). In particular, the PSD of B_y at $T\Omega_{ci}$=70 exhibits a power-law

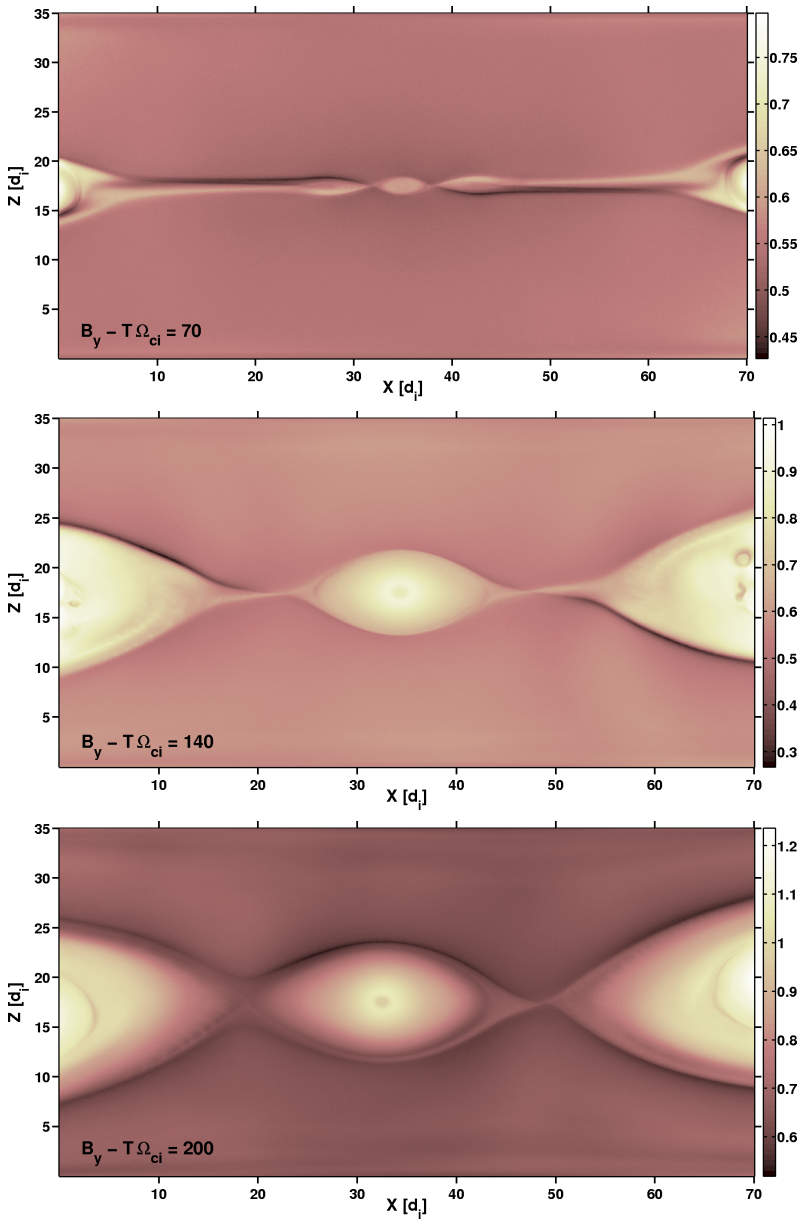

Figure 4.1: Plots of the y-component of the magnetic field, B_y, at the simulation time $T\Omega_{ci}$=70 (upper), 140 (middle) and 200 (lower). Notice the formation of three large islands at later times.

scaling in the range of k numbers $0.06{d_e}^{-1} < k < 0.17{d_e}^{-1}$ with a spectral index α ranging from 1.4 to 2.3 across all the cuts chosen for the analysis (see Fig. 4.4). Notice also that at scales $L < 6d_e$ all spectra are flat, indicating an uncorrelated white noise. The latter is attributed to the PIC noise as we shall

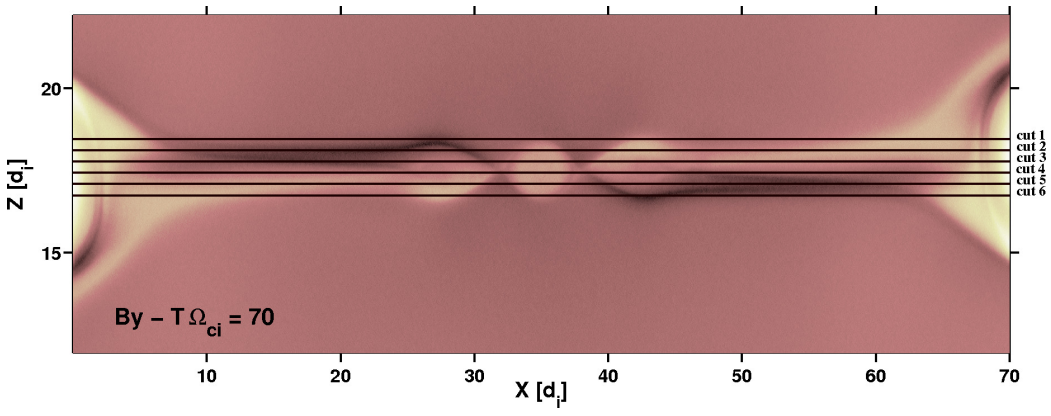

Figure 4.2: Zoom of B_y at $T\Omega_{ci}$=70 showing the six cuts within the reconnection region chosen for the analysis. Cuts are labelled as cut 1 to 6.

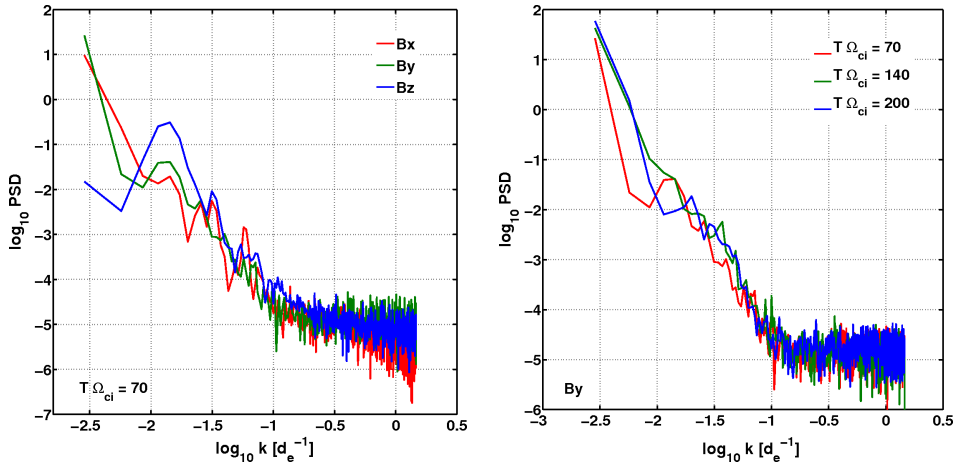

Figure 4.3: *Left panel:* log-log plot of the PSD of all components of the magnetic field at $T\Omega_{ci}$= 70 for a representative cut in the reconnection region. *Right panel:* log-log plot of the PSD of B_y at $T\Omega_{ci}$= 70, 140 and 200 for a representative cut in the reconnection region.

see in the next section.

Under the assumption of statistical homogeneity, turbulent fluctuations on length scale L are expected to follow scaling laws and non-Gaussian statistics (§ 1.2.3 and § 1.2.4). Then, we begin by analysing how the reconnection generated fluctuations are distributed. Fluctuations $\delta B_i(L) = B_i(X + L) - B_i(X)$ at later times of the simulation ($T\Omega_{ci}$=140 and 200), show poorly defined PDFs for all components of the magnetic field (e.g., see

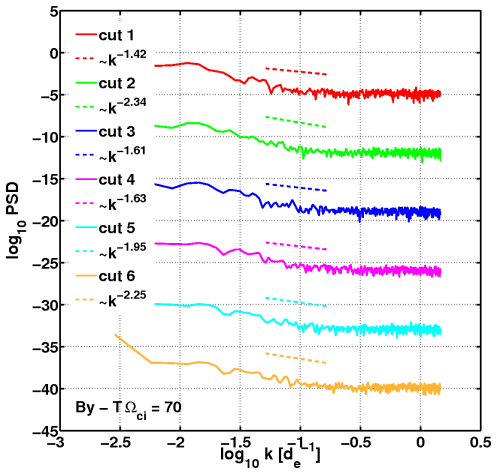

Figure 4.4: PSDs of B_y at the simulation time $T\Omega_{ci}$=70 for the six cuts chosen for the analysis. Dashed lines are linear fits to the curves in the range of k numbers $0.06{d_e}^{-1} < k < 0.17{d_e}^{-1}$. All PSDs are shifted along the y-axis for clarity.

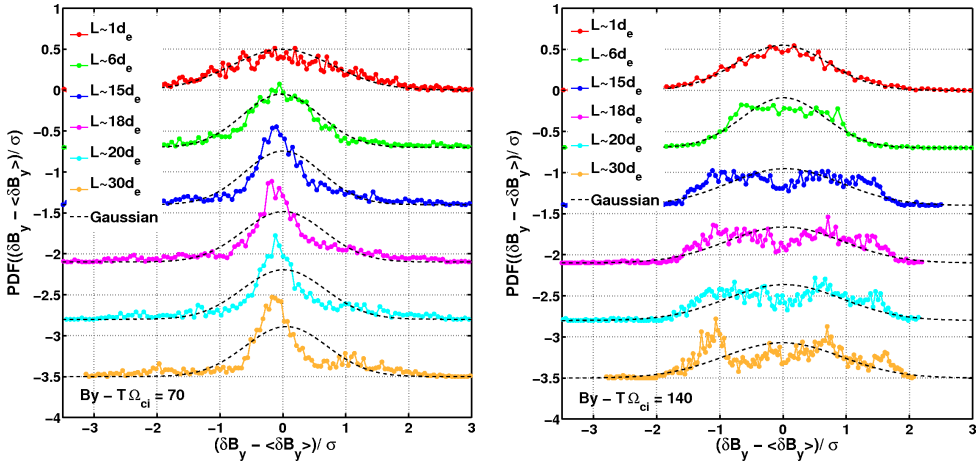

Figure 4.5: PDFs of the fluctuations $\delta B_y(L) = B_y(X+L) - B_y(X)$ of cut 4 at the time $T\Omega_{ci}$=70 (left) and 140 (right) and for $L = 1d_e, 6d_e, 15d_e, 18d_e, 20d_e$ and $30d_e$. All PDFs are centred on the mean value $< \delta B_y(L) >$ and normalized to the standard deviation σ to allow comparisons with a Gaussian distribution (dashed black lines). All curves are shifted along the y-axis for clarity.

the PDF of $\delta B_y(L)$ at $T\Omega_{ci}$=140 for cut 4 in the right panel of Fig. 4.5). Specifically, PDFs associated with all magnetic field components, $\delta B_i(L)$ at scales $L > 6d_e$, show departure from a unimodal distribution; this is not due to

poor statistics, it rather indicates the presence of large scale structures, such as the three large magnetic islands shown in the middle and lower panels of Figure 4.1. We also find the same result for the fluctuations associated with the x and z component of the magnetic field at $T\Omega_{ci}$=70.
Thus, only the fluctuations of the y-component of the magnetic field at the time $T\Omega_{ci}$=70 reveal PDFs with a clear underlying theoretical form. Specifically, $\delta B_y(L)$ shows unimodal non-Gaussian PDFs for scales L in the range $6d_e - 18d_e$ for all the cuts chosen for the analysis (e.g., see the PDFs of cut 4 in the left panel of Fig. 4.5). We identify this range as a potential range of turbulence. Then, we present analysis of B_y at $T\Omega_{ci}$=70.

Let us focus on the GSF of the fluctuations $\delta B_y(L)$ at $T\Omega_{ci}$=70 within the range of scales $L \sim 6d_e - 18d_e$ in order to test the generalized scaling expected for finite sized turbulent systems.
In the upper-right panel of Figure 4.6 we plot the third order of the structure function, $S_3(L)$, versus L. Here we can notice that, within the range of interest, S_3 increases with L for all cuts, as a signature of a high degree of correlation of the fluctuations. This suggests the presence of coherent structures whose typical length scale ranges between $6d_e$ and $18d_e$. Furthermore, by plotting $log(S_2(L))$ against $log(S_3(L))$, we can see that ESS holds for the fluctuations $\delta B_y(L)$ for all cuts chosen for the analysis (see upper-right panel of Fig. 4.6). We now test for intermittency by calculating the ratios $\zeta(2)/\zeta(3)$ for each cut, which corresponds to reading the gradient of the linear fits to the curves in the upper-left panel of Figure 4.6 within the potential range of turbulence. Then, in the lower panel of Figure 4.6 we plot $\zeta(2)/\zeta(3)$ for all the six cuts. The error bars are given by the variation between the exponent observed by the linear regression of $S_2(L)$ against $S_3(L)$ for all the values of L within the potential range of turbulence, and by the linear regression with the two extreme values of L not included. As we can see, the ratios $\zeta(2)/\zeta(3)$ are close to $2/3 \sim 0.66$ for all the cuts, suggesting therefore that the fluctuations are fractal. Moreover, this value is roughly constant (within error bars) across all the cuts, indicating consistency in the statistics.

In conclusion, this early stage of the reconnection shows magnetic field fluctuations in the y-component of the field, which are characterized by a non-Gaussian distribution and of fractal nature. This seems to be consistent with

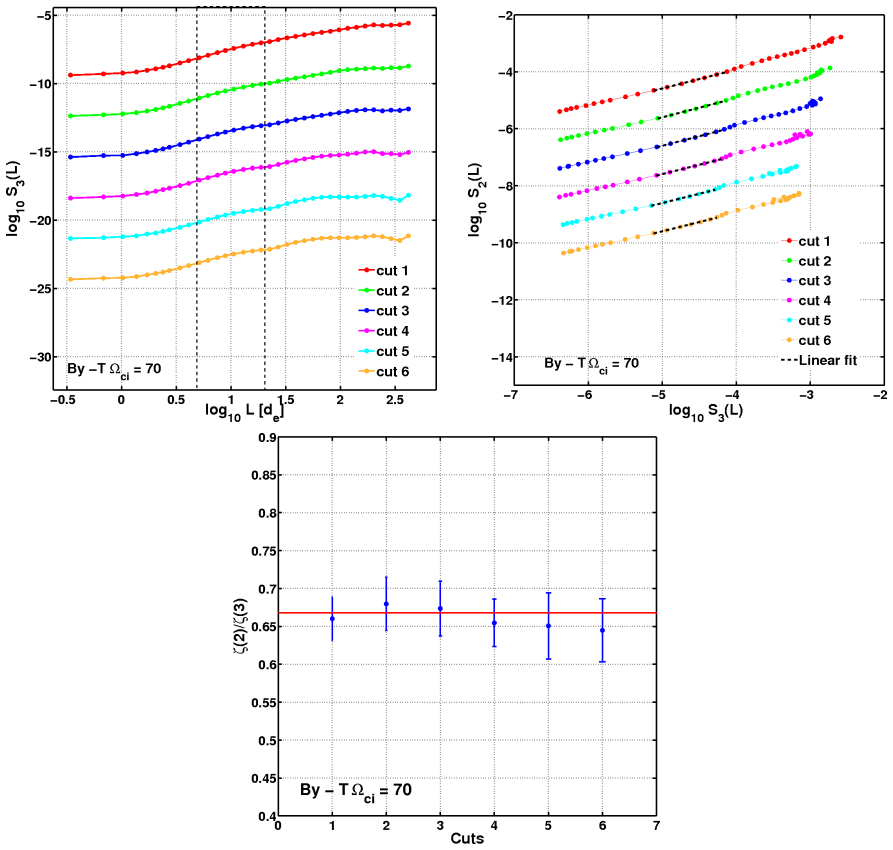

Figure 4.6: GSF and ESS analyses of the fluctuations $\delta B_y(L)$ at $T\Omega_{ci}$=70 for all the cuts of interest. *Upper-left panel:* log-log plots of S_3 vs L. Dashed black lines delimit the range of scales $6d_e < L < 18d_e$. *Upper-right panel:* ESS plot of $S_2(L)$ against $S_3(L)$ on logarithmic axes. Dashed black lines are linear fits to the curves within the range of scales under analysis. *Lower panel:* gradients of the linear fits to the curves in the upper-right panel, that is, the ratio $\zeta(2)/\zeta(3)$ for the six cuts. The red solid line indicates $y = 2/3 \sim 0.66$. All the curves shown in the upper panels are shifted on the y-axis for clarity.

K41 class of scaling (§ 1.2.3) and with what has been called "global scale-invariant dissipation" in the contest of kinetic range turbulence by Kiyani et al. [2009]. Here we do not investigate this latter result, however it points to a wider definition of intermittency in the sense of the K41 theory, which may underline a specific, although unknown, process in action in the turbulent cascade.

Next, we turn to a type of simulation which develops small scale magnetic structures only, in order to understand whether the fractal nature of the re-

connection generated fluctuations is due to the presence of the large scale structures (large magnetic islands) or not.

4.2.2 2D reconnection in an asymmetric configuration

We now focus on the 2D kinetic PIC simulation of reconnection with an asymmetric initial magnetic field. This simulation employs a Harris sheet with magnetic field $\mathbf{B} = B_{xo}tanh(z/\lambda)\mathbf{e_x} + B_{zo}\mathbf{e_z}$, where $\mathbf{e_x}$ and $\mathbf{e_z}$ are unit vectors, $\lambda = d_i$ is the initial half-thickness of the initial current layer, and B_{xo} and B_{zo} are two simulation parameters which depend on the initial guide field and determine the symmetry of the field. The simulation domain size is $L_x \times L_z = 300d_i \times 150d_i$, corresponding to 10240×5120 cells, and each cell contains 500 particles per species. Also in this simulation, an initial (small) perturbation is injected into the system to "promote" the formation of an X-line at the center of the simulation box. Note that this is just an initial perturbation, not a driven perturbation. The simulation also employs periodic boundary conditions in the X direction and conducting boundary conditions in the Z direction. Notice that although the simulation does not employs open boundary conditions, however it has much larger domain size compared to the previous simulation; as a consequence of this, the simulation proceeds longer before recirculation effects completely dominate [Daughton et al., 2006].

We present analysis of the y-component of the magnetic field, B_y, at two different times of the simulation, namely, at $T\Omega_{ci}$=70 and 164 (see Fig. 4.7). In this particular simulation, the asymmetry of the initial magnetic field prevents large magnetic structures to develop, instead small scale structures generate whose interactions is seen to lead to high variable dynamics suggestive of turbulence.

We investigate the statistical properties of the B_y fluctuations in the reconnection region, in order to detect and quantify this apparently turbulent dynamics. Thus, we take six cuts on the simulation grid within the reconnection region where the field is strongly fluctuating, and label them as cuts 1 to 6 (see Fig. 4.8).

For the two time slices of the simulation here considered, a spectral analysis of all magnetic field components reveals two different ranges of k

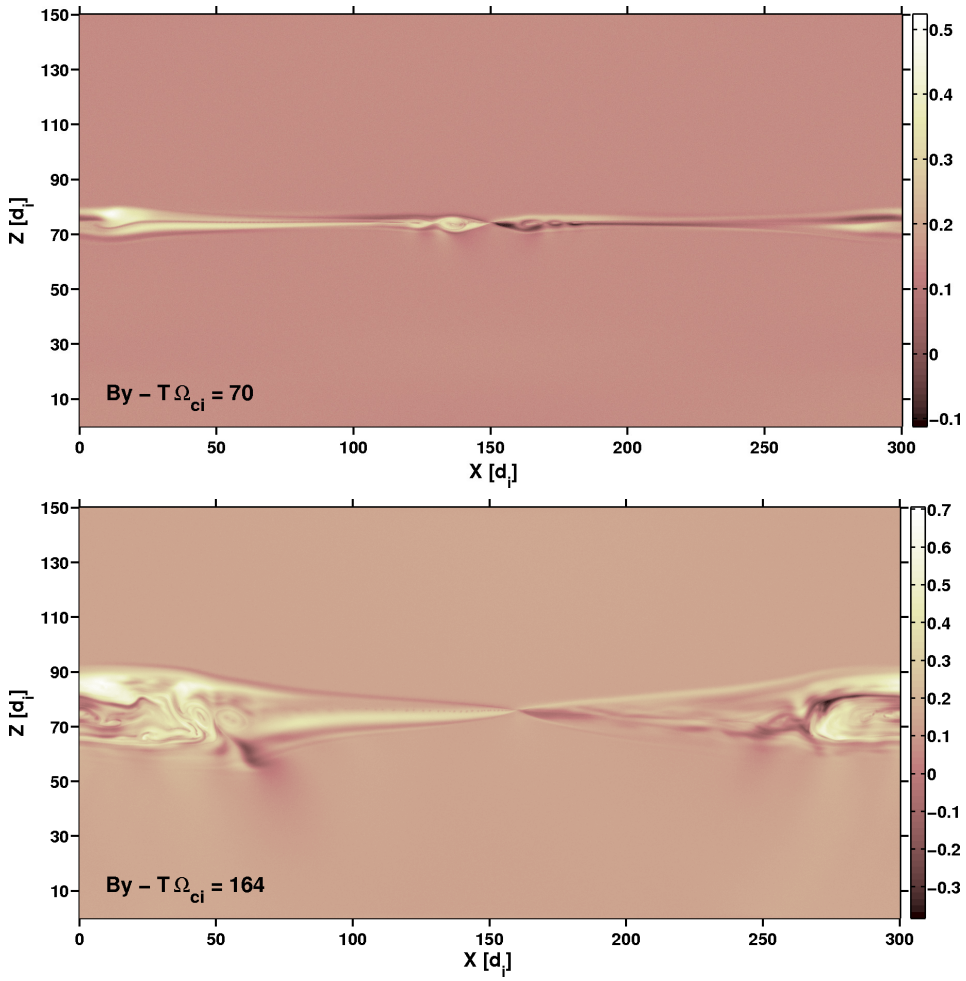

Figure 4.7: Plots of B_y at $T\Omega_{ci}$=70 (upper) and 164 (lower) for the 2D simulation of reconnection with an asymmetric configuration.

numbers for which a non-trivial power-law power scaling is observed (see Fig. 4.9): the range $0.1{d_e}^{-1} < k < 0.16{d_e}^{-1}$ at $T\Omega_{ci}$=70, and the range $0.05{d_e}^{-1} < k < 0.17{d_e}^{-1}$ at $T\Omega_{ci}$=164, which we identify as potential ranges of turbulence. Figure 4.9 shows that the PSD of the y-component of the magnetic field at both simulation times, have a higher level of the power compared to the other two components within the corresponding potential ranges of turbulence. This is also consistent with the values estimated of the total integrated field energy density of the PSD, E, over the corresponding ranges of interest as reported in Table 4.2.2. Hence, the reconnection generated fluctuations have the clearest signature in B_y, which we now focus on.

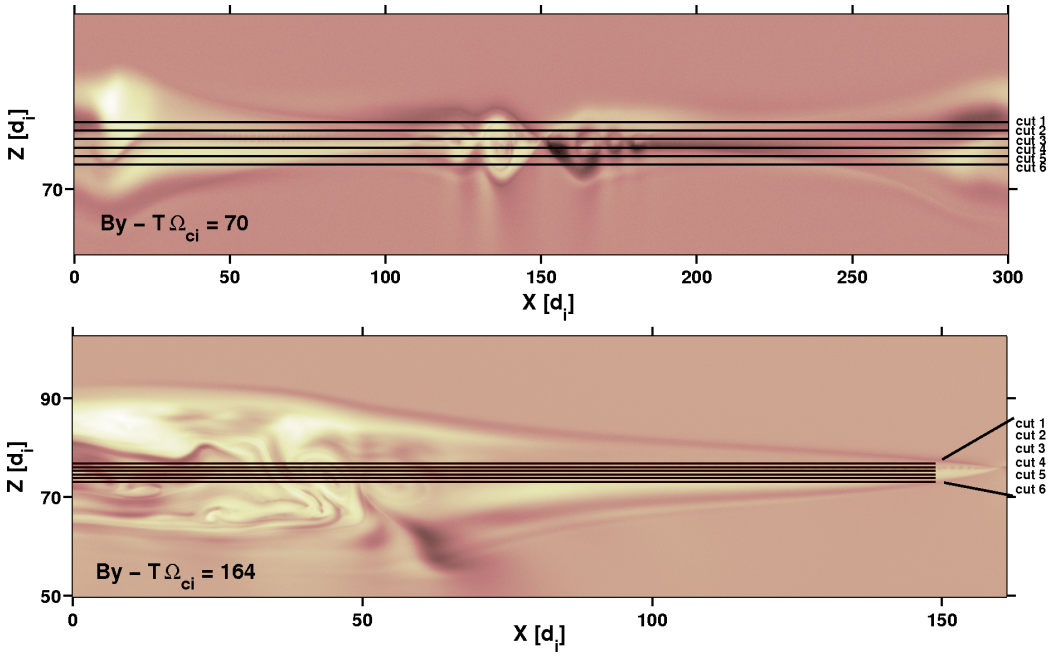

Figure 4.8: Zoom of B_y at $T\Omega_{ci}$=70 (upper) and 164 (lower) showing the reconnection regions where the cuts, labelled as cut 1 to 6, have been chosen for the analysis.

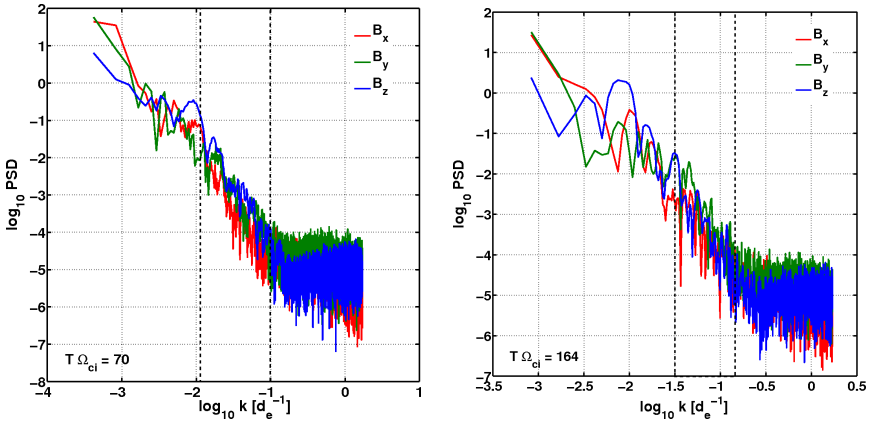

Figure 4.9: Log-log plots of the PSD of all components of the magnetic field at $T\Omega_{ci}$= 70 (left) and 164 (right) for a representative cut in the reconnection region. Dashed black lines delimit the range of k numbers which we shall see correspond to a potential range of turbulence.

Figure 4.10 shows that all cuts associated with B_y possess power-law PSDs within the range $0.1{d_e}^{-1} < k < 0.16{d_e}^{-1}$ at $T\Omega_{ci}$=70, and in the range

Simulation time	**$T\Omega_{ci} = 70$**			**$T\Omega_{ci} = 164$**		
k number range	$0.1{d_e}^{-1} < k < 0.16{d_e}^{-1}$			$0.05{d_e}^{-1} < k < 0.17{d_e}^{-1}$		
B component	B_x	B_y	B_z	B_x	B_y	B_z
E, energy density	0.17	0.48	0.35	0.05	0.16	0.06

Table 4.1: Total integrated field energy density of the PSD, E, over the potential turbulence ranges, for a representative cut within the reconnection region of all magnetic field components and simulation times of interest.

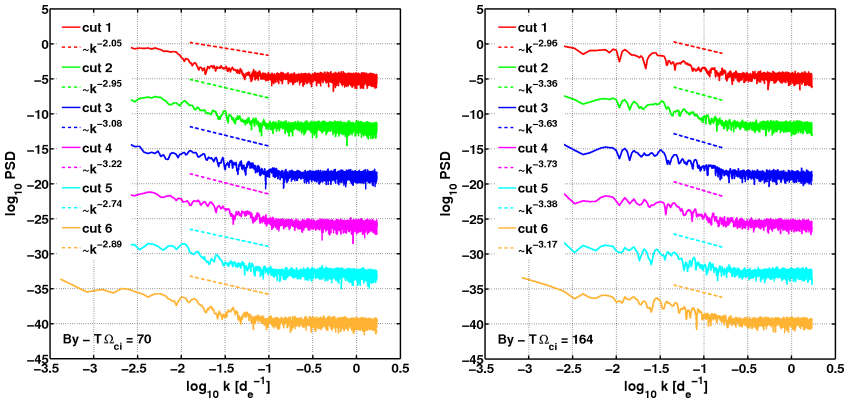

Figure 4.10: PSDs of B_y at $T\Omega_{ci}$=70 (left) and 164 (right) for the six cuts chosen for the analysis. Dashed lines are linear fits to the curves in the ranges $0.1{d_e}^{-1} < k < 0.16{d_e}^{-1}$ for $T\Omega_{ci}$=70 and $0.05{d_e}^{-1} < k < 0.17{d_e}^{-1}$ for $T\Omega_{ci}$=164, respectively. All PSDs are shifted along the y-axis for clarity.

$0.05{d_e}^{-1} < k < 0.17{d_e}^{-1}$ at $T\Omega_{ci}$=164, respectively. Furthermore, within both of these two distinct ranges, fluctuations $\delta B_y(L) = B_y(X+L) - B_y(X)$, show non-Gaussian distributions for all the cuts considered (e.g., see Fig. 4.11 for cut 4).

Now we test whether the fluctuations $\delta B_y(L)$ at $T\Omega_{ci}$=70 with $L \sim 10d_e - 60d_e$ and $\delta B_y(L)$ at $T\Omega_{ci}$=164 with $L \sim 6d_e - 22d_e$ show scaling in the structure function. Figure 4.12 shows the third order of the structure function, $S_3(L)$, against L for each time of the simulation here considered. We can see that, within the two different ranges of interest, S_3 increases with L for all cuts, indicating a high degree of correlation of the fluctuations. This suggests that, at an early stage of the process ($T\Omega_{ci}$=70), coherent structures with typical length scale $L \sim 10d_e - 60d_e$ develop; successively, at $T\Omega_{ci}$=164,

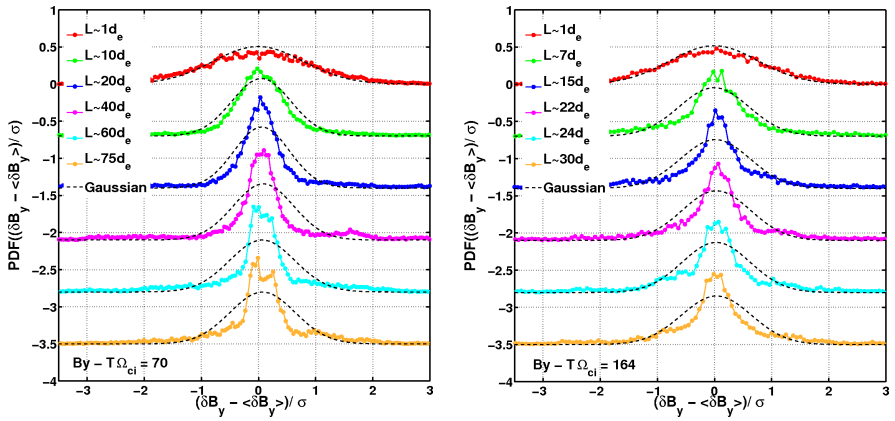

Figure 4.11: PDFs of the fluctuations $\delta B_y(L) = B_y(X+L) - B_y(X)$ of cut 4 at the time $T\Omega_{ci}$=70 (left) and 164 (right) for six different length scales L. All PDFs are centered on the mean value $< \delta B_y(L) >$ and normalized to the standard deviation σ to allow comparisons with a Gaussian distribution (dashed black lines). All curves are shifted along the y-axis for clarity.

these structures break giving rise to smaller coherent structures of size $L \sim 6d_e - 22d_e$.

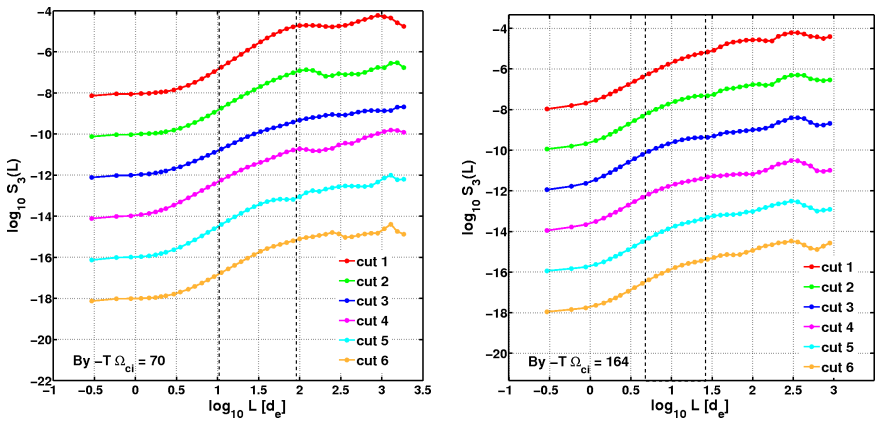

Figure 4.12: Log-log plots of S_3 vs L for all the cuts chosen for the analysis of $\delta B_y(L)$ at $T\Omega_{ci}$=70 (left) and 164 (right). Dashed black lines delimit the ranges of interest: $L \sim 10d_e - 60d_e$ for $T\Omega_{ci}$=70 and $L \sim 6d_e - 22d_e$ for $T\Omega_{ci}$=164. All curves are shifted on the y-axis for clarity.

Hence, the question that immediately arises is whether this fragmentation process (§ 1.5.3) occurs in a manner that is consistent with intermittent,

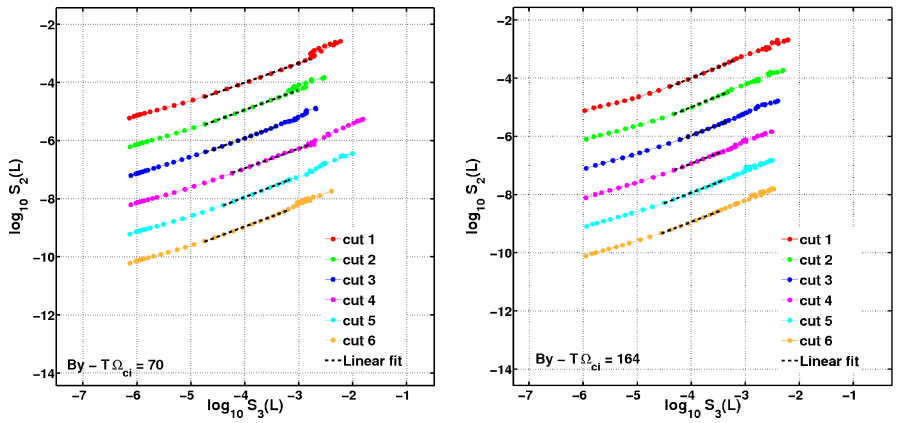

Figure 4.13: Log-log plots of $S_2(L)$ against $S_3(L)$ for all the cuts chosen for the analysis of the fluctuations $\delta B_y(L)$ at $T\Omega_{ci}$=70 (left) and 164 (right). Dashed black lines are linear fits to the curves within the corresponding range of scales under analysis. All curves are shifted on the y-axis for clarity.

multifractal turbulence. We test for this by plotting $S_2(L)$ versus $S_3(L)$ in a logarithmic scale for the fluctuations $\delta B_y(L)$ both at $T\Omega_{ci}$=70 and 164 (see Fig. 4.13). Importantly, we find that ESS holds for all the cuts and times of the simulation within the corresponding ranges of scales. The gradients of the linear fits to the curves in Figure 4.13 would therefore provide the ratios $\zeta(2)/\zeta(3)$. The left panel of Figure 4.14 shows $\zeta(2)/\zeta(3)$ for all the six cuts of B_y at the simulation time $T\Omega_{ci}$=70. Again, the error bars are obtained from the difference between the linear regression of $S_2(L)$ against $S_3(L)$ for all the values of L within the potential range of turbulence, and the linear regression with the two extreme values of L not included. Here we can see that the ratio $\zeta(2)/\zeta(3)$ is close to $2/3 \sim 0.66$ for all the cuts, suggesting therefore that the fluctuations are again fractal. This is also consistent with what we previously found for the fluctuations $\delta B_y(L)$ at $T\Omega_{ci}$=70 in the simulation with a symmetric initial magnetic field, suggesting that the fractal character of the reconnection generated fluctuations does not depend on the presence of large structures in the system. However, for the reconnection fluctuations at $T\Omega_{ci}$=164, the corresponding ratios $\zeta(2)/\zeta(3)$ significantly depart from 2/3 (see the right panel of Fig. 4.14) as a signature of the multifractal, intermittent, nature of the reconnection fluctuations. Thus, at later times of the simulation, the reconnection generated structures are characterized by a

multifractal spatial field consistent with intermittent turbulence.

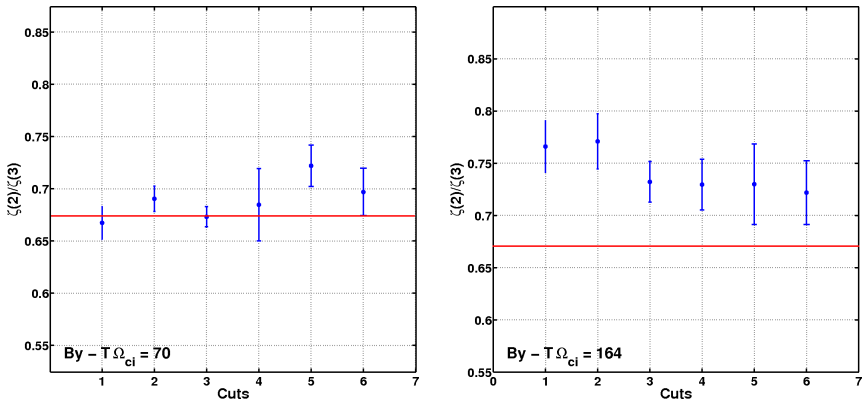

Figure 4.14: Ratios $\zeta(2)/\zeta(3)$ for the six cuts chosen for the analysis of the fluctuations $\delta B_y(L)$ at $T\Omega_{ci}$=70 (left) and 164 (right). Red solid lines indicate $y = 2/3$. Notice that for $T\Omega_{ci}$=164, $\zeta(2)/\zeta(3) \neq 2/3 \sim 0.66$, suggesting a multifractal, intermittent nature of the reconnection fluctuations.

Since both the Kolmogorov model and Iroshnikov-Kraichnan model for fractal turbulence predict $\zeta(3)$=1 and $\zeta(4)$=1 respectively, then we calculate all possible combinations of the scaling exponents ratio $\zeta(p)/\zeta(q)$ for $p, q = 1, 2, 3$ and 4 in order to detect any possible redundancy (e.g., $\zeta(p)/\zeta(3) = \zeta(p)$). As before, the error bars are obtained from the difference between the linear regression of $S_p(L)$ against $S_q(L)$ for all the values of L within the potential range of turbulence, and the linear regression with the two extreme values of L not included. The four panels on the left of Figure 4.15 show that all cuts of B_y at $T\Omega_{ci}$=70 have scaling exponent $\zeta(p)/\zeta(q)$ linear in p, again a signature of the fractal nature of the fluctuations; on the contrary, the four panels on the right of Figure 4.15 show that for B_y at $T\Omega_{ci}$=164, $\zeta(p)/\zeta(q)$ is quadratic in p for all the cuts, confirming therefore that the fluctuations at $T\Omega_{ci}$=164 are multifractal.

Classically, intermittency can be also quantified through the flatness (also know as kurtosis) of the probability distribution; indeed, the kurtosis of the PDF's turbulent fluctuations at scale L, is expected to decrease as L increases within the inertial range of turbulence [Frisch, 1995, p124].
The panel in Figure 4.16 shows the excess kurtosis versus the length scale L for a representative cut of $\delta B_y(L)$ at $T\Omega_{ci}$= 70 and 164. Here, we can see

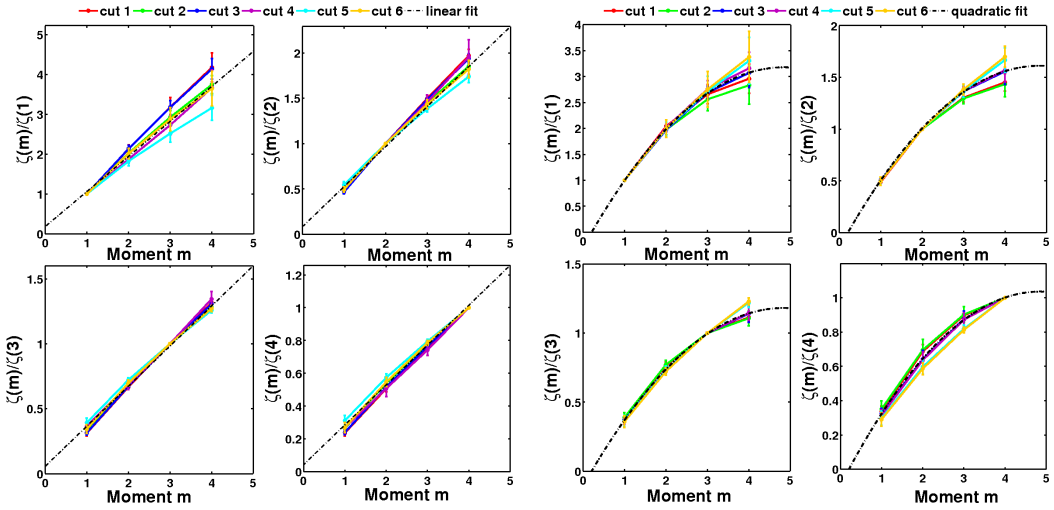

Figure 4.15: $\zeta(p)/\zeta(q)$ versus p for $q = 1$ to 4 for all cuts of B_y at $T\Omega_{ci}$=70 (left four panels) and 164 (right four panels). Dashed black lines are the best fits to the curves within uncertainty.

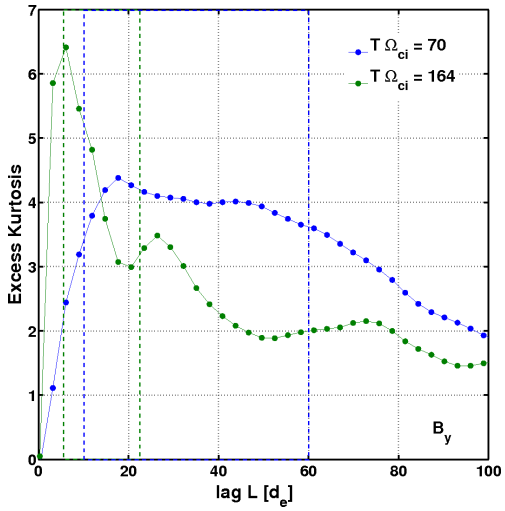

Figure 4.16: Excess kurtosis versus the space lag L for a representative cut of $\delta B_y(L)$ at $T\Omega_{ci}$= 70 (blue) and 164 (green). Dashed lines delimit the ranges of interest: $L \sim 10d_e - 60d_e$ for $T\Omega_{ci}$=70 (blue) and $L \sim 6d_e - 22d_e$ for $T\Omega_{ci}$=164 (green).

that within the corresponding ranges of interest, the reconnection generated fluctuations at $T\Omega_{ci}$= 70 have excess kurtosis roughly constant with L, while for the reconnection fluctuations at $T\Omega_{ci}$= 164 the excess kurtosis drastically

decreases with L, consistently with intermittent multifractal turbulence. Also, notice that the excess kurtosis at $T\Omega_{ci}$= 70 exhibits a peak at about 18 d_e, which then moves in time (at $T\Omega_{ci}$= 164) to smaller scales. This indicates that the reconnecting fluctuations become more and more intermittent as we move to smaller scale at later times of the simulation.

The fact that the reconnection generated fluctuations at $T\Omega_{ci}$= 70 are fractal and non-Gaussian distributed and show a slightly dependence of the flatness on L, seems again to be consistent with the K41 class of scaling (§ 1.2.3) and with a global scale-invariant process [Kiyani et al., 2009].
On the other hand, the fact that at $T\Omega_{ci}$=164 the reconnection generated fluctuations are multifractal suggests that dissipation, in the sense of conversion of magnetic to kinetic energy, in collisionless reconnection on kinetic scales has an analogue in dissipation in fluid-like turbulent phenomenology, in that it proceeds via a spatial multifractal field of structures generated by an intermittent cascade. If this is the case, then the spatial dissipation field will also be multifractal. We now test for this.

We apply the box counting analysis to each component of the dissipation field (see Eqn. (1.30)), $\mathbf{J} \cdot \mathbf{E}$, at $T\Omega_{ci}$=164, in order to investigate its topology. Thus, we calculate both global and local fractal dimension (see § 2.1.1 and also Mandelbrot [1977]) for a reconnection dominated turbulent region.
The box-counting method consists of dividing a spatial region into boxes of size L using a regular grid, and then counting the number of boxes $N(L)$ that contain non-zero values of a discretized spatial field. We consider the magnitude of each component of $\mathbf{J} \cdot \mathbf{E}$ and the discretized values are non-zero where it exceeds a threshold, which identifies the background noise.
For fractal geometries N(L) is expected to depend linearly upon L, while non-linear trends of N(L) against L indicate a multifractal field. In Figure 4.17 we plot N(L) versus L within a reconnection dominated turbulent region. Here we can see that the plot introduces a slight curvature. Also, the inset of Figure 4.17 shows that the local dimension, n(L) = d ln(N(L)) / d ln(L), is not constant but increases with L up to scales $\sim 20 d_e$ as a signature of multifractality. Thus in this 2D simulation, the reconnection generated fluctuations at kinetic scales possess statistical and topological properties consistent with a

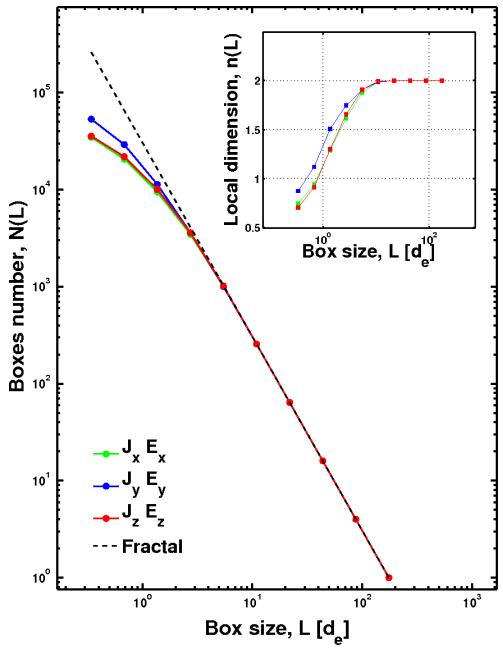

Figure 4.17: **Box-counting method.** Plot of the number of boxes, N(L), versus the box size L within a reconnection dominated turbulent region for each component of $\mathbf{J} \cdot \mathbf{E}$. The inset figure shows the corresponding local dimension, n(L) = d ln(N(L))/d ln(L), against the box size L.

multifractal (intermittent) weakly turbulent field.

4.3 3D magnetic reconnection

Recently Daughton et al. [2011] have demonstrated that 3D fully kinetic PIC simulations of reconnection in collisionless plasmas show the presence of tearing instabilities within electron-scale layers, which give rise to numerous magnetic flux ropes. The subsequent non-linear interaction of these flux ropes is seen to lead to a self-generated turbulence, which generates structures on multiple scales within the initially laminar ion-scale current layer.
In this section we aim to detect and quantify the turbulent mechanism qualitatively observed in these simulations in order to understand whether the multi-scale nature of these structures is important for dissipation phenomena during the reconnection process (§ 1.5.3).

The simulation here analysed was carried out on the petascale super-

computer Kraken using a kinetic PIC description which self-consistently advances the full relativistic particle equations of motion and Maxwell's equations. It is initialized with a Harris current sheet with magnetic field $\mathbf{B} = B_{xo}tanh(z/\lambda)\mathbf{e_x} + B_{yo}\mathbf{e_y}$, where $\mathbf{e_x}$ and $\mathbf{e_y}$ are unit vectors, $B_{yo} = B_{xo} = B_0$ is the uniform guide field and $\lambda = d_i$ is the initial half-thickness, where d_i is an ion inertial length. The ion electron mass ratio is $m_i/m_e = 100$, which implies that d_i is $10d_e$, the electron inertial length. The simulation employs open boundary conditions in the X and Z directions and periodic boundary conditions in the Y direction. The dimensions of the simulation grid are $L_x \times L_y \times L_z = 70d_i \times 70d_i \times 35d_i$, corresponding to $2048 \times 2048 \times 1024$ cells.

We present statistical analysis of all components of the magnetic field, $\mathbf{B}$, in the X-Z plane, at Y=$35d_i$ and at the simulation time $T\Omega_{ci}$=78 (see Fig. 4.18). This time slice corresponds to a later stage of the magnetic reconnection in which the turbulence power is seen to reach its peak.

4.3.1 Coherent structures and scaling laws

The goal of this section is to characterize the statistical properties of the reconnection generated fluctuations and, importantly, distinguish the latter from the fluctuations generated by the background noise which arises from the PIC simulation [Birdsall and Langdon, 1985]. Thus, we apply statistical techniques to the magnetic field spatial fluctuations by taking six cuts on the simulation grid and label them as cut 1 to 6 (see Fig. 4.18). All cuts lie within the reconnection region where the field is strongly fluctuating except for cuts 1 and 6, which lie where there is negligible signature of reconnection. The latter are taken to quantify the effects of the PIC simulation noise. Hence, we investigate on scaling behaviours of the fluctuations associated either with the reconnection region (cuts 2 to 5) and with the region where the PIC noise is dominant (cuts 1 and 6).

Let us begin analysing how the reconnection generated fluctuations are distributed. The fluctuations $\delta B_i(L) = B_i(X + L) - B_i(X)$ reveal different statistics for each component of the magnetic field. Fluctuations associated with B_x and B_y show nearly Gaussian statistics, while $\delta B_z(L)$ reveals non-

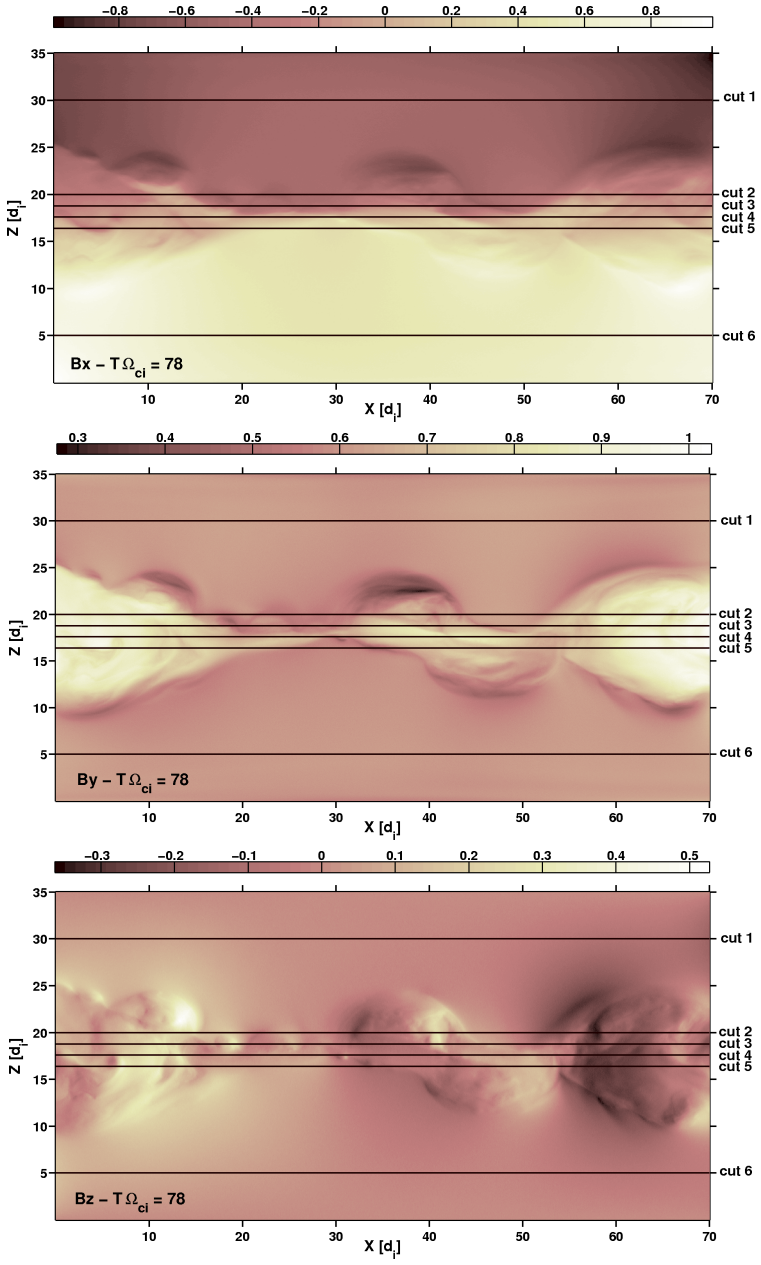

Figure 4.18: Plots of the magnetic field components B_x (upper), B_y (center) and B_z (lower) in the X-Z plane at Y=$35d_i$ and at the simulation time $T\Omega_{ci}$=78. Solid black lines show the six cuts on the simulation grid chosen for the analysis.

Gaussian PDFs at scales $4d_e < L < 25d_e$ (e.g., see Fig. 4.19 for the PDFs of cut 4). We identify this range as a potential range of turbulence. Moreover,

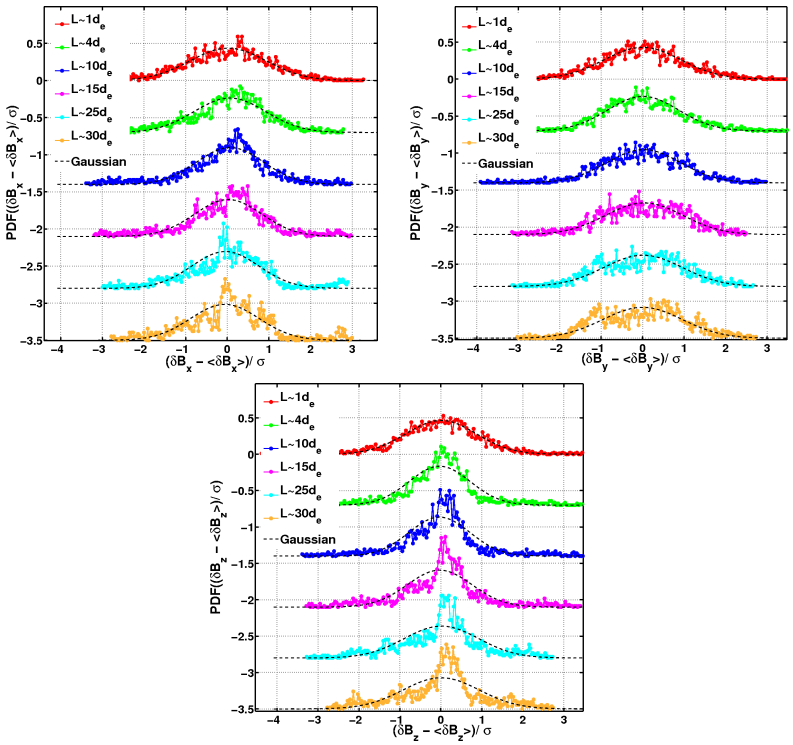

Figure 4.19: PDFs of cut 4 (reconnection region) for $\delta B_x(L)$ (upper-left), $\delta B_y(L)$ (upper-right) and $\delta B_z(L)$ (lower) at $T\Omega_{ci}$=78 and for six different space lags L. All PDFs are centered on the mean value $< \delta B_i(L) >$ and normalized to the standard deviation σ to allow comparisons with a Gaussian distribution (dashed black lines). All curves are shifted along the y-axis for clarity.

we have also analysed the magnetic field fluctuations within the reconnection region in the Y-direction, that is, $\delta B_i(L) = B_i(Y+L) - B_i(Y)$ - i.e. by taking cuts along the vertical direction with respect to the simulation grid - and found that they are described by Gaussian statistics (here not shown). However, we attribute this result to a poor statistics, which arises from the fact that the width of the reconnection region along the Z-axis (see Fig. 4.18) is small[1].
On the other hand, fluctuations associated with the region where there is negligible signature of reconnection (cuts 1 and 6) are Gaussian distributed up to scales $L \sim 100d_e = 10d_i$ (e.g., see Fig. 4.20 for cut 1 of $\delta B_z(L)$).

[1]The typical length of a vertical cut within the reconnection region is $\sim 15d_i$ corresponding to about 400 data points.

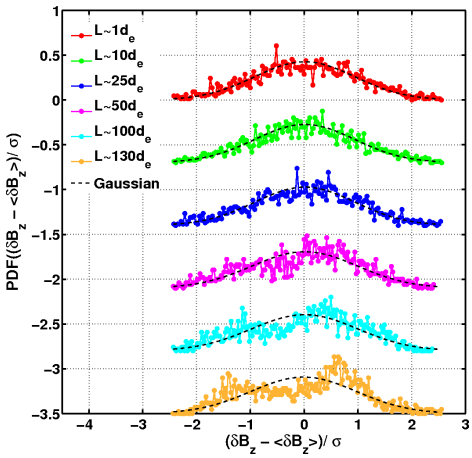

Figure 4.20: PDFs of cut 1 associated with the fluctuations $\delta B_z(L)$ within a region where the PIC noise is dominant. All PDFs are centered on the mean value $< \delta B_z(L) >$ and normalized to the standard deviation σ to allow comparisons with a Gaussian distribution (dashed black lines). All curves are shifted along the y-axis for clarity.

The fact that $\delta B_x(L)$ and $\delta B_y(L)$ show Gaussian PDFs may indicate that the

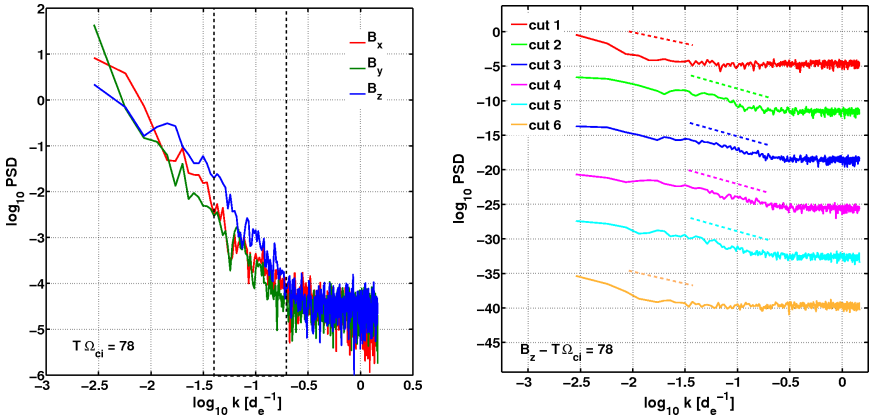

Figure 4.21: *Left panel:* log-log plot of the PSD of all components of the magnetic field at $T\Omega_{ci}$=78 and for a representative cut in the reconnection region. Dashed black lines delimit the range of k numbers corresponding to the potential range of turbulence. *Right panel:* log-log plot of the PSD of B_z at $T\Omega_{ci}$=78 for all the cuts chosen for the analysis. Dashed lines are linear fits to the curves in the range $0.04{d_e}^{-1} < k < 0.25{d_e}^{-1}$ for cuts 2 to 5 (reconnection region), and within the range $0.008{d_e}^{-1} < k < 0.04{d_e}^{-1}$ for cuts 1 and 6 (noise region). All spectra are shifted along the y-axis for clarity.

turbulence power is much weaker in the x and y component of the field rather than in the z-component. We then switch to the analysis of the power spectrum with the aim to test this anisotropy. The left panel of Figure 4.21 shows the PSDs of all magnetic field components at $T\Omega_{ci}$=78 for a representative cut within the reconnection region. We can see that, within the range of k numbers corresponding to the potential range of turbulence, the level of the power is higher in the z-component of the field compared to the other two components, B_x and B_y. Notice also that this asymmetry is much more pronounced in 3D compared to 2D (cf. the left panel of Fig. 4.3 and both panels of Fig. 4.9). Specifically, the total integrated field energy density over the turbulent range of the power spectral density is ~ 0.1 that of the background field for B_z against ~ 0.02 for B_x and B_y. The reconnection generated fluctuations are therefore highly anisotropic in character and have clearest signature in their z-component which is perpendicular to the X-Y plane of the macroscopic field of these simulations. This anisotropy parallels what has been recently observed both in kinetic range turbulence in the solar wind [e.g., Turner et al., 2012; Kiyani et al., 2013] and in a reconnection jet [Huang et al., 2012].
Importantly, notice that the reconnection generated fluctuations (cuts 2 to 5) show power-law power spectra within the potential range of turbulence with spectral indices $\alpha \sim 3.3$ on average across the cuts (right panel of Fig. 4.21); while in the noise region, cuts 1 and 6 show power-law power spectra with spectral indices $\alpha \sim 2$ up to $k \sim 0.04{d_e}^{-1}$, beyond which they show flat spectra (uncorrelated white noise). This suggests that the PIC noise behaves as Brownian (coloured) noise at scales $L > 25d_e$.
We also analysed an early and late phase of the reconnection process at $T\Omega_{ci}$ = 40 and 98 respectively, and find that the reconnection generated fluctuations evolve in time: at early time the power in these fluctuations is weak though above the noise, then it grows in amplitude up to the middle phase at $T\Omega_{ci}$ = 78 in which the turbulence quantitatively reaches its peak of evolution (see Fig. 4.22).

In summary, only the fluctuations associated with the z-component of the magnetic field show the characteristic features of turbulent fluctuations, that is, power-law power spectra and non-Gaussian PDFs. However, these properties by themselves do not fully quantify a turbulence process. A distinc-

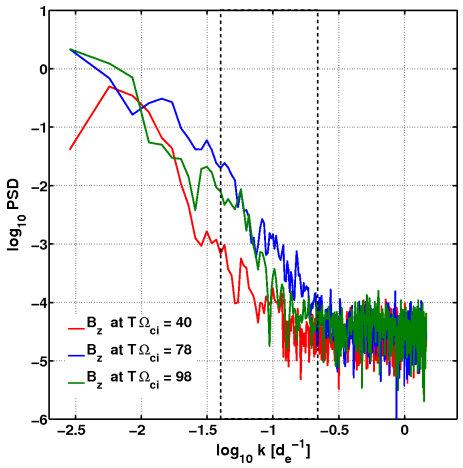

Figure 4.22: Log-log plot of the PSD of B_z at $T\Omega_{ci}$=40, 78 and 98, and for a representative cut in the reconnection region. Dashed black lines delimit the range of k numbers corresponding to the potential range of turbulence.

tive characteristic of turbulence is that the PDFs of non-Gaussian fluctuations at different scales are related by a multifractal similarity or scaling [e.g., Bruno and Carbone, 2005; Chapman et al., 2009; Chapman and Nicol, 2009]. Now we test this by examining the GSF of the magnetic field fluctuations $\delta B_z(L)$.

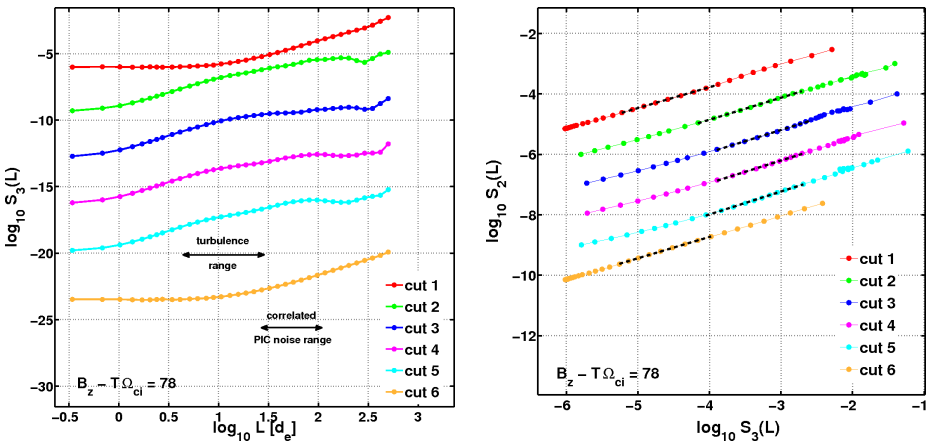

Figure 4.23: *Left panel:* log-log plot of S_3 against L for cuts 1 to 6. *Right panel:* log-log plot of S_2 against S_3 for all the cuts of interest. Dashed black lines correspond to the linear regression fits in the potentially turbulent range $4d_e < L < 25d_e$ for cuts 2 to 5 and within the range $25d_e < L < 100d_e$ for cuts 1 and 6. All curves in both panels are shifted along the y-axis for clarity.

In the left panel of Figure 4.23 we plot the third order of the structure function, S_3, versus L on a logarithmic scale for all the cuts considered. We observe that all cuts show a high degree of correlation but within different ranges of scales: reconnection generated fluctuations (cuts 2 to 5) are highly correlated in the range $4d_e < L < 25d_e$, which is the potential turbulent range, while fluctuations associated with the noise region (cuts 1 and 6) reveal a high degree of correlation at length scales $L > 25d_e$. This indicates the presence of coherent structures (e.g., flux ropes) in the reconnection (turbulent) region with typical length scale $4d_e < L < 25d_e$; while, the fact that the noise generated fluctuations are also correlated within the range $25d_e < L < 100d_e$ is a further evidence that the PIC noise, at these scales, behaves as Brownian correlated noise. On the contrary, at scale $L < 25d_e$, the PIC noise is uncorrelated, white noise.
The right panel of Figure 4.23 finally shows evidence of the ESS for the reconnection generated fluctuations $\delta B_z(L)$. Here, we see that ESS holds for both cuts 1 and 6, which are simulation noise, and cuts 2 to 5, which are within the potentially turbulent range implying that both noise and reconnection generated fluctuations have a range of scale invariance. Now, the question that immediately arises is whether these fluctuations are multifractal or not.

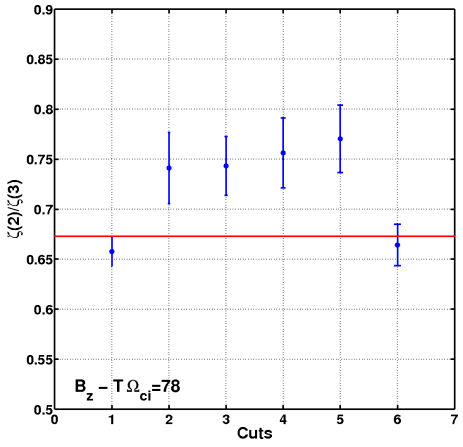

Figure 4.24: $\zeta(2)/\zeta(3)$ versus p for all the cuts chosen for the analysis of B_z at $T\Omega_{ci}$=78. The red solid line indicates $y = 2/3 \sim 0.66$.

Thus, we read the gradients of the linear fits to the curves in the right panel of Figure 4.23, which would provide the ratio $\zeta(2)/\zeta(3)$. Figure 4.24

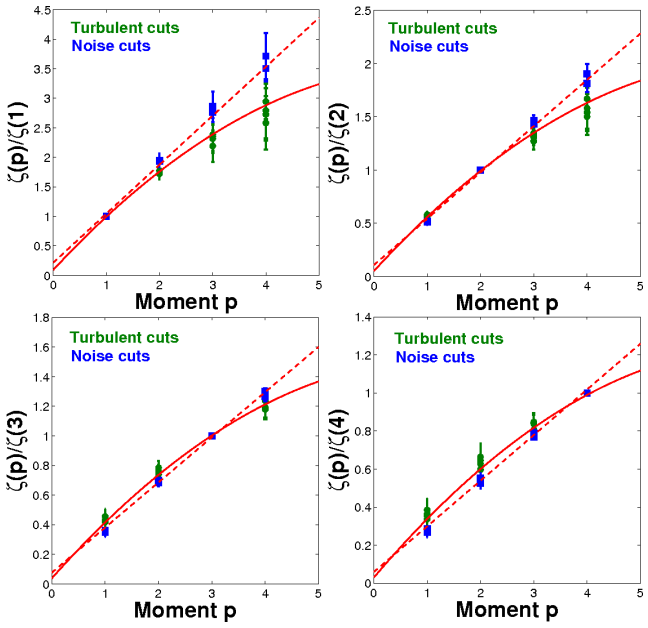

Figure 4.25: $\zeta(p)/\zeta(q)$ versus p for cuts 1 and 6 (blue rectangles) and cuts 2 to 5 (green dots) and for $q = 1$ (top-left), 2 (top-right), 3 (bottom-left) and 4 (bottom-right). Solid and dashed red lines are the best fits to the curves within uncertainty for the turbulent (cuts 2-5) and noise (cuts 1,6) cuts respectively.

shows $\zeta(2)/\zeta(3)$ for all the six cuts of B_z. The error bars are obtained as per above, from the difference between the linear regression of $S_2(L)$ against $S_3(L)$ for all the values of L within the corresponding ranges of interest, and the linear regression with the two extreme values of L not included. Here we can see that the ratio $\zeta(2)/\zeta(3)$ is close to $2/3 \sim 0.66$ for cuts 1 and 6 associated with the PIC noise suggesting therefore that these fluctuations are fractal; while the reconnection generated fluctuations depart significantly within errors from 0.66. This is the evidence of the multifractal nature of the fluctuations in the reconnection region. We also calculate all possible combinations of the scaling exponents ratio $\zeta(p)/\zeta(q)$ for $p, q = 1, 2, 3$ and 4 by plotting $\log(S_p)$ versus $\log(S_q)$ and by reading the gradients of the linear fits to these curves within the potentially turbulent range, $4d_e < L < 25d_e$, for cuts 2 to 5 and in the noise range, $25d_e < L < 100d_e$, for cuts 1 and 6. Error bars are estimated as explained before. The panels in Figure 4.25 show the ratios $\zeta(p)/\zeta(q)$ versus p for $q = 1$ up to 4 for cuts 1 and 6 (noise) and cuts 2 to 5 (reconnection-

fluctuations). The noise cuts (blue rectangles) show a linear behaviour of $\zeta(p)$ with p, again consistent with a fractal field. The PIC noise thus generates a spatial field of magnetic fluctuations which is a self-affine Brownian noise showing fractal scaling. Importantly, it is clearly distinguishable from the reconnection generated fluctuations of cuts 2 to 5 (green dots), which instead consistently show a non-linear dependence of $\zeta(p)$ on p within uncertainty. The reconnection generated structures are thus robustly characterized by a multifractal spatial field, which is also a key signature of a multifractal intermittent turbulence phenomenology.

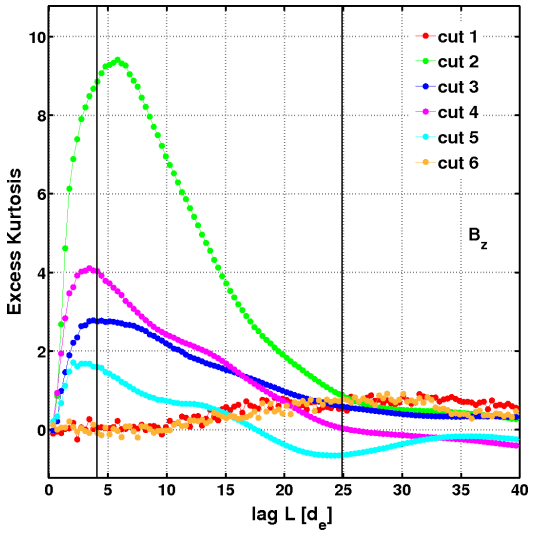

Figure 4.26: Excess kurtosis of the PDF of $\delta B_z(L)$ versus the space lag L for all the cuts. Solid black lines delimit the range of scales $4d_e < L < 25d_e$, which identifies the turbulent range.

As we saw earlier, the classical measure of intermittency makes use of the kurtosis which, for turbulent fluctuations at scale L, is expected to decrease as L increases within the inertial range. In Figure 4.26 we plot the excess kurtosis of the fluctuations $\delta B_z(L)$ against L for all the cuts. Again, we can see that within the turbulent range $4d_e < L < 25d_e$, the reconnection generated fluctuations (cuts 2 to 5) have excess kurtosis decreasing with L. This is a further confirmation of the intermittent nature of the reconnection fluctuations. On the contrary, the noise fluctuations have nearly null kurtosis consistent with Gaussian statistics, which instead decreases as we move to

smaller scales.

In conclusion, the reconnection generated fluctuations at kinetic scales possess all the statistical properties that classically characterize fluid-like intermittent multifractal turbulence suggesting that they share the same phenomenology. In particular, this means that dissipation in the sense of conversion of magnetic to kinetic energy, in collisionless reconnection on kinetic scales has an analogue in dissipation in fluid-like turbulent phenomenology, in that it proceeds via a spatial multifractal field of structures generated by an intermittent cascade. If this is the case, then the spatial dissipation field will also be multifractal. We shall test this idea in the next section.

4.3.2 Intermittent energy dissipation

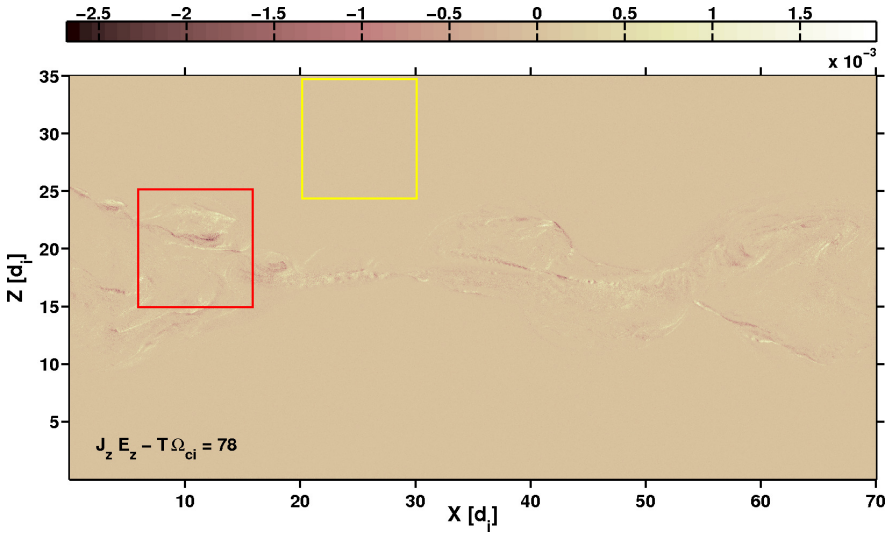

Figure 4.27: Plot of the z-component of $\mathbf{J} \cdot \mathbf{E}$ in the X-Z plane at Y=$35d_i$ and at the time $T\Omega_{ci} = 78$ of the simulation. Red and yellow squares indicate respectively the turbulent and noise regions over which we perform the box counting analysis of $\mathbf{J} \cdot \mathbf{E}$.

In this section we present the application of the box counting analysis to the dissipation field $\mathbf{J} \cdot \mathbf{E}$ (see Eqn. (1.30)) in order to investigate its topology. We show results for the three components of $\mathbf{J} \cdot \mathbf{E}$, at the same time-space slice of the simulation analysed in the previous section. We perform the classical box counting method to calculate both global and local fractal dimension (see

§2.1.1) for a reconnection dominated turbulent region and a region where noise is dominant.

We consider the magnitude of each component of $\mathbf{J}\cdot\mathbf{E}$ and the discretized values are non-zero where it exceeds a threshold, which identifies the background noise. Then, we test the robustness of our results by varying this threshold. For sufficiently small thresholds, this yields the topology of the noise field, but for thresholds above the noise, we obtain the topology of the turbulence. Box counting the thresholded turbulent field then gives its spatial topology in the absence of noise, without the need of filtering or averaging.

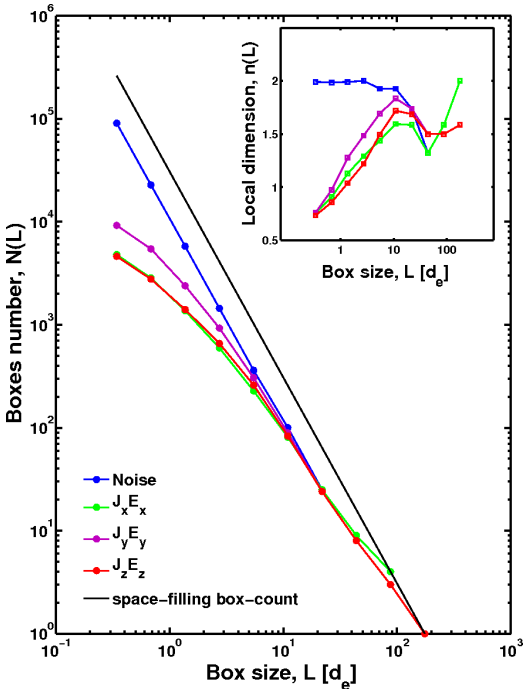

Figure 4.28: **Box-counting method.** Plot of the number of boxes, N(L), versus the box size L within a reconnection dominated turbulent region (red square in Fig.4.27) and a noise region (yellow square in Fig.4.27) for each component of $\mathbf{J}\cdot\mathbf{E}$. The inset figure shows the corresponding local dimension, n(L) = d ln(N(L))/d ln(L), against the box size L.

In Figure 4.28 we plot N(L) versus L within the reconnection dominated turbulent region and the noise region indicated respectively by the red and yellow squares in Figure 4.27. The noise region shows a linear behaviour of $N(L)$ with L indicating that the PIC noise is fractal, on the contrary, in the

turbulent region the plot introduces curvature for scales L smaller than $\sim 25d_e$. The inset of Figure 4.28 also shows how the local dimension, n(L), varies with the scale L. Within the noise region, the fractal dimension is roughly constant as L varies, while it changes with the scale L in the turbulent region, again providing evidence of multifractality. This is a further evidence that magnetic energy dissipation occurs in a spatially intermittent manner.

4.4 Conclusions

4.4.1 Results summary

In this chapter we focused on fully kinetic (PIC) simulations of collisionless magnetic reconnection in 2D and 3D geometries. In both cases, the simulations were initialized with a Harris current sheet, which determines the initial magnetic field configuration. We quantified the ensemble averaged statistical properties of the spatial fields of fluctuations in the magnetic field in order to probe possible turbulent mechanisms in action during the reconnection process.

For the 2D simulations, we studied two different configurations of the initial magnetic field: a symmetric and an asymmetric configuration. In both cases we found that the reconnection generated fluctuations are anisotropic in terms of power level of turbulence and have have the clearest signature in B_y.

At an early time ($T\Omega_{ci}$=70) of the 2D simulation with a symmetric configuration, the reconnection generated fluctuations of B_y at scales $L \sim 6d_e - 18d_e$, revealed power-law power scaling in the PSDs and non-Gaussian PDFs consistent with fluid-like turbulence. Nevertheless, the ESS analysis showed that these fluctuations are fractal in character indicating a dissipation phenomenology distinct from intermittent dissipation via multifractal structures (see §1.3.1). At later times of this simulation, large coherent structures develop in the reconnection region, which seem to quench the turbulence organizing the magnetic flow into well defined, symmetric large islands. In this case, indeed, the reconnection fluctuations showed Gaussian PDFs. Then we moved to the analysis of the 2D simulation with an asymmetric configuration in order to understand if the fractal nature of the reconnection generated

fluctuations is due to the presence of these large coherent structures.

The 2D simulation with an asymmetric configuration revealed that, at an early time of the simulation ($T\Omega_{ci}$=70), the fluctuations $\delta B_y(L)$ possess the same statistical properties of the reconnection fluctuations of the simulation with symmetric configuration at $T\Omega_{ci}$=70: power-law power scaling in the PSD, non-Gaussian PDF and fractal scaling of the GSF. However, at later time of the simulation ($T\Omega_{ci}$=164), when small scale coherent structures form, we find that the fluctuations $\delta B_y(L)$ at scales $L \sim 6d_e - 22d_e$, show non-Gaussian PDFs and multifractal similarity. Consistently, the box-counting analysis of each component of $\mathbf{J}\cdot\mathbf{E}$ revealed a multifractal topology of the dissipation field. Even though we find that the reconnection generated fluctuation and the $\mathbf{J}\cdot\mathbf{E}$ topology are multifractal, their scaling only slightly departs from being fractal. Furthermore, the turbulent range spans scales of only a few d_e, suggesting that in this 2D simulation, reconnection leads to a weakly intermittent turbulence. The question then arose as whether the 2D geometry of the simulation is important for a strong intermittent (multifractal) turbulence to develop. Thus we turned to the study of a simulations of magnetic reconnection in 3D in order to answer this question.

The 3D simulation of reconnection at the simulation time $T\Omega_{ci}$=78, revealed that the reconnection generated fluctuations are anisotropic in terms of power level of turbulence and have the clearest signature in B_z. We found that the fluctuations $\delta B_z(L)$ exhibit the hallmarks of finite range fluid-like turbulence within the range of scales $L \sim 4d_e - 25d_e$. Specifically, they possess non-Gaussian distributions with decreasing excess kurtosis with L as a signature of the intermittent nature of the reconnection fluctuations; they also exhibit ESS consistent with a multifractal scaling. This was confirmed by the box-counting analysis of the spatial dissipation field, which also showed a multifractal topology. These signatures are recovered quite robustly across the regions in the simulation domain where reconnection is actively generating fluctuations and were clearly distinguished from the fluctuations generated by the PIC noise, which instead revealed to be correlated fractal Brownian noise at large scales ($25d_e < L < 100d_e$), while uncorrelated white noise at small scales ($L < 25d_e$).

4.4.2 Discussions

In this chapter we focused on fully kinetic PIC simulations of reconnection in a collisionless plasma in both a 2D and 3D geometry. In these simulations the initial current layer is seen to become unstable to plasmoids via tearing instabilities; then, fragmentation processes occur leading to the formation of coherent structures on multiple scales (e.g., magnetic islands in 2D and flux ropes in 3D) and, in some cases, turbulent mechanisms have been observed to arise. We investigated whether this fragmentation process leads to a turbulent reconnection or not.

The early phase of the 2D magnetic reconnection with a symmetric configuration revealed a turbulence outset, which is soon killed off at later times. Indeed, at $T\Omega_{ci}$=140 and 200 the magnetic flux organize in very smooth large islands and the turbulence is quenched. This may due to the fact that in a 2D geometry small scale magnetic structures cannot move relative to each other in the third direction, since they are forced to lie in a plane forming large structures. However, the 2D simulation without large magnetic islands (asymmetric configuration) at later times ($T\Omega_{ci}$=164) leads to a weakly intermittent turbulent reconnection, suggesting that the coherent structures can actually interact non-linearly with each others despite the 2D topology of the system. While at the simulation time $T\Omega_{ci}$=164, the 2D simulation with asymmetric initial magnetic field shows a weakly intermittent turbulence, on the contrary, at $T\Omega_{ci}$=78, in the 3D simulation, turbulence is already developed into a strong intermittent turbulence. The third dimension, indeed, seems to allow small scale coherent structures to evolve freely and quickly leading to a fully evolved intermittent turbulence. Hence, we conclude that whether the topology of the system allows turbulence to arise during reconnection in collisionless plasmas, then the process proceeds faster and shows a stronger turbulence in 3D than in 2D.

Remarkably, the presence of intermittent (multifractal) turbulence in collisionless reconnection on kinetic scales means that dissipation, in the sense of conversion of magnetic to kinetic energy, has an analogue in dissipation in fluid-like turbulent phenomenology, in that it proceeds via a spatial multifractal field of structures generated by an intermittent cascade. This finding then provides a starting point for theoretical models of heating in collisionless recon-

nection; it also suggests that existing analytical and quasi-analytical models of reconnection that do not take into account the development of turbulence in the reconnection layer may need revision.

Finally, it has been suggested in MHD formalisms that the reconnection rate is influenced by the level of turbulence (Lazarian and Vishniac [1999]; Kowal et al. [2009], see also § 1.5.3). The reconnection rate in these kinetic simulations is fast, $V_{in}/V_A \approx 0.1$ and does not show any correlation with the level of turbulence. Indeed, for these fully kinetic PIC simulations, rates are consistent with a fast reconnection regime even in the laminar case - rates range between 0.04 - 0.2 [Daughton and Roytershteyn, 2012]. However, while LV99 assumes a pre-existing turbulence in the system, the simulations here discussed do not include any initial perturbation which may facilitate turbulence to develop and they can only lead to a self-generated turbulence. Nevertheless, we do not exclude that higher levels of the turbulent power in the process may affect the reconnection rate.

Lately, we would like to remark that the techniques here performed revealed powerful tools for the identification of intermittent turbulent mechanisms during the reconnection process; they potentially offer new observational tests for reconnection regions using in-situ observations, so that for example recent observations of non-Gaussian fluctuations in a turbulent jet [Huang et al., 2012] (see also Chaston et al. [2009]; Dai et al. [2011]) could be tested for ESS and non-linear ratios of exponents as found here.

Chapter 5

Conclusions

5.1 Thesis summary

In this thesis we presented a statistical approach for the identification and quantification of the statistical properties of a broad range of self-similar and quasi self-similar systems. In particular, we focused on the characterization of scaling in finite range turbulence by developing new tests for distinguishing fractal from multifractal processes.

In Chapter 1 we reviewed the turbulence phenomenon in both HD and MHD flows along with its historical development. We highlighted the strong non-linearity of turbulent systems, which is responsible of the coupling of many degrees of freedom leading to an analytically unpredictable dynamical evolution of a turbulent flow. Statistics then reveals a valid tool for studying turbulence thanks to the fact that the latter is a statistical scale invariant process, namely, its statistical properties are unchanged as we move from scale to scale subject to a rescaling.

In Chapter 2 we gave an overview on a wider class of scale invariant processes, that is, processes that show self-affinity - i.e. anisotropic self-similarity - and fractality. Importantly, we saw that these processes exhibit well defined statistical properties and scaling that uniquely characterize a scaling process. Then, we presented and discussed some statistical tools that allow to quantify the characteristic statistical scaling of both fractal processes (e.g. Wiener process, Ornstein-Uhlenbeck process, fractional Brownian motion) and multifractal processes such as intermittent turbulence. Hence, we introduced a new

statistical approach to test for multifractal scaling in finite sized turbulent systems.

Moreover, we investigated the finite size effects on scaling arising from the presence of finite cut-offs of the fields or parameters in real turbulent systems. This is seen as an extended form of self-similarity, that is, ESS, which reveals ubiquitous in finite range plasma turbulence.
We tested this generalized similarity or ESS as well as the statistical approach here proposed by analysing a solar quiescent prominence and a few numerical simulations of magnetic reconnection from the prospective of finite sized turbulent systems. Thus, we investigated the statistical properties of the physical quantities that characterize each system in order to quantify statistical scaling laws in the inertial range of turbulence.

5.1.1 Results of the analysis on the Hinode/SOT observations

In Chapter 3 we analysed images of a solar QP provided by the SOT on board the Hinode spacecraft. We presented analysis of the integrated, line of sight intensity measurements in both the time an space domain.

We found that the spatial intensity fluctuations along both the longitudinal and transverse direction to the bulk driven QP flow exhibit all the statistical properties expected for an intermittent turbulent flow in a finite sized system. Specifically, they show non-trivial power law power spectra, non-Gaussian PDFs and multifractal scaling for the GSFs. This is a clear evidence of in-situ evolving small-scale turbulence within the prominence flow; remarkably, it also confirms that line of sight intensity fluctuations, here found to be multifractal in character, are actually the response of a multifractal field associated with the physical quantities of the observed QP flow.
Moreover, we found evidence of the generalized function $G(L/L_0)$, which showed dependence on a characteristic length scale of the flow L_0 and provided indication about the crossover from the small scales to the large scales of turbulence.

On the other hand, intensity fluctuations in time revealed uncorrelated. The cause for this was attributed to the sample time of the observations, which

is too long for appreciating coherent structures (flows) moving past the line of sight. If observations with a better space-time resolution were available, we would expect the temporal intensity fluctuations to exhibit consistent statistics with a finite range turbulent flow as per the spatial fluctuations.

Remarkably, the statistical methods here used to quantify the multifractal scaling in the spatial intensity fluctuations of the QP revealed powerful tools for testing in-situ turbulence. They could be applied to others QPs in order to test whether the flow is more generally found to be turbulent; in particular it would be interesting to determine if or how the presence of turbulence in QPs correlates with their physical properties.

5.1.2 Results of the analysis on the reconnection simulations

In Chapter 4 we focused on fully kinetic PIC simulations of reconnection in a collisionless plasma. We showed the application of the statistical tools discussed in Chapter 2 to the magnetic field fluctuations of two 2D simulations, one with a symmetric initial configuration of the magnetic field and the other with an asymmetric configuration, and successively we moved to the study of a 3D simulation with a symmetric configuration.

The 2D symmetric simulation showed the formation of three large magnetic islands, which prevent turbulence to develop. We attributed this behaviour to the 2D geometry of the system for which small scale magnetic structures cannot move relative to each other in the third direction, since they are forced to lie in a plane forming large structures. However, the 2D asymmetric simulation, which does not develop any large structures, manifested a weakly intermittent turbulence at later times of the simulation, suggesting that the small coherent structures, in absence of the large ones, can actually interact non-linearly leading to turbulence despite the 2D geometry of the system.

Hence, we conclude that the 2D geometry of the system in these simulations does not represent a restriction for turbulence to generate, it may rather affect its development - i.e. level of power. On the contrary, large magnetic structures acting as boundaries, may prevent turbulence to rise since they limit

non-linear interactions between small scale coherent structures.

We recovered a completely different scenario for the 3D symmetric simulation. In this case, indeed, the third direction allows magnetic structures to develop freely without organizing in large structures. This enables small scale coherent structures to interact non-linearly with each others leading to a fully developed turbulence.
As a consequence of this, we found that the magnetic field fluctuations along the perpendicular direction to the macroscopic magnetic field exhibit the hallmarks of intermittent multifractal turbulence, that is, they are described by non-Gaussian statistics, show evidence of ESS and the GSF scaling exponent is consistent with a multifractal scaling.
The multifractal nature of the magnetic field fluctuations in both the 3D symmetric simulation and the 2D asymmetric simulation suggests that dissipation, in the sense of conversion of magnetic to kinetic energy, in collisionless reconnection on kinetic scales has an analogue in dissipation in fluid-like turbulent phenomenology, in that it proceeds via a spatial multifractal field of structures generated by an intermittent cascade. This was confirmed by the multifractal topology found for the spatial field $\mathbf{J} \cdot \mathbf{E}$ by performing a box-counting analysis.

5.2 Discussions and future work

We presented the analysis of two very different physical systems: a solar QP and few PIC simulations of magnetic reconnection. Although both the physics and the accessible physical observables of these two environments are different, however the underling turbulent process along with its characteristic statistical properties are qualitatively the same.
The above systems have the common feature to be bounded, namely, the turbulent flow is either constrained between large structures like in the QP, or evolves in a confined space, as the reconnecting magnetic field within the simulation box. The effects of the boundaries on the turbulence process manifest by conditioning the scaling properties of the turbulent fluctuations in a way that is still not fully known. The generalized scaling observed for finite sized turbulent systems is the most evident signature of these effects. We indeed

consistently recovered ESS in both the QP turbulent flow and the reconnection simulations. Importantly, we found that the generalized function anticipated by ESS appears insensitive to the details of the QP flow; it rather depends on some characteristic scale of the flow and determines the crossover to the outer scale of turbulence, which we saw corresponds to the large-scale structures of the QP that bound the turbulent flow. This suggests that the generalized function contains some information about the boundaries of the system, in other words, the "box" in which the evolving turbulence is constrained. It would be intriguing to investigate the generalized function in many other bounded turbulent flows in both HD and MHD - e.g. turbulent experiments in pipe flows, in the solar wind, atmospheric turbulence data, and so on - in order to detect the physical parameters that determine its functional form as well as its effects on scaling. Determining the form of the generalized function and its dependence on flow parameters is then crucial in order to fully quantify scaling in finite range turbulence. It would also allow to have direct access to the scaling exponent $\zeta(p)$ and therefore develop theoretical models for turbulence in finite sized systems.

Moreover, the statistical techniques here applied revealed valid tools for the characterization of the turbulent process in the systems here analysed. They indeed allowed us to fully quantify the statistical properties of the spatio-temporal fluctuations associated with the systems analysed. In particular, we demonstrated how tests for fractal/multifractal scaling can be used for the characterization of intermittency phenomena in the turbulence cascade and, importantly, how it is possible to distinguish turbulence from other processes that show statistical scaling such as white and coloured noise, which are the major source of uncertainty on data.

These statistical tools then have a broad applicability that goes beyond the characterization of the inertial range turbulence scaling only. The generalized scaling, indeed, has also been found in critical phenomena in presence of finite cut-offs of the fields or parameters [Dubrulle, 2000] suggesting that an extended scale symmetry is not unique to turbulence but is rather ubiquitous in Nature, pointing therefore to a universal feature of finite size scale invariant processes.

List of Figures

List of Tables

Bibliography

V. Abramenko, V. Yurchyshyn, and H. Wang. Intermittency in the photosphere and corona above an active region. *Astrophys. J.*, 681(2):1669, 2008. 25

M. J. Aschwanden. *Physics of the Solar Corona. An Introduction.* Praxis Publishing Ltd, Aug. 2004. 25, 34, 59

G. I. Barenblatt. Turbulent boundary layers at very large Reynolds numbers. *Russian Math. Surv.*, 59:47–64, feb 2004. 19

M. Bárta, J. Büchner, and M. Karlický. Multi-scale MHD approach to the current sheet filamentation in solar coronal reconnection. *Advances in Space Research*, 45:10–17, Jan. 2010. 33

M. Bárta, J. Büchner, M. Karlický, and P. Kotrč. Spontaneous Current-layer Fragmentation and Cascading Reconnection in Solar Flares. II. Relation to Observations. *Astrophys. J.*, 730:47, Mar. 2011. 34

R. Benzi, S. Ciliberto, R. Tripiccione, C. Baudet, F. Massaioli, and S. Succi. Extended self-similarity in turbulent flows. *Phys. Rev. E*, 48:29–+, July 1993. 20, 56

T. Berger. Hinode/SOT Observations of Quiescent Prominence Dynamics. In B. Lites, M. Cheung, T. Magara, J. Mariska, and K. Reeves, editors, *The Second Hinode Science Meeting: Beyond Discovery-Toward Understanding*, volume 415 of *Astronomical Society of the Pacific Conference Series*, page 109, Dec. 2009. 58

T. E. Berger, R. A. Shine, G. L. Slater, T. D. Tarbell, A. M. Title, T. J. Okamoto, K. Ichimoto, Y. Katsukawa, Y. Suematsu, S. Tsuneta, B. W.

Lites, and T. Shimizu. Hinode SOT Observations of Solar Quiescent Prominence Dynamics. *Astrophys. J. Lett.*, 676:L89–L92, Mar. 2008. 58, 74

T. E. Berger, G. Slater, N. Hurlburt, R. Shine, T. Tarbell, A. Title, B. W. Lites, T. J. Okamoto, K. Ichimoto, Y. Katsukawa, T. Magara, Y. Suematsu, and T. Shimizu. Quiescent Prominence Dynamics Observed with the Hinode Solar Optical Telescope. I. Turbulent Upflow Plumes. *Astrophys. J.*, 716: 1288–1307, June 2010. 28, 58

T. E. Berger, P. Testa, A. Hillier, P. Boerner, B. C. Low, K. Shibata, C. Schrijver, T. Tarbell, and A. Title. Magneto-thermal convection in solar prominences. *Nature*, 472:197–200, Apr. 2011. 28

A. Bershadskii. Beyond Scaling and Locality in Turbulence. *J. of Stat. Phys.*, 128:721–739, Aug. 2007. 19, 20, 21, 57

N. Bessho and A. Bhattacharjee. Collisionless Reconnection in an Electron-Positron Plasma. *Phys. Rev. Lett.*, 95(24):245001, Dec. 2005. 33

A. Bhattacharjee, Y.-M. Huang, H. Yang, and B. Rogers. Fast reconnection in high-lundquist-number plasmas due to the plasmoid instability. *Phys. Plasmas*, 16:112102, 2009. 33, 35

R. Bhattacharya and E. C. Waymire. *A Basic Course in Probability Theory*. Springer, 2008. 45

C. K. Birdsall and B. Langdon. *Plasma Physics via Computer Simulation*. McGraw-Hill, 1985. 79, 95

J. Birn, J. Drake, M. Shay, B. Rogers, R. Denton, M. Hesse, M. Kuznetsova, Z. Ma, A. Bhattacharjee, A. Otto, and P. Pritchett. Geospace environmental modeling (GEM) magnetic reconnection challenge. *J. Geophys. Res.*, 106: 3715, 2001. 36

D. Biskamp. *Magnetohydrodynamic Turbulence*. Cambridge University Press, 1993. 11, 32

T. Bohr, M. H. Jensen, G. Paladin, and A. Vulpiani. *Dynamical Systems Approach to Turbulence*. Cambridge University Press, 1998. 7

P. K. Browning, C. Gerrard, A. W. Hood, R. Kevis, and R. A. M. van der Linden. Heating the corona by nanoflares: simulations of energy release triggered by a kink instability. *Astron. Astrophys.*, 485:837–848, July 2008. 29

R. Bruno and V. Carbone. The Solar Wind as a Turbulence Laboratory. *Liv. Rev. in Solar Phys.*, 2:4–+, Sept. 2005. 100

V. Carbone. Cascade model for intermittency in fully developed magnetohydrodynamic turbulence. *Phys. Rev. Lett.*, 71:1546–1548, Sept. 1993. 11

V. Carbone, P. Veltri, and R. Bruno. Solar wind low-frequency magnetohydrodynamic turbulence: extended self-similarity and scaling laws. *Nonlinear Processes in Geophys.*, 3(4):247–261, 1996. 21, 56

H. Carmichael. A Process for Flares. *NASA Special Publication*, 50:451, 1964. 26

O. Chang, S. Peter Gary, and J. Wang. Whistler turbulence forward cascade: Three-dimensional particle-in-cell simulations. *Geophys. Res. Lett.*, 38: L22102, Nov. 2011. 35

S. Chapman, R. Nicol, E. Leonardis, K. Kiyani, and V. Carbone. Observation of Universality in the Generalized Similarity of Evolving Solar Wind Turbulence as Seen by Ulysses. *Astrophys. J. Lett.*, 695:L185, 2009. 21, 100

S. C. Chapman and B. Hnat. Quantifying scaling in the velocity field of the anisotropic turbulent solar wind. *Geophys. Res. Lett.*, 34(17), 2007. ISSN 1944-8007. 12

S. C. Chapman and R. M. Nicol. Generalized Similarity in Finite Range Solar Wind Magnetohydrodynamic Turbulence. *Phys. Rev. Lett.*, 103(24): 241101–+, Dec. 2009. 20, 21, 57, 100

S. C. Chapman, B. Hnat, G. Rowlands, et al. Scaling collapse and structure functions: identifying self-affinity in finite length time series. *Nonlinear Processes in Geophys.*, 12:767–774, 2005. 56

C. C. Chaston, J. R. Johnson, M. Wilber, M. Acuna, M. L. Goldstein, and H. Reme. Kinetic alfvén wave turbulence and transport through a reconnection diffusion region. *Phys. Rev. Lett.*, 102:015001, Jan 2009. 35, 109

J. Cleve, T. Dziekan, J. Schmiegel, O. E. Barndorff-Nielsen, B. R. Pearson, K. R. Sreenivasan, and M. Greiner. Finite-size scaling of two-point statistics and the turbulent energy cascade generators. *Phys. Rev. E*, 71(2):026309, Feb. 2005. 19

L. Dai et al. Cluster observations of surface waves in the ion jets from magnetotail reconnection. *J. Geophys. Res.(Space Phys.)*, 116:A12227, Dec. 2011. 109

W. Daughton and V. Roytershteyn. Emerging Parameter Space Map of Magnetic Reconnection in Collisional and Kinetic Regimes. *Space Sci. Rev.*, 172: 271–282, Nov. 2012. 109

W. Daughton, J. Scudder, and H. Karimabadi. Fully kinetic simulations of undriven magnetic reconnection with open boundary conditions. *Phys. Plasmas*, 13(7):072101, July 2006. 77, 79, 85

W. Daughton, J. Scudder, and H. Karimabadi. Fully kinetic simulations of undriven magnetic reconnection with open boundary conditions. *Phys. Plasmas*, 13:072101, 2006. 33

W. Daughton, V. Roytershteyn, B. J. Albright, H. Karimabadi, L. Yin, and K. J. Bowers. Transition from collisional to kinetic regimes in large-scale reconnection layers. *Phys. Rev. Lett.*, 103(6):065004, Aug. 2009. 33

W. Daughton, V. Roytershteyn, H. Karimabadi, L. Yin, B. J. Albright, B. Bergen, and K. J. Bowers. Role of electron physics in the development of turbulent magnetic reconnection in collisionless plasmas. *Nature Phys.*, 7:539–542, July 2011. 37, 77, 94

R. O. Dendy and S. C. Chapman. Characterization and interpretation of strongly nonlinear phenomena in fusion, space and astrophysical plasmas. *Plasma Physics and Controlled Fusion*, 48:B313–B328, Dec. 2006. 21, 57

K. P. Dere. The Rate of Magnetic Reconnection Observed in the Solar Atmosphere. *Astrophys. J.*, 472:864, Dec. 1996. 29

M. Dimitropoulou, M. Georgoulis, H. Isliker, L. Vlahos, A. Anastasiadis, D. Strintzi, and X. Moussas. The correlation of fractal structures in the photospheric and the coronal magnetic field. *A&A*, 505(3):1245–1253, 2009. 25

J. F. Drake, M. Swisdak, H. Che, and M. A. Shay. Electron acceleration from contracting magnetic islands during reconnection. *Nature*, 443:553–556, Oct. 2006. 32

J. F. Drake, M. Swisdak, K. Schoeffler, B. Rogers, and S. Kobayashi. Formation of secondary islands during magnetic reconnection. *Geophys. Res. Lett.*, 33:L13105, 2006. 33

B. Dubrulle. Finite size scale invariance. *European Physical Journal B*, 14: 757–771, Apr. 2000. 19, 21, 57, 114

T. Dudok de Wit. Can high-order moments be meaningfully estimated from experimental turbulence measurements? *Phys. Rev. E*, 70(5):055302–+, Nov. 2004. 61

B. D. Dudson, R. O. Dendy, A. Kirk, H. Meyer, and G. F. Counsell. Comparison of L- and H-mode plasma edge fluctuations in MAST. *Plasma Physics and Controlled Fusion*, 47:885–901, June 2005. 21, 57

J. W. Dungey. Interplanetary magnetic field and the auroral zones. *Phys. Rev. Lett.*, 6:47–48, Jan 1961. 29

O. Engvold. The small scale velocity field of a quiescent prominence. *Solar Phys.*, 70:315–324, Apr. 1981. 27

O. Engvold. Observations of Filament Structure and Dynamics (Review). In D. F. Webb, B. Schmieder, & D. M. Rust, editor, *IAU Colloq. 167: New Perspectives on Solar Prominences*, volume 150 of *Astronomical Society of the Pacific Conference Series*, page 23, 1998. 27

G. L. Eyink, A. Lazarian, and E. T. Vishniac. Fast magnetic reconnection and spontaneous stochasticity. *Astrophys. J.*, 743:51, 2011. 35

C. Foullon, E. Verwichte, and V. M. Nakariakov. Ultra-long-period Oscillations in EUV Filaments Near to Eruption: Two-wavelength Correlation and Seismology. *Astrophys. J.*, 700:1658–1665, Aug. 2009. 28

C. Foullon, E. Verwichte, V. M. Nakariakov, K. Nykyri, and C. J. Farrugia. Magnetic Kelvin-Helmholtz Instability at the Sun. *Astrophys. J. Lett.*, 729: L8, Mar. 2011. 28

U. Frisch. *Turbulence: The Legacy of A.N. Kolmogorov*. Cambridge University Press, 1995. 6, 7, 9, 13, 14, 16, 50, 55, 70, 91

U. Frisch, P.-L. Sulem, and M. Nelkin. A simple dynamical model of intermittent fully developed turbulence. *J. Fluid Mech.*, 87:719–736, Aug. 1978. 4, 15

H. P. Furth, J. Killeen, and M. N. Rosenbluth. FiniteâResistivity Instabilities of a Sheet Pinch. *Phys. Fluid*, 6:459, 1963. 33

S. Galtier, S. V. Nazarenko, A. C. Newell, and A. Pouquet. A weak turbulence theory for incompressible magnetohydrodynamics. *J. Plasma Phys.*, 63: 447–488, June 2000. 12

C. W. Gardiner. *Handbook of Stochastic Methods*. Springer, third edition, 2004. 43, 44, 46, 47

R. G. Giovanelli. A Theory of Chromospheric Flares. *Nature*, 158:81–82, July 1946. 31

P. Goldreich and S. Sridhar. Toward a theory of interstellar turbulence. 2: Strong alfvenic turbulence. *Astrophys. J.*, 438:763–775, Jan. 1995. 12

L. Golub and J. M. Pasachoff. *The Solar Corona*. Cambridge University Press, second edition, 2010. 22

S. Grossmann, D. Lohse, V. L'vov, and I. Procaccia. Finite size corrections to scaling in high reynolds number turbulence. *Phys. Rev. Lett.*, 73:432–435, July 1994. 19, 20, 21, 57

J. Hershaw, C. Foullon, V. M. Nakariakov, and E. Verwichte. Damped large amplitude transverse oscillations in an EUV solar prominence, triggered by large-scale transient coronal waves. *Astron. Astrophys.*, 531:A53, July 2011. 28

M. Hesse, K. Schindler, J. Birn, and M. Kuznetsova. The diffusion region in collisionless magnetic reconnection. *Phys. Plasmas*, 6:1781–1795, 1999. 37

J. C. Higdon. Density fluctuations in the interstellar medium: Evidence for anisotropic magnetogasdynamic turbulence. I - Model and astrophysical sites. *Astrophys. J.*, 285:109–123, Oct. 1984. 12

B. Hnat, S. C. Chapman, K. Kiyani, G. Rowlands, and N. W. Watkins. On the fractal nature of the magnetic field energy density in the solar wind. *Geophys. Res. Lett.*, 34:L15108, 2007. 56

T. S. Horbury and A. Balogh. Structure function measurements of the intermittent MHD turbulent cascade/a. *Nonlinear Processes in Geophys.*, 4: 185–199, 1997. 56

S. Y. Huang et al. Observations of turbulence within reconnection jet in the presence of guide field. *Geophys. Res. Lett.*, 39:11104, June 2012. 35, 99, 109

Y.-M. Huang and A. Bhattacharjee. Scaling laws of resistive magnetohydrodynamic reconnection in the high-lundquist-number, plasmoid-unstable regime. *Phys. Plasmas*, 17:062104, 2010. 33, 35

P. S. Iroshnikov. Turbulence of a Conducting Fluid in a Strong Magnetic Field. *Sov. Astron.*, 7:566, Feb. 1964. 11

H. Kantz and T. Schreiber. *Nonlinear time series analysis*. Cambridge University Press, 1997. 41, 44, 48, 51

H. Karimabadi, D. Krauss-Varban, J. D. Huba, and H. X. Vu. On magnetic reconnection regimes and associated three-dimensional asymmetries: Hybrid, Hall-less hybrid, and Hall-MHD simulations. *J. Geophys. Res.(Space Phys.)*, 109:A09205, Sept. 2004. 32

H. Karimabadi, W. Daughton, and J. Scudder. Multi-scale structure of the electron the electron diffusion region. *Geophys. Res. Lett.*, 34:L13104, 2007. 33

H. Karimabadi, J. Dorelli, V. Roytershteyn, W. Daughton, and L. Chacón. Flux Pileup in Collisionless Magnetic Reconnection: Bursty Interaction of Large Flux Ropes. *Phys. Rev. Lett.*, 107(2):025002, July 2011. 35

M. Karlický and M. Bárta. Successive Merging of Plasmoids and Fragmentation in a Flare Current Sheet and Their X-Ray and Radio Signatures. *Astrophys. J.*, 733:107, June 2011. 34

M. Karlický, M. Bárta, and D. Nickeler. Fragmentation during merging of plasmoids in the magnetic field reconnection. *Astron. Astrophys.*, 541:A86, May 2012. 34

J. T. Karpen, S. K. Antiochos, M. Hohensee, J. A. Klimchuk, and P. J. MacNeice. Are Magnetic Dips Necessary for Prominence Formation? *Astrophys. J. Lett.*, 553:L85–L88, May 2001. 76

B. Kaulakys and T. Meš Kauskas. Modeling 1/f noise. *Phys. Rev. E*, 58: 7013–7019, Dec. 1998. 63

B. Kaulakys, V. Gontis, and M. Alaburda. Point process model of 1/f noise vs a sum of Lorentzians. *Phys. Rev. E*, 71(5):051105–+, May 2005. 63

G. Kitagawa. *Introduction to time series modelling*. Taylor & Francis Group, LLC, 2010. 51

M. G. Kivelson and C. T. Russel. *Introduction to Space Physics*. Cambridge University Press, 1995. 21, 22

K. Kiyani, S. Chapman, and B. Hnat. Extracting the scaling exponents of a self-affine, non-Gaussian process from a finite-length time series. *Phys. Rev. E*, 74(5):51122, 2006. 53, 56

K. Kiyani, S. C. Chapman, B. Hnat, and R. M. Nicol. Self-Similar Signature of the Active Solar Corona within the Inertial Range of Solar-Wind Turbulence. *Phys. Rev. Lett.*, 98(21):211101–+, May 2007. 21, 56

K. Kiyani, S. C. Chapman, and N. W. Watkins. Global Scale-Invariant Dissipation in Collisionless Plasma Turbulence. *Phys. Rev. E*, 79:036109, 2009. 56, 84, 93

K. H. Kiyani et al. Enhanced magnetic compressibility and isotropic scale invariance at sub-ion larmor scales in solar wind turbulence. *Astrophys. J.*, 763(1):10, 2013. 99

B. Kliem, M. Karlický, and A. O. Benz. Solar flare radio pulsations as a signature of dynamic magnetic reconnection. *Astron. Astrophys.*, 360:715–728, Aug. 2000. 33

A. Klimas, M. Hesse, and S. Zenitani. Particle-in-cell simulations of collisionless reconnection with open outflow boundaries. *Phys. Plasmas*, 15:082102, 2008. 33

A. Klimas, V. Uritsky, and E. Donovan. Multiscale auroral emission statistics as evidence of turbulent reconnection in Earth's midtail plasma sheet. *J. Geophys. Res.(Space Phys.)*, 115:A06202, June 2010. 35

A. N. Kolmogorov. Dissipation of Energy in Locally Isotropic Turbulence. *Dokl. Akad. Nauk SSSR*, 32:16–18, 1941. 8

A. N. Kolmogorov. A refinement of previous hypotheses concerning the local structure of turbulence in a viscous incompressible fluid at high Reynolds number. *J. Fluid Mech.*, 13:82–85, 1962. 14

G. Kowal, A. Lazarian, E. T. Vishniac, and K. Otmianowska-Mazur. Numerical Tests of Fast Reconnection in Weakly Stochastic Magnetic Fields. *Astrophys. J.*, 700:63–85, July 2009. 36, 109

G. Kowal, E. M. de Gouveia Dal Pino, and A. Lazarian. Particle Acceleration in Turbulence and Weakly Stochastic Reconnection. *Phys. Rev. Lett.*, 108 (24):241102, June 2012. 36

R. H. Kraichnan. Inertial-Range Spectrum of Hydromagnetic Turbulence. *Phys. of Fluids*, 8:1385–1387, July 1965. 11

L. D. Landau and E. M. Lifshitz. *Fluid mechanics*. Pergamon Press, second edition, 1987. 9

P. Langevin. On the Theory of Brownian Motion. *C. R. Acad. Sci. (Paris)*, 146:530–533, 1908. 47

G. Lapenta. Self-feeding turbulent reconnection on macroscopic scales. *Phys. Rev. Lett.*, 100:235001, 2008. 33, 35

G. Lapenta and A. Lazarian. Achieving fast reconnection in resistive MHD models via turbulent means. *Nonlinear Processes in Geophys.*, 19:251–263, Apr. 2012. 36

A. Lazarian and E. T. Vishniac. Reconnection in a Weakly Stochastic Field. *Astrophys. J.*, 517:700–718, June 1999. 36, 109

A. Lazarian, G. L. Eyink, and E. T. Vishniac. Relation of astrophysical turbulence and magnetic reconnection. *Phys. Plasmas*, 19(1):012105, Jan. 2012. 36

M. Lesieur. *Turbulence in Fluids*. Springer, fourth edition, 2008. 14

Y. Lin, O. Engvold, L. Rouppe van der Voort, J. E. Wiik, and T. E. Berger. Thin Threads of Solar Filaments. *Solar Phys.*, 226:239–254, Feb. 2005. 27

N. Loureiro, D. A.Uzdensky, A. Schekochihin, S. Cowley, and T. Yousef. Turbulent magnetic reconnection in two dimensions. *Mon. Not. Roy. Astron. Soc.*, 399(1):L146–L150, 2009. 35

N. F. Loureiro, A. A. Schekochihin, and S. C. Cowley. Instability of current sheets and formation of plasmoid chains. *Phys. Plasmas*, 14(10):100703, 2007. 33, 35

B. C. Low and J. R. Hundhausen. Magnetostatic structures of the solar corona. 2: The magnetic topology of quiescent prominences. *Astrophys. J.*, 443: 818–836, Apr. 1995. 28

D. H. Mackay, J. T. Karpen, J. L. Ballester, B. Schmieder, and G. Aulanier. Physics of Solar Prominences: IIMagnetic Structure and Dynamics. *Space Sci. Rev.*, 151:333–399, Apr. 2010. 27

B. Mandelbrot. *Fractals: Form, Chance, and Dimension.* Mathematics Series. W. H. Freeman, 1977. 15, 39, 93

B. Mandelbrot. *The Fractal Geometry of Nature.* W. H. Freeman, San Francisco, 1982. 39

B. B. Mandelbrot. Self-afi¬$nefractalsandthefractaldimension.Physica\ Scripta$, 32 : 257 − −260, 1985. 39

B. B. Mandelbrot and J. W. van Ness. *Fractional Brownian motions, fractional noises and applications*, volume 10. 1968. 47

B. B. Mandelbrot and J. A. Wheeler. The Fractal Geometry of Nature. *American Journal of Physics*, 51:286–287, Mar. 1983. 39

M.-J. Martres, P. Mein, B. Schmieder, and I. Soru-Escaut. Structure and evolution of velocities in quiescent filaments. *Solar Phys.*, 69:301–312, Feb. 1981. 27

M. Materassi and G. Consolini. Magnetic Reconnection Rate in Space Plasmas: A Fractal Approach. *Phys. Rev. Lett.*, 99(17):175002, Oct. 2007. 35

W. Matthaeus and S. Lamkin. Rapid reconnection caused by finite amplitude fluctuations. *Phys. Fluid*, 28:303, 1985. 35

W. Matthaeus and S. Lamkin. Turbulent reconnection. *Phys. Fluid*, 29:2513, 1986. 35

W. H. Matthaeus and M. L. Goldstein. Low-frequency $1/f$ noise in the interplanetary magnetic field. *Phys. Rev. Lett.*, 57(4):495–498, Jul 1986. 25

W. H. Matthaeus and M. Velli. Who Needs Turbulence?. A Review of Turbulence Effects in the Heliosphere and on the Fundamental Process of Reconnection. *Space Sci. Rev.*, 160:145–168, Oct. 2011. 35

W. McComb. *The Physics of Fluid Turbulence.* Oxford University Press, 1990. 6, 18, 19

C. Meneveau and K. R. Sreenivasan. Simple multifractal cascade model for fully developed turbulence. *Phys. Rev. Lett.*, 59:1424–1427, Sept. 1987. 17

M. D. Millionshchikov. The theory of homogeneous isotropic turbulence. *Dokl. Akad. Nauk SSSR*, 32:611, 1941. 19

A. S. Monin and A. M. Yaglom. *Statistical Fluids Mechanics: Mechanics of Turbulence*. The MIT Press, 1971. 14, 19

R. Nicol, S. Chapman, and R. Dendy. The Signature of Evolving Turbulence in Quiet Solar Wind as Seen by Ulysses. *Astrophys. J.*, 679(1):862–870, 2008. 21, 56

A. M. Obukhov. Spectral energy distribution of a turbulent flow. *Izv. Akad. Nauk SSSR, Ser. Geogr. Geophys.*, 5:453–466, 1941. 8

A. M. Obukhov. Some specific features of atmospheric turbulence. *J. Fluid Mech.*, 12:78–81, 1962. 14

G. Paladin and A. Vulpiani. Anomalous scaling laws in multifractal objects. *Phys. Reports*, 156:147–225, Dec. 1987. 17

G. Parisi and U. Frisch. *Turbulence and Predictability of Geophysical Flows and Climatic Dynamics*. North Holland Amsterdam, 1985. 16

E. N. Parker. Sweet's Mechanism for Merging Magnetic Fields in Conducting Fluids. *J. Geophys. Res.*, 62:509–520, Dec. 1957. 31

D. B. Percival and A. T. Walden. *Spectral Analysis for Physical Applications*. Cambridge University Press, 2000. 50, 51

H. E. Petschek. Magnetic Field Annihilation. *NASA Special Publication*, 50: 425, 1964. 32

R. F. Pinto, A. S. Brun, L. Jouve, and R. Grappin. Coupling the Solar Dynamo and the Corona: Wind Properties, Mass, and Momentum Losses during an Activity Cycle. *Astrophys. J.*, 737:72, Aug. 2011. 25

E. Priest and T. Forbes. *Magnetic Reconnection*. Cambridge University Press, June 2000. 29

P. Pritchett. Geospace environmental modeling magnetic reconnection challenge: Simulations with a full particle electromagnetic code. *J. Geophys. Res.*, 106:3783–3798, 2001. 37

L. F. Richardson. *Weather Prediction by Numerical Process*. Cambridge University Press, 1922. 4

H. J. O. E. Russel, D. Dimension of strange attractors. *Phys. Rev. Lett.*, 45, 1980. 40

A. A. Ruzmaikin, J. Feynman, B. E. Goldstein, E. J. Smith, and A. Balogh. Intermittent turbulence in solar wind from the south polar hole. *J. Geophys. Res.*, 100:3395, 1995. 16

S. Servidio, P. Dmitruk, A. Greco, M. Wan, S. Donato, P. A. Cassak, M. A. Shay, V. Carbone, and W. H. Matthaeus. Magnetic reconnection as an element of turbulence. *Nonlinear Processes in Geophys.*, 18:675–695, Oct. 2011. 35

L. Seuront, F. Schmitt, Y. Lagadeuc, D. Schertzer, and S. Lovejoy. Universal multifractal analysis as a tool to characterize multiscale intermittent patterns example of phytoplankton distribution in turbulent coastal waters. *J. Plankton Res.*, 21(5):877–922, 1999. 14, 15, 17

M. Shay, J. Drake, and M. Swisdak. Two-scale structure of the electron dissipation region during collisionless magnetic reconnection. *Phys. Rev. Lett.*, 99:155002, 2007. 33

Z.-S. She and E. Leveque. Universal scaling laws in fully developed turbulence. *Phys. Rev. Lett.*, 72:336–339, Jan. 1994. 17

K. Shibata. *Proc-1995-Watanabe*, 85, 1995. 26

K. Shibata and S. Tanuma. Plasmoid-induced-reconnection and fractal reconnection. *Earth, Planets, and Space*, 53:473–482, June 2001. 33

D. Sornette. *Critical phenomena in natural sciences : chaos, fractals, selforganization and disorder : concepts and tools*. Springer, 2000. 19, 39, 45, 46, 55, 57

K. R. Sreenivasan and A. Bershadskii. Finite-Reynolds-number effects in turbulence using logarithmic expansions. *J. Fluid Mech.*, 554:477–498, May 2006. 19

P. A. Sturrock. Model of the High-Energy Phase of Solar Flares. *Nature*, 211: 695–697, Aug. 1966. 26

P. A. Sweet. The Neutral Point Theory of Solar Flares. In B. Lehnert, editor, *IAU Symp. 6, Electromagnetic Phenomena in Cosmical Physics*, page 123. New York: Cambridge Univ. Press, 1958. 31

D. Telloni, R. Bruno, V. Carbone, E. Antonucci, and R. D'Amicis. Statistics of density fluctuations during the transition from the outer solar corona to the interplanetary space. *Astrophys. J.*, 706(1):238, 2009. 25

S. Tsuneta. Structure and Dynamics of Magnetic Reconnection in a Solar Flare. *Astrophys. J.*, 456:840, Jan. 1996. 26

A. J. Turner, G. Gogoberidze, and S. C. Chapman. Nonaxisymmetric Anisotropy of Solar Wind Turbulence as a Direct Test for Models of Magnetohydrodynamic Turbulence. *Phys. Rev. Lett.*, 108(8):085001, Feb. 2012. 99

D. A. Uzdensky, N. F. Loureiro, and A. A. Schekochihin. Fast Magnetic Reconnection in the Plasmoid-Dominated Regime. *Phys. Rev. Lett.*, 105 (23):235002, Dec. 2010. 33

M. Van Dyke. *An album of fluid motion.* Stanford, CA: Parabolic Press, 1982. 6

L. J. Vasquez, A. Rodriguez, and R. A. Römer. Multifractal analysis of the metal-insulator transition in the three-dimensional Anderson model. I. Symmetry relation under typical averaging. *Phys. Rev. B*, 78(19):195106, Nov. 2008. 40

P. Veltri. MHD turbulence in the solar wind: self-similarity, intermittency and coherent structures. *Plasma Phys. and Controlled Fusion*, 41:787, Mar. 1999. 56

M. Yamada, R. Kulsrud, and H. Ji. Magnetic reconnection. *Rev. Mod. Phys.*, 82:603–664, Mar 2010. 30

J. B. Zirker, O. Engvold, and S. F. Martin. Counter-streaming gas flows in solar prominences as evidence for vertical magnetic fields. *Nature*, 396: 440–441, Dec. 1998. 27